

Dynamic Behaviour of Concrete Structures subjected to Blast and Fragment Impacts

JOOSEF LEPPÄNEN

Department of Structural Engineering
Concrete Structures
CHALMERS UNIVERSITY OF TECHNOLOGY
Göteborg, Sweden 2002

THESIS FOR THE DEGREE OF LICENTIATE OF ENGINEERING

Dynamic Behaviour of Concrete Structures subjected to Blast and Fragment Impacts

JOOSEF LEPPÄNEN

Department of Structural Engineering
Concrete Structures
CHALMERS UNIVERSITY OF TECHNOLOGY
Göteborg, Sweden 2002

Dynamic Behaviour of Concrete Structures subjected to Blast and Fragment Impacts
JOOSEF LEPPÄNEN

© JOOSEF LEPPÄNEN, 2002

ISSN 1650-514X

Publication no. 02:4

Archive no. 31

Department of Structural Engineering

Concrete Structures

Chalmers University of Technology

SE-412 96 Göteborg

Sweden

Telephone: + 46 (0)31-772 1000

Cover:

Steel projectile impacting a concrete target; see Figure 6.6.

Chalmers Reproservice
Göteborg, Sweden 2002

Dynamic Behaviour of Concrete Structures subjected to Blast and Fragment Impacts

JOOSEF LEPPÄNEN

Department of Structural Engineering

Concrete Structures

Chalmers University of Technology

ABSTRACT

For protective structures, reinforced concrete is commonly used. Concrete structures subjected to explosive loading in a combination of blast and fragments will have very different response than statically loaded structure. During the blast and the fragment impacts the structure will shake and vibrate, severe crushing of concrete occurs and a crater forms (spalling) in the front of the concrete; for large penetration, scabbing may occur at the backside of the wall, or even perforation, with a risk of injury for people inside the structure.

This thesis is intended to increase the knowledge of reinforced concrete structures subjected to explosive loading, i.e. effects of blast and fragmentation. A further aim is to describe and use the non-linear finite element (FE) method for concrete penetration analyses. Particular attention is given to dynamic loading, where the concrete behaviour differs compared to static loading. The compressive and tensile strengths increase due to the strain rate effects. Initial stiffness increases, and moreover the concrete strain capacity is increased in dynamic loading.

Traditionally, for prediction of the depth of penetration and crater formation from fragments and projectiles, empirical relationships are used, which are discussed here together with the effects of the blast wave that is caused by the explosion.

To learn more about the structural behaviour of concrete subjected to severe loading, a powerful tool is to combine advanced non-linear FE analyses and experiments. A trustworthy model must be able to capture correct results from several experiments, including both the depth of penetration and the crater size. In this thesis, FE analyses of concrete penetration with steel projectiles have been performed and compared to existing experimental results. By using the non-linear FE program AUTODYN, the depth of penetration and crater sizing can be predicted.

Key words: concrete, blast, fragment, projectile, impact, penetration, perforation, dynamic loading, strain rate, non-linear finite element analyses, protective structures.

Splitterbelastade Betongkonstruktioners Dynamiska Verkningsätt

JOOSEF LEPPÄNEN

Institutionen för konstruktionsteknik

Betongbyggnad

Chalmers tekniska högskola

SAMMANFATTNING

Armerade betongkonstruktioner utsatta för explosionslaster i kombination med stötvågs- och splitterbelastning skiljer sig avsevärt från statisk belastning. Under belastningen av stötvågen och splittrets inträngning kommer konstruktionen att skaka och vibrera, och omfattande krossning och sprickutveckling sker. På belastningssidan av konstruktionen uppstår en krater genom splittrets kontaktverkan. Dessutom kan splittret penetrera betongen. Om inträngningsdjupet är tillräckligt stort kan utstötning ske på baksidan, eller till och med perforation, med risk att skada människor bakom konstruktionen.

Målet med denna studie är att öka kunskapen om armerade betongkonstruktioner utsatta för explosionslaster i kombination med stötvågs- och splitterbelastning. Vidare beskrivs och nyttjas icke-linjär finit elementmetod för penetrationsanalyser i betong. Särskilt intresse har ägnats åt betongens egenskaper vid dynamisk belastning där beteendet skiljer sig från den statiska belastningen. Betongens tryck- och draghållfasthet ökar på grund av töjningshastighetseffekten. Även styvheten och betongens deformationskapacitet ökar vid dynamisk belastning.

Traditionellt har empiriska samband nyttjats för att bedöma inträngningsdjup och kraterstorlek från splitter och projektiler som träffar en betongkonstruktion. Dessa, tillsammans med effekter av stötvågen från en explosion, har studerats.

För att öka kunskapen om det strukturella beteendet hos betongkonstruktioner utsatta för extrema belastningar är en kombination med experiment och finita elementanalyser en bra metod. En trovärdig modell skall kunna förutsäga experimentella resultat från flera experiment med olika utformning både gällande inträngningsdjup och kraterstorlek. I den här studien har FE-analyser med stålprojektiler som penetrerar betongen utförts och jämförts med existerande försök. Med det icke-linjära finita elementprogrammet AUTODYN blir överensstämmelsen med jämförda experiment god både gällande inträngningsdjup och kraterstorlek.

Nyckelord: Betong, stötvåg, splitter, projektil, penetration, perforation, dynamik, töjningshastighet, icke-linjära finita elementanalyser, skyddsrum.

Contents

1	INTRODUCTION	1
1.1	Background and aim	1
1.2	Research area	2
1.3	Outline of contents	2
2	BLAST, STRESS AND SHOCK WAVE THEORY	3
2.1	Introduction	3
2.2	Blast waves and reflections	3
2.2.1	Blast waves	3
2.2.2	Blast wave reflections	6
2.3	Stress waves, reflections and transmission	8
2.3.1	Stress waves	8
2.3.2	Reflection and transmission of one-dimensional waves	10
2.4	Shock waves	12
3	CONCRETE UNDER SEVERE LOADING	14
3.1	Introduction	14
3.2	Weapon systems	14
3.3	Fragmentation	14
3.4	Penetration with steel fragments into different materials	16
3.5	Spalling and scabbing	19
3.6	Concrete penetration with steel projectiles	20
3.7	Concrete slabs loaded with steel fragments	21
3.8	Combined blast wave and fragment loading	23
4	BEHAVIOUR OF CONCRETE UNDER DYNAMIC LOADING	27
4.1	General	27
4.2	Behaviour of concrete under static loading	28
4.3	Strain rate effects for concrete under uniaxial loading	29
4.4	Strain rate effects of confined concrete	32
4.4.1	Strain rate effects of confined concrete in compression	32
4.4.2	Strain rate effects of confined concrete in tension	33
5	FE MODELLING OF CONCRETE UNDER SEVERE DYNAMIC LOADING	34
5.1	Introduction	34
5.2	Lagrangian, Eulerian and SPH techniques	34

5.3	Abaqus/Explicit	35
5.4	AUTODYN	37
5.4.1	Equation of state	37
5.4.2	Constitutive models	38
5.5	Treatment of blast, shock and stress waves	40
5.6	Erosion models	41
5.7	Parameter study	42
5.7.1	Mesh dependency	43
5.7.2	Residual strength	48
5.7.3	Erosion criteria	50
5.7.4	Strain rate effect of tensile strength	52
5.8	Discussion	53
6	FE ANALYSES OF CONCRETE PENETRATION	54
6.1	Experimental series	54
6.1.1	Heavy steel projectile	54
6.1.2	Light steel projectile	55
6.2	Analyses with Abaqus/Explicit	56
6.3	Analyses with AUTODYN	56
6.3.1	Mesh descriptions	58
6.3.2	Results	59
6.4	Discussion	64
6.5	Concluding remarks	65
7	CONCLUSIONS	66
7.1	General conclusions	66
7.2	Future research	67
8	REFERENCES	68
APPENDIX A	Input data to the RHT-model in AUTODYN	A1
APPENDIX B	Parameter study	B1
APPENDIX C	Empirical formulas for penetration with projectiles	C1
APPENDIX D	Empirical formulas for penetration with fragments	D1

Preface

This licentiate thesis is a part of the PhD project “Dynamic behaviour of concrete structures subjected to blast and fragments”, and was carried out from February 2000 to April 2002 at the Department of Structural Engineering, Concrete Structures, Chalmers University of Technology. The project is financially supported by the Swedish Rescue Services Agency.

I wish to thank my supervisor and examiner Professor Kent Gylltoft for his guidance and support throughout the project. Great thanks also to the members of the reference group in this project, for creative discussions and continuous progress of the project work. The group members are M.Sc. Björn Ekengren from the Swedish Rescue Services Agency, Professor Kent Gylltoft and Dr Mario Plos from Chalmers, and Dr. Morgan Johansson from Reinertsen AB.

Finally I would like to thank my colleagues at Concrete Structures for fruitful discussions.

Göteborg, April 2002

Joosef Leppänen

Notations

Roman upper case letters

A	Area, parameter for compressive yield surface
B	Parameter for residual yield surface
C	Constant to predict the depth of penetration
D	Damage
E	Young's Modulus
E_0, E_1	Energy per unit mass and time; initial and time unit one
G_F	Fracture energy
I	Acoustic impedance
I_1, I_2	Acoustic impedance; for medium one and medium two
K	Bulk Modulus
M	Parameter for residual yield surface
N	Parameter for compressive yield surface
M_c	Weight of the case
M_x, M_r	Mach number for incident shock and reflected shock
P_0, P_1	Pressure; initial and time unit one
P_r	Reflected pressure
P_s^+, P_s^-	Peak pressures
Q	Charge weight
R	Distance from explosion
T^+, T^-	Positive time duration, negative time duration
T_x, T_y, T_r	Temperature at location x, y, and reflected temperature
U	Particle velocity, shock velocity
U_0, U_1	Particle velocity; initial and time unit one
V_s	Striking velocity
W	Equivalent weight of TNT
Y	Yield strength
Y_{comp}^*	Normalized compressive failure surface
Y_{res}^*	Residual yield surface
Z	Scaling parameter

Roman lower case letters

b	Constant for describe pressure–time history
c	Stress wave velocity
c_0, c_L, c_T	Initial, longitudinal and transversal stress wave velocity
c_1, c_2	Stress wave velocity in medium one and medium two
d	Projectile diameter
e	Specific internal energy
f_t	Ultimate tensile strength
k	Slope of Rayleigh line
l	length
i^+	Positive impulse
i^-	Negative impulse
m	Mass, mass per time unit and area
m_f	Fragment mass
m_p	Projectile mass
p	Pressure
p_{crush}	Initial compaction pressure
p_0	Atmospheric pressure
r_σ, r_u	Reflected stress and velocity
t	Time
t_0, t_l	Initial time, time unit one
t_σ, t_u	Transmitted stress and velocity
u	Displacement
$\dot{u}_i, \dot{u}_r, \dot{u}_t$	Initial, reflected and transmitted velocity
v	Specific volume
v_0, v_l	Specific volume; initial and time unit one
v_i	Initial fragment velocity
v_r	Fragment velocity after a distance r
v_p	Fragment velocity for perforation in a steel plate
w	Crack opening
w_u	Ultimate crack opening
x	Depth of penetration

Greek letters

A	Reflection coefficient for normal blast wave reflection
β, δ	Reflection angles
δ	Strain rate factor
ε	Strain
ε_c	Concrete strain
ε_u	Ultimate concrete strain in tension
ε_{xx}	Strain in x-direction
$\dot{\varepsilon}$	Strain rate
$\dot{\varepsilon}_0$	Strain rate for static loading
θ	Coefficient to estimate fragment velocity
μ	Compression
ν	Poisson's ratio
ρ	Density
ρ_0, ρ_1	Density; initial and time unit one
ρ_0, ρ_s	Initial density, solid density
ρ_1, ρ_2	Density; medium one and medium two
σ	Stress
$\sigma_1, \sigma_2, \sigma_3$	Principal stresses
σ_c	Concrete stress
$\sigma_i, \sigma_r, \sigma_t$	Initial, reflected and transmitted stress
σ_{lat}	Lateral stress
σ_{xx}	Stress in x-direction

1 Introduction

1.1 Background and aim

Concrete structures are usually large and massive. For protective structures, e.g. civil defence shelters, concrete is commonly used. For civil defence shelters the main threat arises from explosions caused by military weapons, such as conventional and nuclear weapons; the latter are not considered in this thesis.

Chalmers University of Technology has long collaborated with the Swedish Rescue Services Agency. In earlier projects a combination of experiments and non-linear finite element (FE) analyses of a new reinforcement detailing in frame corners of civil defence shelters has been carried out at Chalmers; see Plos (1994), Johansson (1996), Johansson and Karlsson (1997), and Johansson (2000). These works have resulted in a new reinforcement detailing that has been introduced in the Swedish Shelter Regulations, Swedish Rescue Services Agency (1998).

The experiments and appertaining FE analyses mentioned above have been performed for static loading. However, a civil defence shelter must resist transient loading caused by explosions and falling debris from a collapsing building. Non-linear FE analyses have been performed by Johansson (1999) and Johansson (2000), where the blast wave from the detonation was taken into account, and a study of falling debris from a collapsing building was carried out. In this work it was shown how the shelter subjected to blast wave was responding at the most critical stage for the first few milliseconds. If the load was applied fast enough, some parts of the structure were not aware of the loading where other parts of it had already gone to failure. Furthermore, it was shown that the civil defence shelter could withstand the design load for the blast, according to the Swedish Shelter Regulations, Swedish Rescue Services Agency (1998).

In addition, from a detonation of a General Purpose (GP) bomb, besides the shock wave, fragments will fly against the civil defence shelter. The influence of the fragments that impact the shelter has not been taken into account by the earlier projects at Chalmers, Concrete Structures.

The work presented in this thesis is a part of a research project where the long-term aim is to increase the knowledge of reinforced concrete structures subjected to explosive loading, i.e. combination of blast wave and fragmentation. To reach the aim, a powerful tool is to combine experiments with advanced non-linear FE analyses. The work presented in this thesis is intended to give a strong basis of knowledge in the field of structures subjected to explosive loading. This includes the weapon effects, i.e. blast and fragmentation, knowledge of the material behaviour for concrete subjected to severe dynamic loading, and the damage mechanisms. Analysing a civil defence shelter subjected to explosive loading is very complex, since both the shock wave and fragmentation from a detonation must be included in the analyses. In this work the analyses are limited to a steel projectile impacting a concrete target.

1.2 Research area

The research area in this thesis is to study reinforced concrete structures subjected to an explosive loading from conventional weapons. From a high-explosive bomb, the explosive weight causes a blast wave and fragments fly in all directions from the bomb case. The physics of the detonation process is of interest, from initiation to the formation of the shock front, blast wave and fragmentation. Depending on the distance between the charge and target, the fragments can impact the target before, at the same time or after the blast wave.

A concrete structure subjected to impulse loading will have a very different response than a statically loaded structure. When fragments fly into a concrete target, spalling occurs in the front of the concrete surface as a result of the direct impact. When a shock wave propagates through the concrete and reaches the backside of the construction, it will reflect as a tensile wave, since concrete is very weak in tension, and this will lead to scabbing at the backside.

Design against fragments and projectiles is critical and an important issue for protective structures. To predict the depth of penetration in concrete targets, empirical equations have been developed from large series of experiments. The depth of penetration is a function of the impact velocity, mass, and form of the fragment or projectile, and of the target material. For concrete, the latter parameter is normally related to the compressive strength.

Furthermore, using non-linear FE analyses of concrete penetration is an issue, where the depth of penetration and crater size is of interest. In this thesis, the FE programs Abaqus/Explicit and AUTODYN have been used.

1.3 Outline of contents

In Chapter 2 the creation of a blast wave, the physics of shock waves and wave propagation are discussed.

Chapter 3 describes general weapon effects. A detonation produces a shock wave and fragmentation of the case. Further, empirical formulas for penetration and for fragment and projectile velocities are discussed. Experimental series are discussed together with damage mechanisms in concrete subjected to severe loading from explosion.

In Chapter 4 the behaviour of concrete under dynamic loading is discussed. Important parameters are the strain rate and confinement effects in concrete for uniaxial and multiaxial stress states.

Chapter 5 describes in general how to model dynamic loading in FE codes, such as blast and impact loading. In Chapter 6, comparisons with existing experiments and non-linear FE analyses with Abaqus/Explicit and AUTODYN are carried out.

In Chapter 7, conclusions are drawn from the thesis.

2 Blast, stress and shock wave theory

2.1 Introduction

To understand the behaviour of concrete structures subjected to severe loading from military weapons, the nature and physics of explosions and the creation of a blast wave and reflections from a bomb must be understood. When the blast wave hits a concrete surface, a shock wave propagates through the concrete. There are two main theories to describe the response, the Eulerian and Lagrangian methods, which are further described in section 5.2. When treating the shock wave with the Eulerian method, where a fixed reference in space is chosen and the motions are derived with respect to that region, the shock wave theory is based on the conservation of mass, momentum and energy. When treating the shock wave by the Lagrangian method, with moving reference, the stress wave theory is based on the classic wave equation of motion, where equilibrium and compatibility are considered.

An explosion is characterized by a physical or a chemical change in the material, which happens under sudden change of stored potential energy into mechanical work, with creation of a blast wave and a powerful sound; see FortH1 (1987). The explosive material can react in two ways, as a deflagration or a detonation. For deflagration, the chemical change in the reaction zone occurs below the sonic speed through the explosive material. In the case of a detonation, the chemical change in the reaction zone occurs over the sonic speed through the explosive material. In military situations, detonations are most common; for example, if a TNT charge explodes, this means that it decays as a detonation. In present thesis, by explosion is meant a detonation unless stated otherwise.

2.2 Blast waves and reflections

2.2.1 Blast waves

A shock wave resulting from an explosive detonation in free air is termed an air-blast shock wave, or simply a blast wave. The blast environment will differ depending on where the explosion takes place. In the case of an airburst, when the blast wave hits the ground surface, it will be reflected. The reflected wave will coalesce the incident wave and a mach front is created, as shown in Figure 2.1. The point where the three shock fronts meet – incident wave, reflected wave and the mach front – is termed the triple point, which is further discussed in Section 2.2.2.3.

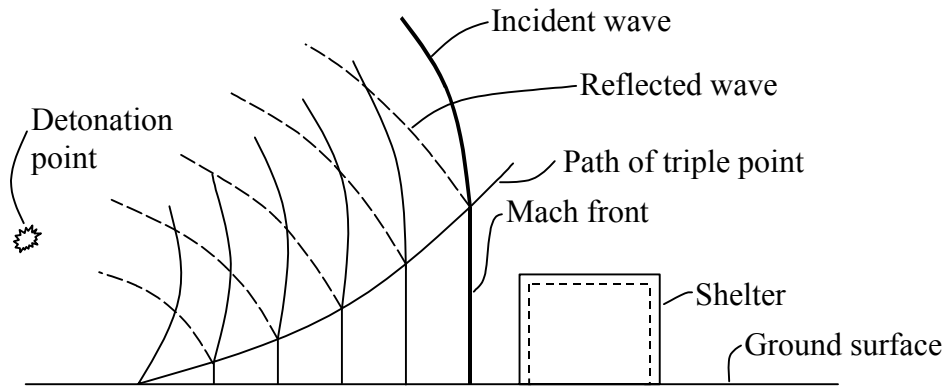


Figure 2.1 Blast environment from an airburst, based on Krauthammer (2000).

In the case of a surface burst, the reflection happens instantaneously against the ground surface and a shock wave is created; this is termed a ground-reflected wave, as shown in Figure 2.2. At a short distance from the burst, the wave front can be approximated by a plane wave.

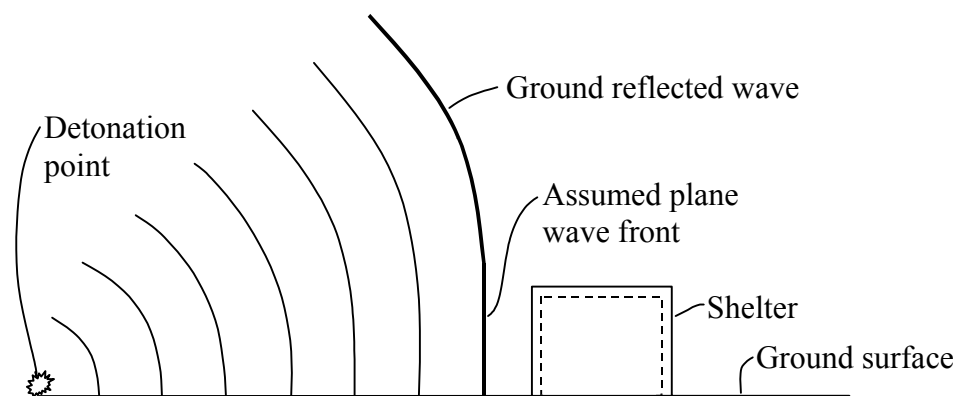


Figure 2.2 Surface burst blast environment, based on Krauthammer (2000).

The pressure–time history of a blast wave can be illustrated with a general shape as shown in Figure 2.3. The illustration is an idealization for an explosion in free air.

The pressure–time history is divided into a positive and a negative phase. In the positive phase, maximum overpressure, P_s^+ , rises instantaneously and decays to atmospheric pressure, p_0 , in the time T^+ . The positive impulse, i^+ , is the area under the positive phase of the pressure–time curve. For the negative phase, the maximum negative pressure, P_s^- , has much lower amplitude than the maximum overpressure. The duration of the negative phase, T^- , is much longer compared to the positive duration. The negative impulse, i^- , is the area under the negative phase of the pressure–time curve.

The positive phase is more interesting in studies of blast wave effects on concrete buildings because of its high amplitude of the overpressure and the concentrated impulse.

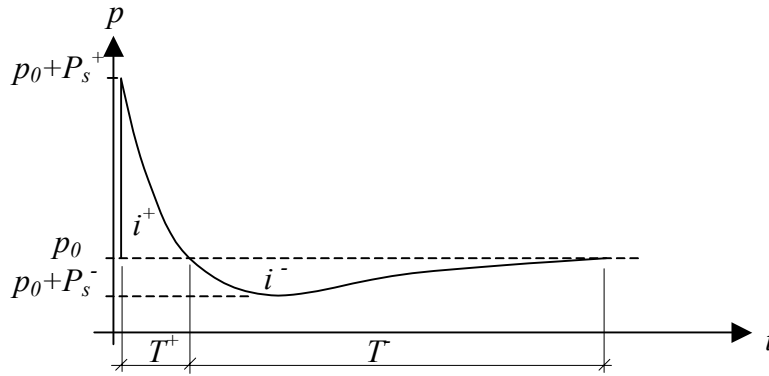


Figure 2.3 Pressure–time history from a blast.

The pressure–time history in Figure 2.3 can be approximated by the following exponential form, first noted by Friedlander (1939) according to Bulson (1997).

$$p(t) = p_0 + P_s^+ \left(1 - \frac{t}{T^+}\right) e^{-bt/T^+} \quad (2.1)$$

where $p(t)$ is the overpressure at time t , and T^+ (the positive duration) is the time for the pressure to return to atmospheric pressure, p_0 . By selecting a value for the constant b , various pressure–time histories can be described. The peak pressure, P_s^+ , is dependent on the distance from the charge and the weight of the explosives. In addition, if the peak pressure, the positive impulse and the positive time duration are known, the constant b can be calculated, and then the pressure–time history is known.

The equation (2.1) is often simplified with a triangular pressure–time curve; see Bulson (1997):

$$p(t) = p_0 + P_s^+ \left(1 - \frac{t}{T^+}\right) \quad (2.2)$$

Conventional high explosives tend to produce different magnitudes of peak pressure. As a result, the environments produced by these chemicals will be different from each other. In order to establish a basis for comparison, various explosives are compared to equivalent TNT values, which can be found in the literature, as in Krauthammer (2000), with the pressure range for different chemicals.

A scaling parameter is introduced, first noted by Hopkinson (1915); see Bulson (1997). With the parameter Z , in equation (2.3), it is possible to calculate the effect of a detonated explosion, conventional or nuclear, as long as the equivalent weight of charge in TNT is known:

$$Z = \frac{R}{W^{1/3}} \quad (2.3)$$

where R is the distance from the detonation and W is the equivalent weight of TNT.

The peak pressure, the positive duration time and the positive impulse are now functions of Z , and the pressure–time history in Figure 2.3 can be described.

$$P_s^+(Z), \frac{T^+}{\sqrt[3]{W}}(Z), \frac{i^+}{\sqrt[3]{W}}(Z) \quad (2.4)$$

In the literature there are several empirical formulas for the expressions in (2.4); see Bulson (1997). In US Army Technical Manual Fundamentals of Protective Design, No. TM5-855-1 (1965) there are tables and diagrams for different types of explosive materials.

2.2.2 Blast wave reflections

When a blast wave strikes a surface, which is not parallel to its direction of propagation, a reflection of the blast wave takes place. The reflection can be either normal reflection or an oblique reflection. There are two types of oblique reflection, either regular or Mach reflection; the type of reflection depends on the incident angle and shock strength.

2.2.2.1 Normal reflection

A normal reflection takes place when the blast wave hits perpendicular to a surface, as shown in Figure 2.4.

The medium has a particle velocity, U_x , before the incident shock wave, U_s , passes the medium; after passage the particle velocity increases to U_p . Furthermore, the overpressure increases from p_x to p_y (p_x refers usually to atmospheric overpressure), the temperature increases from T_x to T_y and the sonic speed increases from a_x to a_y (a_x is approximately 340 m/s in undisturbed air).

When the blast wave hits a rigid surface, the direction will be shifted rapidly, and, as a consequence, the particles at the surface possess a velocity relative to those further from the surface that are still in motion. This relative velocity is equal in magnitude and opposite in direction to the original particle velocity and gives the effect of a new shock front moving back through the air; the reflected shock, U_r . However, since the air conditions have changed, the reflected shock will have different properties. The reflected overpressure increases to p_r , temperature increases to T_r and sonic speed will be a_r .

For shock waves it is common to describe the velocity as a Mach number, which is defined as the actual velocity (of the shock front) in the medium divided by the sonic speed of the undisturbed medium. For example, the shock front will have a velocity with a Mach number M_r into air that had a velocity with M_x at the incident shock.

Incident Shock at M_x Reflected Shock at M_r

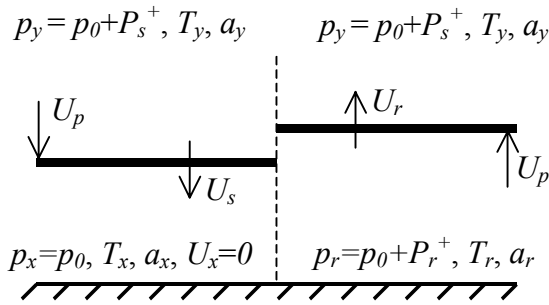


Figure 2.4 Normal reflection in air from a rigid wall, based on Baker (1973).

The properties of the reflected blast wave can be described in terms of a reflection coefficient, defined as the ratio of reflected overpressure to the overpressure in the incident blast wave. It can be shown that for an ideal gas with a specific gas constant ratio of 1.4, the reflection coefficient Λ is, according to Baker (1973),

$$\Lambda = \frac{p_r - p_x}{p_y - p_x} = \frac{8M_x^2 + 4}{M_x^2 + 5} \quad (2.5)$$

From equation (2.5) it can be seen that for a shock front moving with M_x equal to one, i.e. at sonic speed, the reflection coefficient will be two. This means that the overpressure is twice in the reflected blast wave. With increasing speed for the shock front, M_x , the reflection coefficient approaches eight. However, that is for ideal gas with a specific gas constant ratio of 1.4. In a real blast wave, the specific gas constant ratio is not constant, and the coefficient is pressure-dependent; see Johansson (2002). The reflection coefficient increases with increasing pressure.

2.2.2.2 Regular reflection

In a regular reflection the blast wave has an incident shock at M_x with an angle of β and reflection takes place. The reflected shock at M_r has an angle of δ as shown in Figure 2.5. The angle of reflection is not generally equal to the angle of incidence. The air conditions in front of the incident shock (region 1) are still at pressure p_x and temperature T_x . Behind the incident shock (region 2), the air conditions are the same as for free air shock, with pressure p_y and temperature T_y . The air conditions from the reflected shock (region 3), have the pressure p_r and temperature T_r .

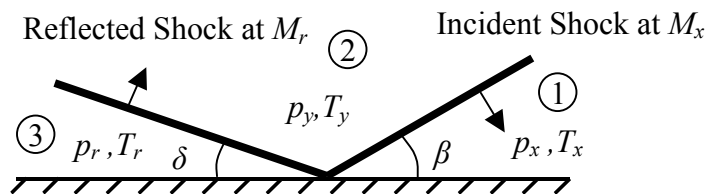


Figure 2.5 Oblique reflection, based on Baker (1973).

2.2.2.3 Mach stem formation

There is a critical angle that depends on the shock strength, where an oblique reflection cannot occur. According to Baker (1973), Ernst Mach [Mach and Sommer (1877)] showed that the incident shock and the reflected shock coalesce to form a third shock front. The created shock front is termed the Mach stem or Mach front, which is moving approximately parallel to the ground surface, as shown in Figure 2.6, with increasing height of the shock front. The point where the three shock fronts meet is termed the triple point. The Mach front and the path of the triple point are also shown in Figure 2.1.

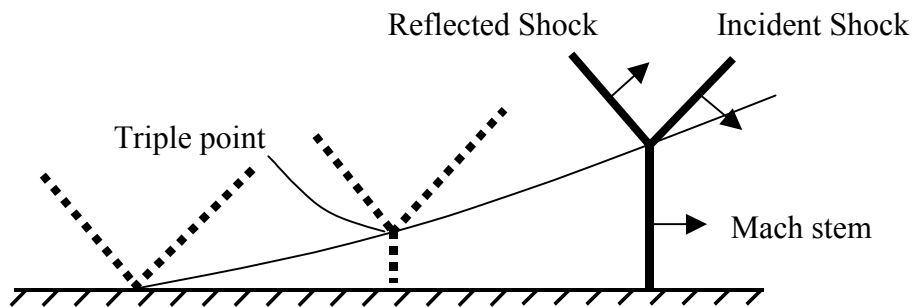


Figure 2.6 Mach stem formation, based on Baker (1973). The arrows indicate the direction of the shock waves.

2.3 Stress waves, reflections and transmission

2.3.1 Stress waves

When a concrete member is subjected to dynamic loading, a stress wave will propagate through it. The stress wave propagates in the longitudinal and the transverse directions in the structure. By using constitutive laws, equilibrium and compatibility the classic wave equation in one dimension for elastic materials can be derived; see Figure 2.7. In real structures when the blast wave or fragment hits the concrete, the concrete behaviour is far from elastic, and the elastic wave equations is not valid. However, the elastic assumption of the classic wave equation illustrates phenomena for concrete in dynamic loading.

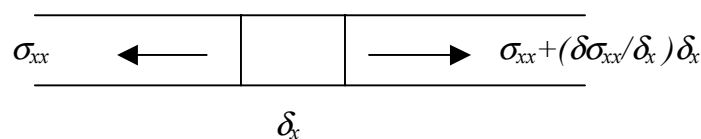


Figure 2.7 Model for one-dimensional elastic wave propagation.

From Newton's second law, the equation of motion, $\sum F = ma$, yields

$$A \frac{\partial \sigma_{xx}}{\partial x} \delta x = \rho A \delta x \frac{\partial^2 u}{\partial t^2} \quad (2.6)$$

where ρ is the density, A is the cross section area, and u is the displacement. By using Hooke's law for the stress $\sigma_{xx} = E \varepsilon_{xx}$, and the definition of strain $\varepsilon_{xx} = \frac{\partial u}{\partial x}$, the classic wave equation can be derived in one dimension:

$$\rho \frac{\partial^2 u}{\partial t^2} = E \frac{\partial^2 u}{\partial x^2} \quad (2.7)$$

and the wave propagates with a velocity of

$$c_0 = \sqrt{\frac{E}{\rho}}. \quad (2.8)$$

For normal concrete the wave propagates with a velocity of approximately 3500 m/s.

The solution to the differential equation (2.7) is

$$u = F(c_0 t - x) + f(c_0 t + x) \quad (2.9)$$

where F and f are arbitrary functions, which are dependent on the initial conditions. The wave's propagation is described by F in the positive x-direction and f in the negative x-direction.

By considering a wave propagating in the negative x-direction, it can be shown, as in Krauthammer (2000), that the particle velocity is

$$\frac{\partial u}{\partial t} = \frac{\sigma_{xx}}{\rho c}. \quad (2.10)$$

The particle velocity is proportional to the stress and indirectly proportional to the acoustic impedance (ρc). The acoustic impedance is the resistance to the wave propagation, where the mass and stiffness are parameters that determine the particle velocity in the medium. By using this model, comparison of concrete and steel shows that the particle velocity is approximately four to five times higher for concrete than for steel.

In three-dimensional space the stress wave propagates faster in the longitudinal direction. For concrete the stress wave propagates in the transverse direction with approximately 60 % of the velocity in longitudinal direction. With three-dimensional wave theory, according to Geradin and Rixen (1994), the longitudinal particle velocity, c_L , becomes

$$c_L = \sqrt{\frac{E(1-\nu)}{(1+\nu)(1-2\nu)\rho}} \quad (2.11)$$

and the transversal particle velocity, c_T , becomes

$$c_T = c_L \sqrt{\frac{(1-2\nu)}{2(1-\nu)}} \quad (2.12)$$

For normal concrete with $E = 29$ GPa, $\nu = 0.2$ and $\rho = 2400$ kg/m³ the wave is propagated in the longitudinal direction with a velocity of approximately 3690 m/s, and in the transverse direction with a velocity of approximately 2260 m/s.

2.3.2 Reflection and transmission of one-dimensional waves

When a stress wave reaches a medium from another medium, the initial wave will be reflected and transmitted at the boundary between these two media. The reflected and transmitted stress waves' amplitudes and velocities depend on the media. The stress wave can propagate as a compressive or tensile wave.

For example, a compressive stress wave in concrete that is propagating will reflect at the boundary. If the boundary is air, the reflected stress will be equal to the incident stress but with opposite sign. This means that the reflected wave will propagate as a tensile wave, since concrete is very weak in tension; the reflected wave can cause scabbing.

Stress wave theory in one dimension explains this type of phenomenon; a model for this theory is shown in Figure 2.8.

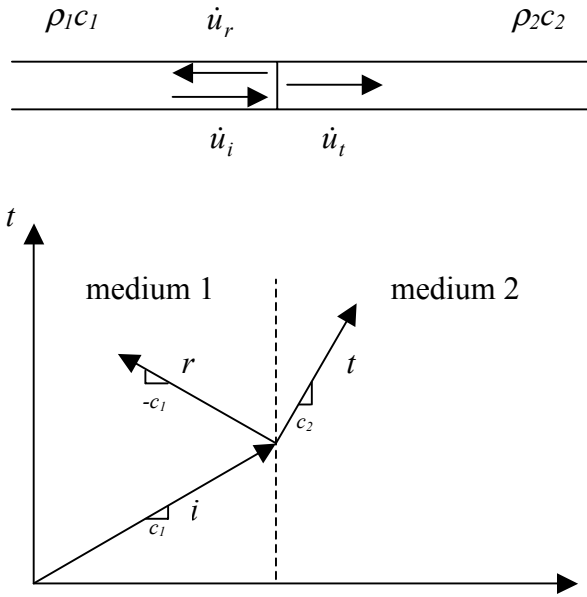


Figure 2.8 Reflection and transmission of one-dimensional stress wave, where i is the incident wave, r is the reflected wave and t is the transmitted wave, based on Krauthammer (2000).

The acoustic impedances (ρc) can be used to characterize the media. For air, the acoustic impedance is approximately zero.

By using equilibrium and compatibility at the boundary it can be shown, as in Krauthammer (2000), that

$$r_\sigma = \frac{I_2 - I_1}{\sum I}, \quad r_{\dot{u}} = \frac{I_1 - I_2}{\sum I} \quad (2.13)$$

$$t_\sigma = \frac{2I_2}{\sum I}, \quad t_{\dot{u}} = \frac{2I_1}{\sum I}$$

where r_σ , $r_{\dot{u}}$, t_σ and $t_{\dot{u}}$ are scalars that describes the changes in reflected and transmitted amplitudes of the stress and velocity, $I_1 = \rho_1 c_1$ and $I_2 = \rho_2 c_2$.

By definition:

$$r_\sigma \equiv \frac{\sigma_r}{\sigma_i}, \quad r_{\dot{u}} \equiv \frac{\dot{u}_r}{\dot{u}_i} \quad (2.14)$$

$$t_\sigma \equiv \frac{\sigma_t}{\sigma_i}, \quad t_{\dot{u}} \equiv \frac{\dot{u}_t}{\dot{u}_i}$$

where

σ_i = initial stress, σ_r = reflected stress, σ_t = transmitted stress,
 u_i = initial velocity, u_r = reflected velocity, u_t = transmitted velocity.

From a blast wave or fragment impact, a compressive stress wave propagates through the concrete member. When the stress wave reaches the backside of the construction, normally air, with acoustic impedance of approximately zero, from equation (2.13), it can be seen that the reflected stress will be equal; it will reflect as a tensile wave, but with the same velocity. The transmitted stress will be zero and double in velocity.

If the stress wave reaches a fixed end, the same stress will be reflected at the boundary with the same velocity and magnitude but with opposite sign.

2.4 Shock waves

By choosing a fixed reference in space (the shock front), where the material motions are derived with respect to that region, the fundamental shock wave equations, known as the Rankine-Hugoniot equations, are derived from the equations for conservation of mass, momentum, and energy in the medium. Consider the one-dimensional model in Figure 2.9, where the material is moving with a velocity of U_0 against the shock front, and the material velocity is U_1 after passing the shock front. The pressure is P_0 and the density ρ_0 before the material reaches the shock front, and the pressure is P_1 and density ρ_1 after passage.

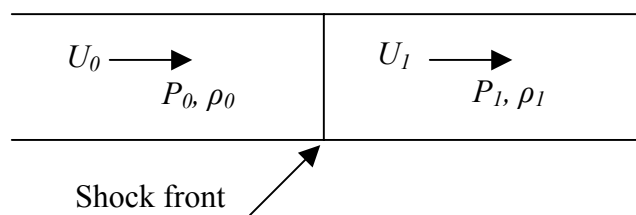


Figure 2.9 Model for one-dimensional shock waves.

Consider the conservation of mass flow per unit time and area in the model in Figure 2.9. It can be expressed for times t_0 and t_1 as

$$m = \rho_0 U_0 A \Delta t = \rho_1 U_1 A \Delta t \Leftrightarrow \rho_0 U_0 = \rho_1 U_1 \quad (2.15)$$

Considering the conservation of momentum, mass times the change in velocity is equal to the impulse of external forces. By using equation (2.15) the conservation of momentum can be derived as

$$m(U_0 - U_1) = P_1 - P_0 \quad (2.16)$$

where m is the flow of mass per time unit and area. The change in internal energy and kinetic energy is equal to the work done by external forces. It can be shown, as in Baker (1973), that the conservation of energy per unit mass can be expressed as

$$E_1 - E_0 = \frac{1}{2}(P_1 + P_0)\left(\frac{1}{\rho_0} - \frac{1}{\rho_1}\right) \quad (2.17)$$

Equations (2.15), (2.16) and (2.17) are the Rankine-Hugoniot equations. The Hugoniot curve expresses the relationship for pressure and specific volume as shown in Figure 2.10. However, the material state is described by a discontinuous jump from one state to another, known as the Rayleigh line.

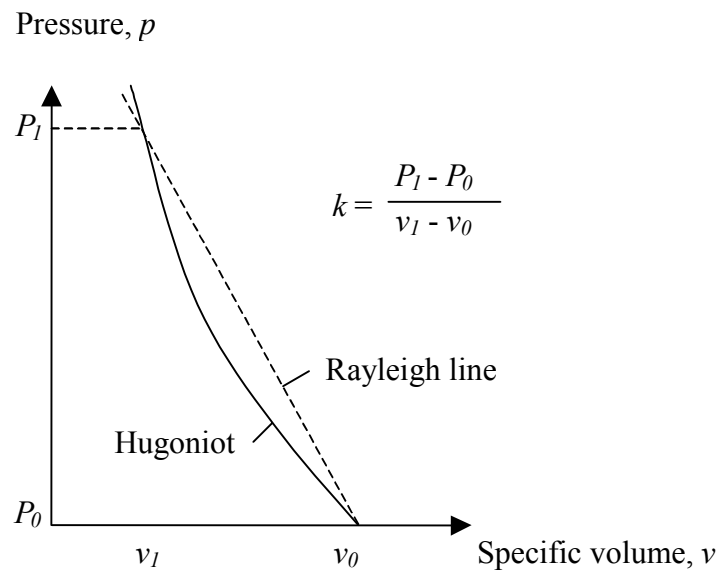


Figure 2.10 Hugoniot curve and Rayleigh line, k is the slope of the Rayleigh line.

3 Concrete under severe loading

3.1 Introduction

To understand the behaviour of concrete structures subjected to severe loading from military weapons, the nature and physics of explosions, the creation of a blast wave and reflections must be known, as described in Chapter 2. Furthermore, fragments will be released from the bomb case, which will fly against the structure. The fragment size, area density (kg/m^2) and striking (impact) velocity are important parameters for the fracture mechanism in concrete. Prediction of the depth of penetration is an important factor for design of protective structures. These subjects will be discussed in this chapter. The effects in concrete slabs loaded by fragments and combined loading of blast and fragment into concrete walls are discussed as well.

3.2 Weapon systems

Weapon systems can be divided into conventional weapons, nuclear weapons, biological and chemical weapons. Nuclear weapons, the most powerful weapon systems in human history, are of two kinds, A-bomb (atomic) and H-bomb (hydrogen). An A-bomb is created by fission of uranium and an H-bomb by fusion of hydrogen. The H-bomb gives much higher energy release than the A-bomb. Biological weapons cause diseases by releasing bacteria or viruses; an example is anthrax. Chemical weapons are direct chemical attacks. An example is mustard gas, first introduced in World War I.

However, the aim in this thesis is to study the effects of conventional weapon attacks in reinforced concrete structures, especially the combination of blast wave and fragments. Conventional weapons are divided into direct and indirect projectiles with and without explosives; see FortH1 (1987). The damage of a direct projectile without explosives is caused by the mass and velocity of the projectile. For direct projectiles with explosives such as grenades, bombs, torpedoes, missiles and robots, the damage is caused not only by the primary kinetic energy from the projectile, but also by the shock wave due to the explosion. Furthermore, fragments are produced from the projectile case, which will fly against the target. Indirect projectiles are weapons that produce a projectile after being discharged.

3.3 Fragmentation

When high explosives such as grenades, bombs, torpedoes, missiles or robots detonate, fragments will fly out in all directions when the case is broken. The fragments from the same kind of weapon can be of different sizes. An example of fragmentation of a 15.5 cm bursting shell is shown in Figure 3.1.




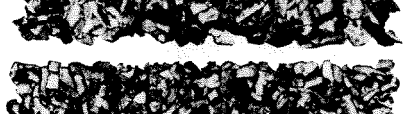


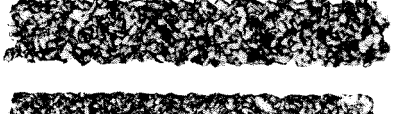
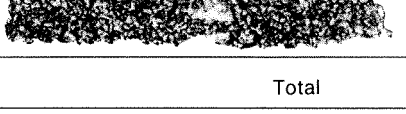
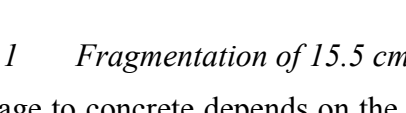
Weight class g		Number of each	Mass g
> 63,5		88	8332
63,5–32,5		186	8078
32,5–15,5		334	7524
15,5–8,5		323	3575
8,5–3,8		520	3020
3,8–2,5		328	1022
2,5–1,5		406	778
1,5–0,5		882	784
< 0,5		–	641
Total		3047	34 758

Figure 3.1 Fragmentation of 15.5 cm bursting shell, based on FortH1 (1987).

The damage to concrete depends on the fragment properties, i.e. the striking velocity, mass and area density. In the literature there are empirical formulas – as Janzon (1978), ConWep (1992), Krauthammer (2000), or FortH1 (1987) – for estimating the velocity of the fragments. Here formulas from FortH1 (1987) are presented.

The initial velocity of the fragments depends on the amount of the explosive material and the size of the case, which can be estimated with equation (3.1), where Q is the charge weight and M_h is the weight of the case.

$$v_i = 2400(1 - e^{-2Q/M_h}) \quad [m/s] \quad (3.1)$$

The fragment velocity is retarded in the air, depending on the initial fragment velocity, the fragment mass and the type of fragment. The velocity is retarded differently after a distance r , and for steel fragments can be calculated as

$$v_r = v_i e^{-0.0456r/\sqrt[3]{m_f}} \quad [m/s] \quad (3.2)$$

where r is the distance, v_i is the initial fragment velocity from equation (3.1) and m_f is the fragment mass. Fragments from an explosion can fly through the air over very long distances, more than 1000 m for heavy fragments; FortH1 (1987).

According to Swedish Rescue Services Agency (1994), a shelter must be able to resist the effect of a 250 kg GP bomb (with 50 weight per cent TNT) that bursts freely outside from a distance of 5 m from the shelter. The fragments masses from a 250 kg GP bomb are normally distributed from 1 to 50 g; FortH1 (1987). By using equations (3.1) and (3.2) the impact velocity at a distance of 5 m varies between 1650-1950 m/s for fragments with mass of 1 to 50 g. In Figure 3.2 fragments velocities from a 250 kg GP bomb are shown for varying fragment weights.

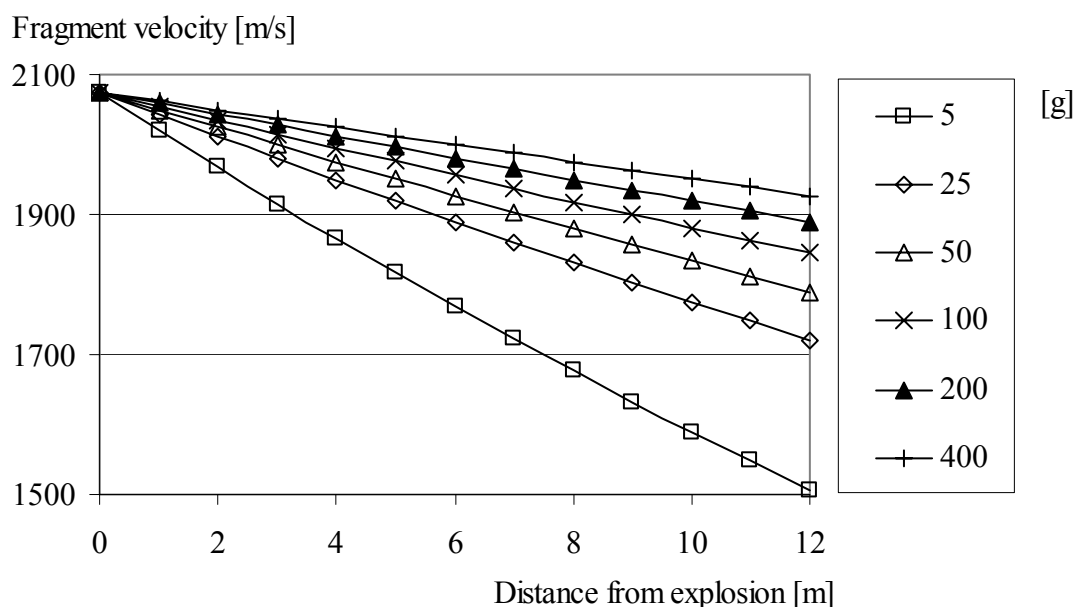


Figure 3.2 Fragment velocity from a 250 kg GP bomb (with 50 weight per cent TNT) that bursts freely outside, for fragment weights from 5 to 400 g, based on equations from FortH1 (1987).

3.4 Penetration with steel fragments into different materials

The depth of penetration depends on the fragment mass, form, velocity and inclination angle of impact, and the material of the target.

For spherical fragments, it has been empirically found by Janzon (1978) that the velocity for perforation at different thicknesses of steel plates is

$$v_p = \frac{t}{\theta \times m_f^{1/3} \times \sin \alpha} \quad (3.4)$$

where θ is a constant depending on the form of the fragment and the target material. The inclination of the impact is α , the mass of the fragments is m_f , and the thickness of the steel plate is t .

An example of penetration with fragments of 15.5 cm bursting shell into soft steel is shown in Figure 3.3, with an impact inclination of 90° .

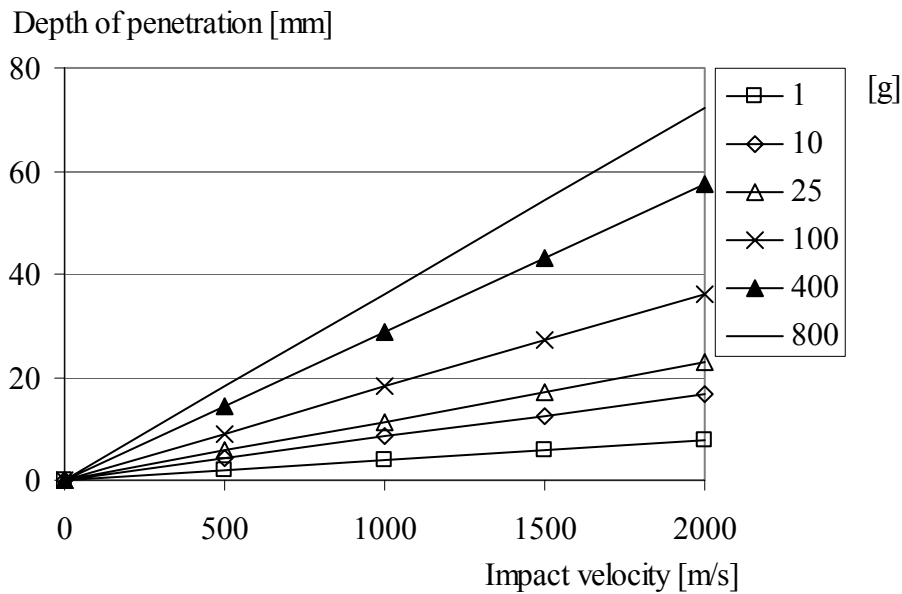


Figure 3.3 Depth of penetration into steel, from equation (3.4), impact inclination 90° , $\theta = 39 \times 10^{-6}$; see Janzon (1978).

Approximate depth of penetration into other materials than steel is given by multiples of the depth of penetration for soft steel by a factor; these factors are given in Table 3.1.

Table 3.1 Penetration depth of common materials, FortHI (1987).

Material	Factor
Armour-plate	0.75
Soft steel	1,0
Aluminium	2
Reinforced fibre-glass plastic	4
Concrete (K40, reinforced)	6
Pine wood	15
Sand	18
Water	50
Wet snow	70
Dry snow	140

By using a direct formula, in Krauthammer (2000), the depth of penetration can be estimated for fragments penetrating massive concrete, as shown in Figure 3.4. For equations, see the Appendix D. The depth of penetration is a function of the fragment weight, the striking velocity and the concrete compressive strength.

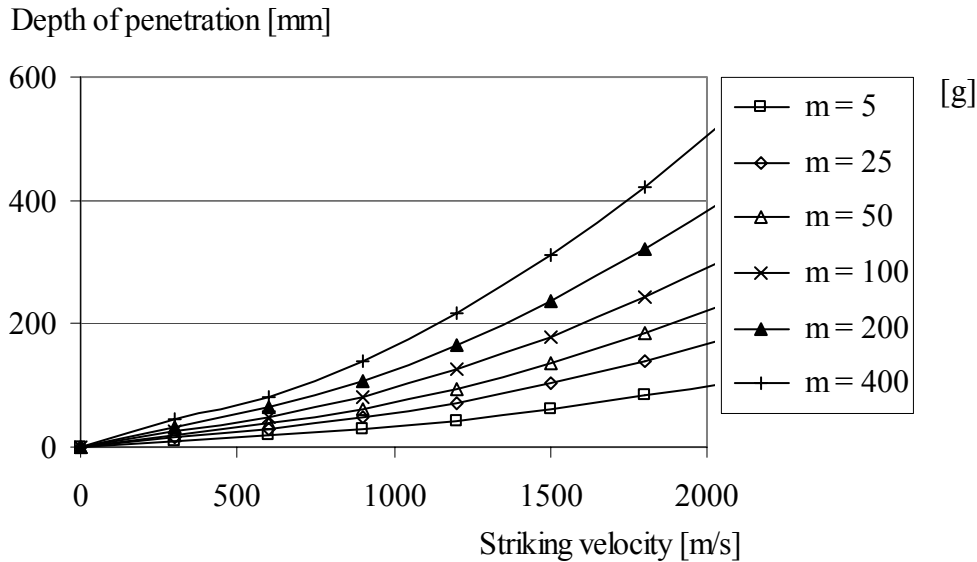


Figure 3.4 Penetration of fragments into massive concrete, compressive strength 30 MPa, for fragment weights from 5 to 400 g with striking velocities up to 2000 m/s, based on equations from Krauthammer (2000).

In Figure 3.4 the penetration depth for fragments into massive concrete is shown. However, for a concrete structures, for 70 % penetration, perforation may be expected; see Krauthammer (2000).

According to Swedish Rescue Services Agency (1994), shelter above ground must have a minimum thickness of 350 mm. For the normally distributed (1–50 g) fragments from a 250 kg GP bomb with 125 kg TNT, perforation will not be a problem. However, if single fragments of large size are released from the bomb, perforation may become a problem.

Table 3.2 shows the required thickness of a concrete wall to just prevent perforation for fragment weights from 5 to 400 g with striking velocities up to 3000 m/s. As seen, both the striking velocity and the mass are important factors for the design of protective structures. The area marked grey gives a thickness above 350 mm massive concrete (the required minimum thickness of a civil defence shelter above ground). For equations, see the Appendix D.

Table 3.2 Thickness of concrete wall that just prevents perforation, compressive strength 30 MPa, for fragment weights from 5 to 400 g with striking velocities up to 3000 m/s, based on equations from Krauthammer (2000).

Striking velocity [m/s]	Fragment mass [g]					
	5	25	50	100	200	400
300	22	39	50	65	84	108
600	30	54	70	91	118	153
900	39	74	97	127	167	220
1200	53	101	134	177	235	312
1500	70	135	180	239	318	424
1800	90	175	233	312	416	556
2100	112	220	295	394	528	707
2400	138	271	363	487	653	877
2700	166	327	439	590	792	1064
3000	196	389	522	702	943	1268

3.5 Spalling and scabbing

Concrete has a high compressive strength but is very weak in tension. The fragment or projectile impact will cause severe cracking and crushing in the concrete, which must be supported by reinforcement in order to prevent failure. When a fragment or a projectile hits a target of concrete, it will penetrate into the concrete and the impact will cause crushing of the material at the point of contact (spalling) and possible scabbing on the backside of the wall; see Figure 3.5. When 50 % penetration is achieved, scabbing will become a problem; see Krauthammer (2000).

The cause of scabbing is the reflected shock wave (tensile wave). The amount of reinforcement is a very important parameter in regard to scabbing. Experiments shows that the scabbing is reduced by increasing the amount of reinforcement – see Jonasson (1990) – since the reinforcement will hold the concrete intact (confinement effect).

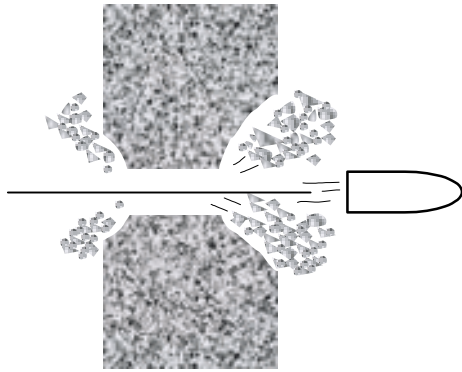


Figure 3.5 Spalling and scabbing, based on FortHI (1987). Spalling in the front of the concrete wall and scabbing at the backside of the wall.

3.6 Concrete penetration with steel projectiles

Reinforced concrete structures for military protection have been the most widely used material. Protective structures in concrete have been built since the beginning of the 20th century. During and after World War II there were large research projects for studying penetration effects on concrete.

Poncelet (1829), according to Bulson (1997) is known as the first who came up with a penetration formula for projectiles. He assumed that the course of forces between the projectile and the target was a function of the projectile weight, diameter, nose shape, impact velocity, v_i , and two parameters that took account of the target material.

Since Poncelet there has been further development of the formulas by Beth (1943), Bergman (1950), Hughes (1984) and Forrestal *et al.* (1994), but the same basic idea has been used. The depth of penetration is a function of the impact velocity of the projectile with a general form of

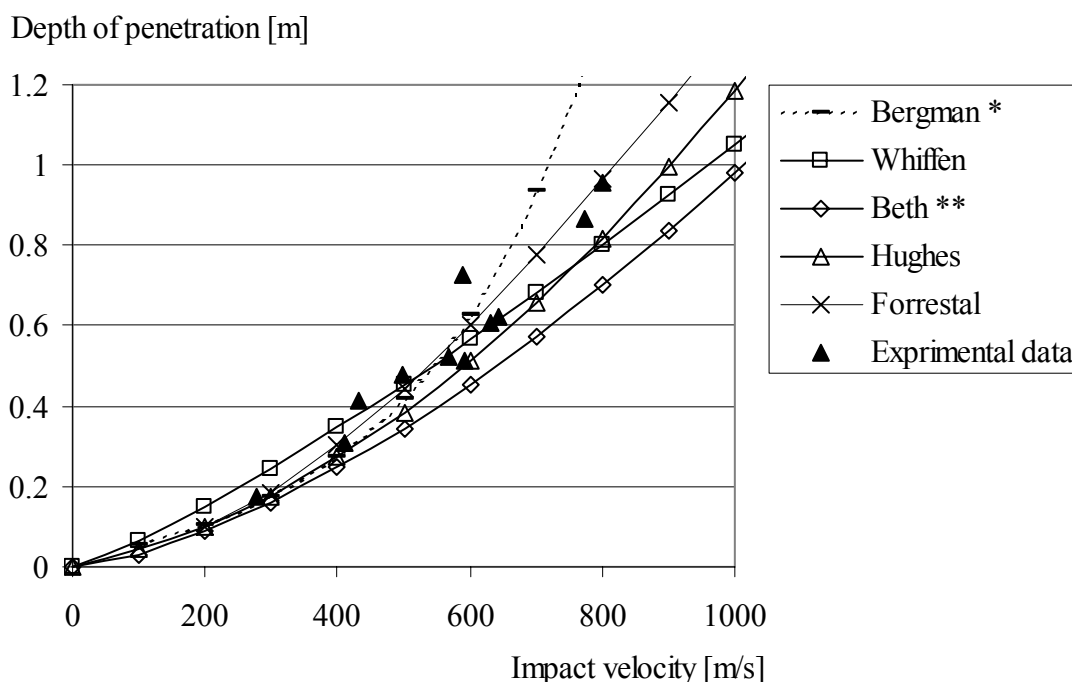
$$x = C \times f(v_i) \quad (3.5)$$

where x is the depth of penetration, and C is a constant which depends on the projectile mass, the nose shape of the projectile, the diameter of the projectile and a parameter that takes account of the target material. For concrete this last parameter is normally related to the compressive strength.

For the empirical formula developed by Bergman (1950) see the Appendix C. The work published by Beth (1943) was later incorporated in the US Army Technical Manual on the Fundamentals of Protective Design (1965); see Appendix C. The formula used in the manual had been further developed.

Hughes (1984) derived an empirical formula; see Appendix C. He used the same principal ideas that Bergman and Beth used, i.e. that the depth of penetration was dependent on the projectile mass, the nose shape of the projectile, the diameter of the projectile and a parameter that takes account of the target material. However, Hughes used the tensile strength of the concrete as a parameter, whereas Bergman and Beth had used the concrete compressive strength. Furthermore, the concrete strength depends on the strain rate. This approach gives more realistic behaviour of the concrete. Forrestal *et al.* (1994) derived an analytical formula for penetration into concrete; see Appendix C.

The formula developed by Forrestal gives the most accurate prediction of the depth of penetration; the agreement with experimental data is good for wide range. The empirical formulas from the time around World War II cannot predict the depth of penetration for as wide a range of data as Forrestal. Here a comparison for a 0.906 kg projectile impacting a concrete target, with varying striking velocity has been performed with the different empirical formulas; see Figure 3.6. This experimental series has been compared with FE analyses in Chapter 6.



* Experiments out of limitations of the empirical formula.

** The Formula is based on Beth's work (1943).

Figure 3.6 Penetration data and comparison with empirical relationships for prediction of 0.906 kg, 26.9 mm projectile impacting concrete with a compressive strength of 36 MPa.

3.7 Concrete slabs loaded with steel fragments

FOA¹ made a series test of fragment-loaded concrete slabs; see Nordström (1992), Nordström (1993) and Nordström (1995). The experiments were made in scale 1:4. The aim with the experimental series was to investigate the effects against concrete slabs loaded with fragments of different size, velocities, form and area density. In the experimental series the energy absorption capacity was calculated for undamaged and damaged (pre-loaded by fragments) slabs. After each shot, the slabs were cleaned and loaded with a point load, the deformation was measured, and the energy absorption was calculated as the area under the load–deformation curve.

¹ Försvarets Forskningsanstalt, in English: National Defence Research Establishment.

In general, the experimental results showed that the slabs which were damaged had a lower maximum capacity than undamaged slabs, and that with increasing fragment area density the maximum capacity decreases. The maximum capacity was reduced for the pre-damaged slabs, and with increasing area density the capacity decreased since the craters from the fragments are so many that they coincide and the slab thickness is reduced.

During the loading, the deflections were measured. For small deflections (25 mm) of the concrete slab, the energy absorption was higher for undamaged slabs and for slabs with small fragment area density (0.10 kg/m^3) than for slabs with higher fragment area density (above 0.10 kg/m^3); see Figure 3.7. This is due to the maximum capacity, which is reduced for the concrete slabs that had higher fragment area density. The fragment area density from a 250 kg GP-bomb at distance of 4 m in scale 1:4 is approximately 0.2 kg/m^3 , according to Nordström (1995).

However, for further loading, the energy absorption was lower for the undamaged slabs at a deflection of 100 mm; see Figure 3.7. This is explained by the fact that for pre-damaged slabs the behaviour is much more ductile; this can be attributed to the cracking and shaking of the slabs before loading with the point load. The reinforcement can yield at several points at the same time and the behaviour becomes more ductile. For undamaged slabs the cracks in the concrete are normally localized under the point load and the reinforcement yields locally. Another cause is that the bond between reinforcement and concrete has been lost or reduced due to the shaking and vibration of the slab after a shot with fragments, and the reinforcement slides in the slab.

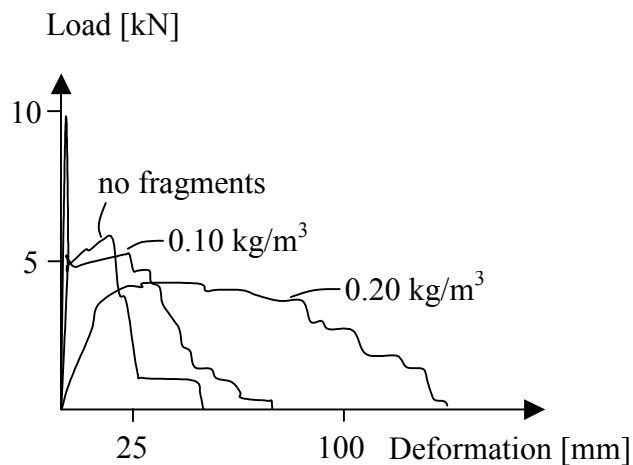


Figure 3.7 Schematic load–deformation relationship for undamaged slabs, with fragment area density of 0.10 kg/m^3 and 0.20 kg/m^3 , based on results from Nordström (1995).

3.8 Combined blast wave and fragment loading

A building is not only exposed to fragments or only a blast wave; from a bomb the loading is a combination of both the blast wave and fragmentation. Experiments show that a concrete buildings which is exposed to a combination of blast wave and fragments will collapse more easily than one which is exposed only to a blast wave or fragments; see Forsén and Edin (1991).

The load from a detonation can be divided into a blast wave and a stress wave, which is caused by the direct impact from the fragments. Depending on the charge and the distance between the bomb and the target, the fragments may impact the concrete surface before, at the same time or after the blast wave. Figure 3.8 shows an example of a 250 kg GP bomb (with an equivalent charge weight of 125 kg) with the arrival time for the blast wave calculated with ConWep (1992), and the arrival time for the fragments; see equation (3.2). For a 250 kg GP bomb the arrival times for the blast and the fragments are the same for a distance of approximately 5 m, and for a distance above that the fragments will impact the target before the blast wave.

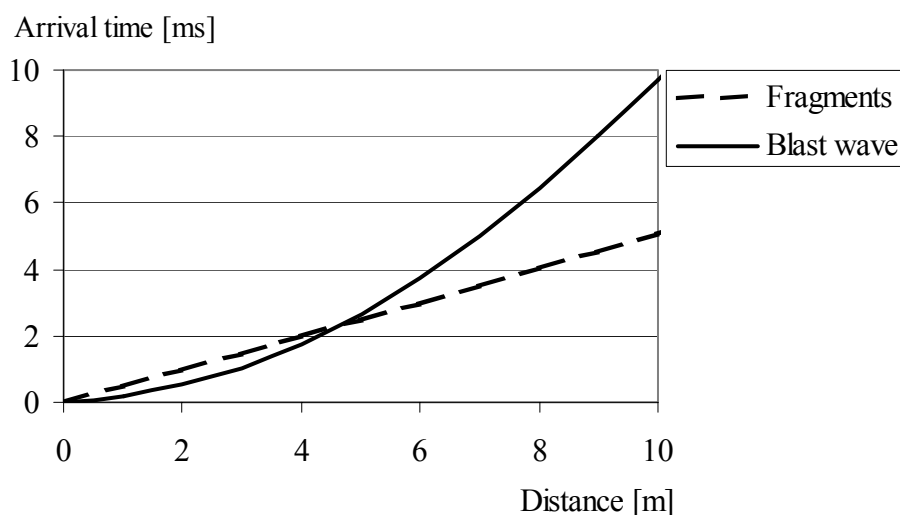


Figure 3.8 Arrival time for blast wave and fragments from a 250 kg GP-bomb.

The difference in arrival time between blast and fragments is not so important at short distances; see Forsén and Nordström (1992). This is due to the fact that the response time of the reinforced concrete wall is usually very long compared to the difference between arrival times of blast and fragments. The wall is going to be damaged by the fragments before it has started moving. A very good estimation of the deflection can be made by simply superposing the fragment impulse on the positive impulse of the blast wave, with the maximum blast pressure, and rearing it to a triangular shape and considering the resistance to be decreased by the fragments from the very beginning of the load; see Forsén and Nordström (1992).

In an experimental series carried out by Forsén and Edin (1991), reinforced multi-storey concrete buildings were studied. Different structural solutions were analysed, with reinforcement in each storey that was either non-continuous or continuous to the next storey, and with and without inner walls. To simulate the load from storeys

higher up in the building, which cause a normal force in the wall, a load of 800 kg was placed above the wall. The weight of the load corresponds to a building approximately six storeys high.

The reinforcement was arranged in four different ways. Type 1, weak reinforcement; the reinforcement was not continuous in the wall between two storeys. Type 2, strong reinforcement: continuous through the building. Type 3 was weak reinforcement with a structural solution that has inner walls perpendicular to the outer wall. Type 4 was strong reinforcement with inner walls, which are perpendicular to the outer wall.

The experiments were made in scale 1:4. The charge was simulated as a 250 kg GP bomb in full scale, scaled with 1:4 in the experiments. An example of the results from the study is shown in Figure 3.10.

Earlier experiments at FOA, according to Forsén and Edin (1991) showed that walls exposed only to a shock wave differed little with weak and strong reinforcement. However, the damage when combining blast and fragment at the same time is much higher than with only a blast.

The fragment impulse density is relatively small compared to the positive impulse density of the blast wave, as seen in Figure 3.9.

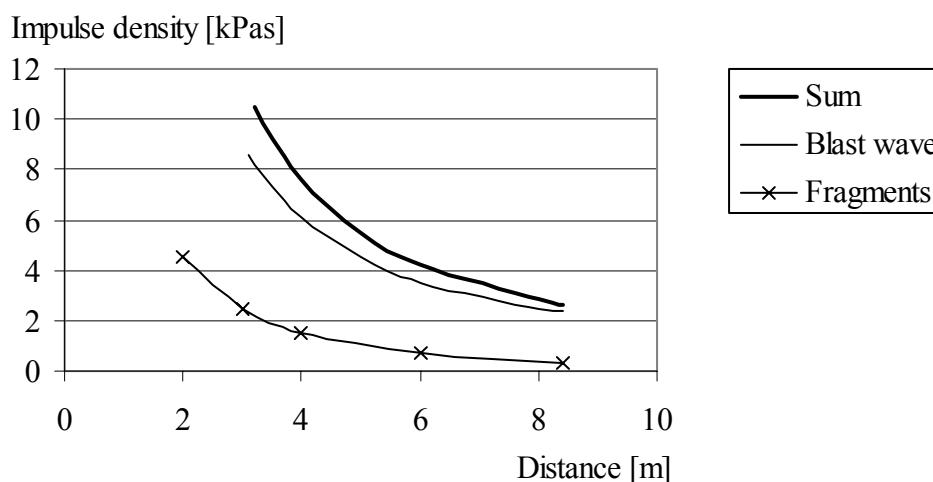


Figure 3.9 Impulse density of blast and fragments. At level 5.4 kPas, collapse is expected for a 150 mm concrete wall; based on results from Forsén and Edin (1991).

The increase in the impulse density does not explain the higher damage of the structure, since the increase is relatively small. The damage mechanisms are not known in detail. The increased damage is explained by the following. The resistance to horizontal displacement depends on the normal force in the wall. When the wall is subjected to a blast, it will have a sudden displacement and the mass above will accelerate; this will increase the normal force. By taking account of the accelerating mass and the reduced cross section, the combination of blast and fragment loading gives a more unsafe construction.

In addition, inner walls perpendicular to the outer wall increase the stiffness of the wall. In the study it was concluded that the inner walls had a great resisting effect. Comparison of the horizontal wall velocity shows that the walls without the inner wall perpendicular to the outer wall had the highest velocities. The weak reinforcement will give higher horizontal velocities.

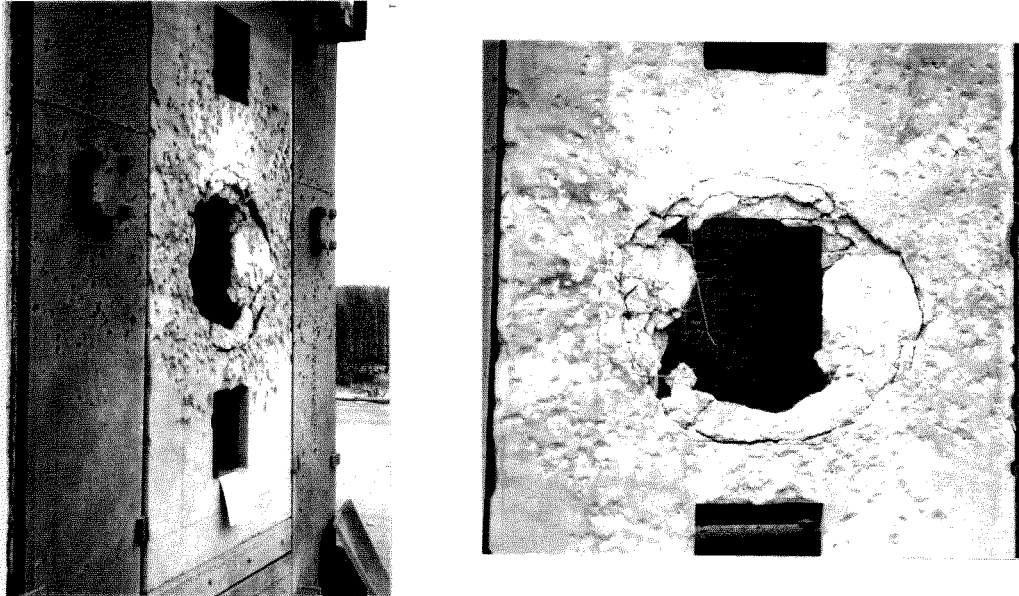


Figure 3.10 Damage after blast, heavy reinforcement, with inner walls; Forsén and Edin (1991).

A detonation inside a building will give more damage than if the detonation were outside the building. This is due to the fact that, besides the short duration of a blast wave, a long-duration blast wave will be added by gas and heat from the explosion, which cannot leak out from the limited space. If the amplitude and the duration of the pressure are high, the walls and roof may jerk. An important parameter with cased buildings is the relationship between openings, the so-called leakage area. With large leakage areas the duration can be shortened and the damage possibly reduced.

Forsén (1989) studied the effects of cased buildings. The experiments showed that the walls were not broken into small pieces by charges without fragments; see Figure 3.11. The walls were jerked in almost whole pieces. Charges with fragments showed a different behaviour; the walls were crushed at the height of the charge, and were still standing after the explosion as shown in Figure 3.12.

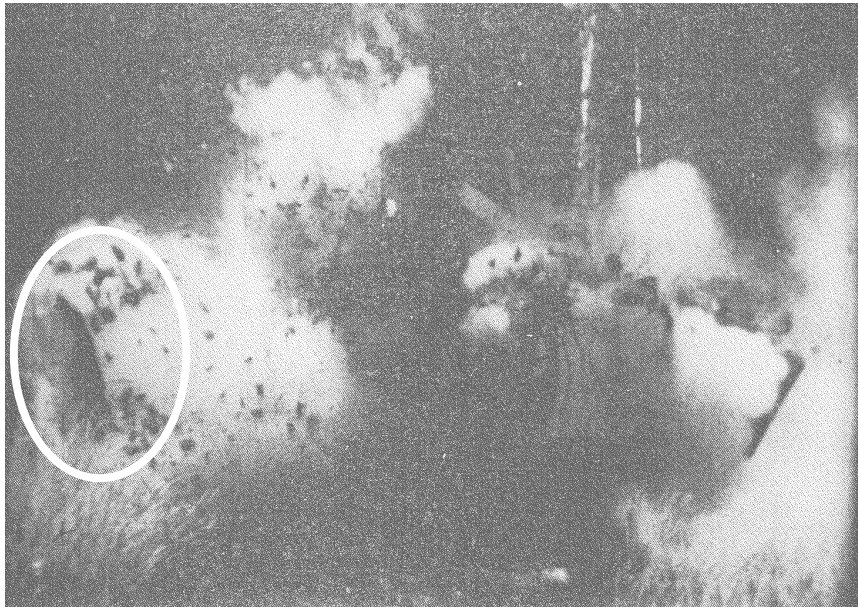


Figure 3.11 Blast wave without fragments, based on Forsén (1989). The marked area shows a wall that is jerked in almost one piece.

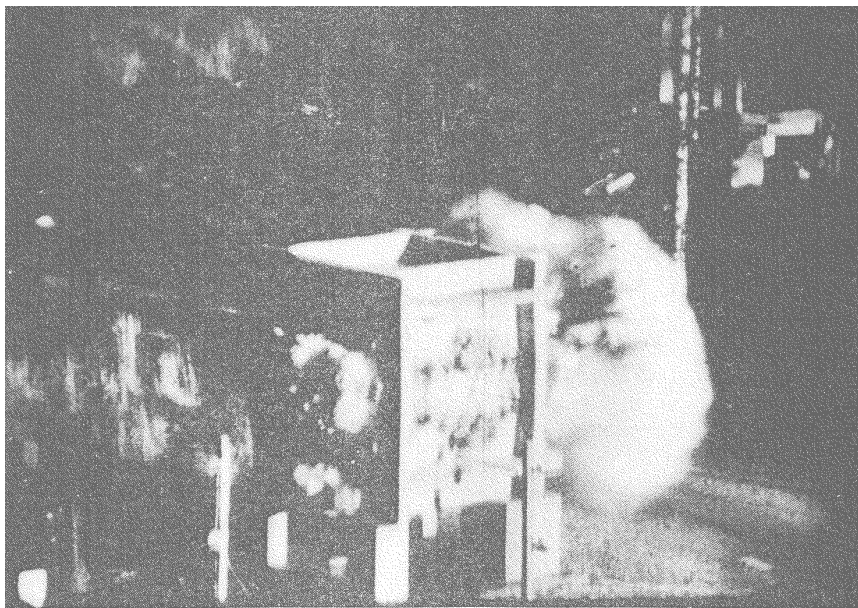


Figure 3.12 Blast wave combined with fragments; Forsén (1989).

4 Behaviour of concrete under dynamic loading

4.1 General

The behaviour of concrete differs in dynamic loading compared to static loading. The initial stiffness, as well the ultimate strength, increases in both compression and tension. Furthermore, the concrete strain capacity is extended in dynamic loading.

Under severe loading, when a projectile or fragments hit a concrete target, the concrete will crush and crack, and the structure will shake and vibrate. The pressure at the front of the nose of the projectile is several times higher than the static uniaxial strength of concrete, also the lateral confining pressure. In addition, a stress wave is propagating from the tip of the nose of the projectile. In front of the nose of the projectile, the impact may cause crushing. Since concrete is very weak in tension, the tensile wave obtained when the compressive wave hits the backside of the wall may cause scabbing at the backside, and cracking in the lateral direction. Both the compressive strength and the tensile strength of concrete are important parameters for the depth of penetration. Moreover, the crater size depends on the tensile strength. The material behaviour of concrete in dynamic loading is discussed in this chapter.

At Delft University, Zielinski (1982) followed a phenomenological approach where he compared static and impact tensions. He observed a changing geometry of the fracture plane. With increasing loading rate, the amount of aggregate fracture increased. Furthermore, multiple fractures were observed at high loading rates, as shown in Figure 4.1.

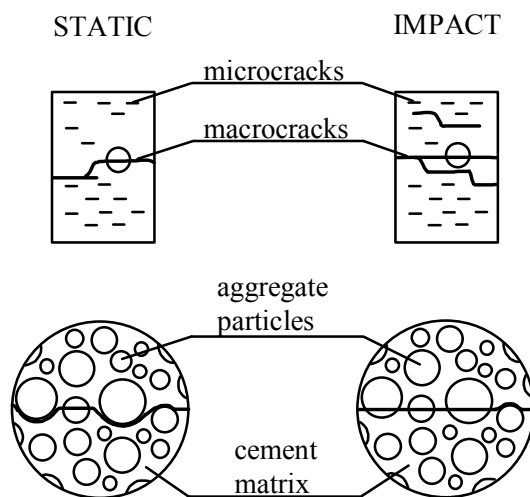


Figure 4.1 Crack path for tensile static and dynamic loading; based on Zielinski (1982).

These fracture mechanisms have a direct influence upon the stress–strain relationship for concrete in dynamic loading; the energy absorption is much higher for the multiple fracture planes. Furthermore, the stiffness is increased; stress levels at failure for high loading rates and deformation capacity increase. In addition, the elastic stiffness is increased. This is schematically shown in Figure 4.2.

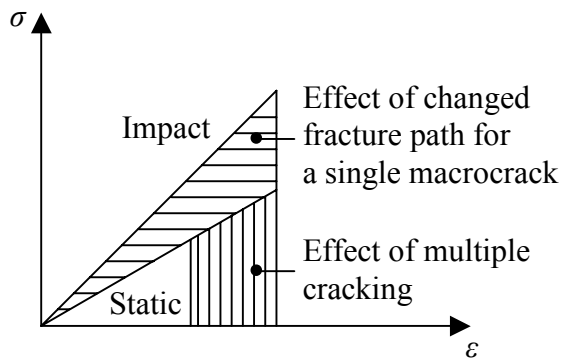


Figure 4.2 Schematic view of the effect of fracture mechanisms on the stress – strain relationship, based on Zielinski (1982).

4.2 Behaviour of concrete under static loading

Concrete is often characterized with the uniaxial stress–strain relationship as shown in Figure 4.3. For normal-strength concrete, the ultimate tensile strength is less than one tenth of the ultimate compressive strength.

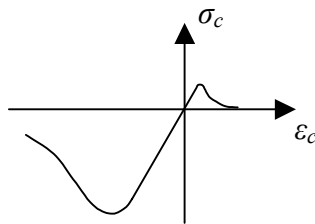


Figure 4.3 Concrete stress–strain relationship under uniaxial loading.

However, real structures are subjected to multiaxial stresses. Confined concrete has increased strength and stiffness, and furthermore, strains are extended. In Figure 4.4 the stress–strain relationship for concrete in compression is shown for increasing lateral pressure (confined concrete).

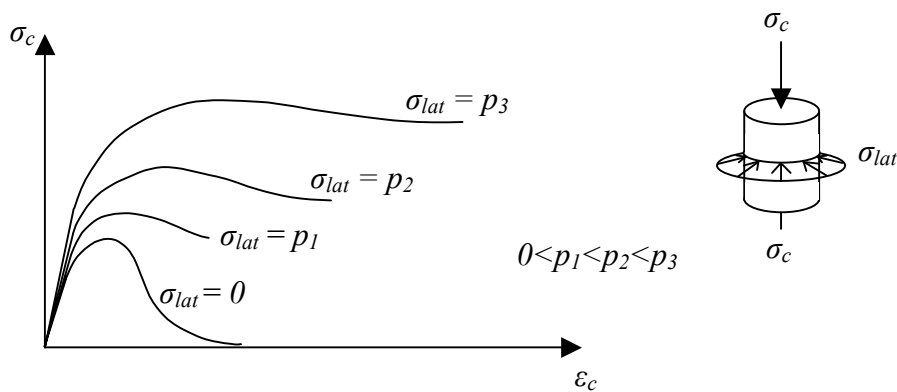


Figure 4.4 Schematic view of stress–strain relationship increasing lateral pressure for concrete in compression.

When concrete is subjected to very high pressures as in an impact situation, the lateral pressure will increase. Under the nose of the missile, concrete is exposed to enormous confining pressures and behaves plastically, dissipating a large amount of energy. In addition, civil defence shelters have heavy reinforcement, which gives further confinement effects. The confining pressure in impact loading can be several hundreds MPa. In a standard static tri-axial test, the ultimate strength of concrete can increase enormously. Experiments by Bazant *et al.* (1986), with a uniaxial compressive strength of 46 MPa, showed that the ultimate strength increased up to 800 MPa, and the strains were extended as shown in Figure 4.5.

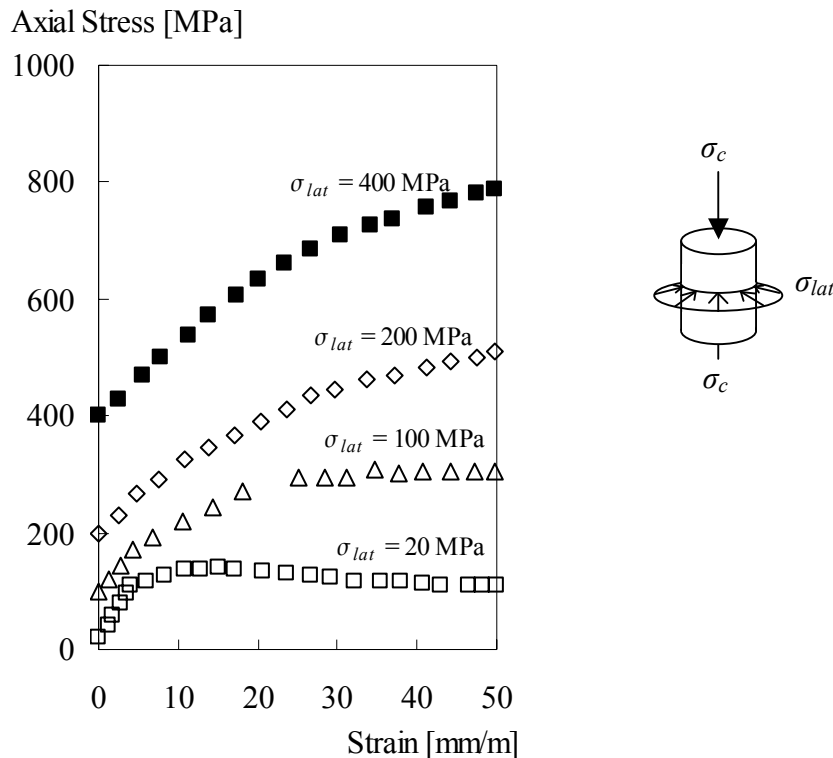


Figure 4.5 Stress–strain relationship for confined concrete; based on triaxial compression test data from Bazant *et al.* (1996).

Concrete is very weak in tension; the ultimate tensile strength is less than one tenth of the ultimate compressive strength. When concrete cracks, the tensile strength has reached a maximum and thereafter decreases quickly (tensile softening). The ultimate tensile strength is hardly affected by lateral compression as concrete in compression. This is further discussed in section 4.4.2.

4.3 Strain rate effects for concrete under uniaxial loading

The behaviour of concrete depends on the loading rate; this is called the strain rate effect. The strain rate in the material depends on the loading case, as shown in Figure 4.6 for different loading cases such as creep, static, earthquake, hard impact and blast loads.

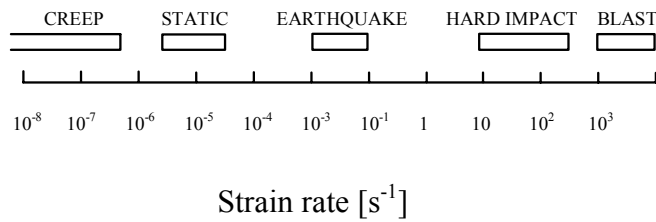


Figure 4.6 Strain rates on different loading cases; based on Bischoff and Perry (1991).

The strength, deformation capacity, and fracture energy are important parameters for characterizing and describing the response of concrete. For dynamic loading, these parameters change relative to static loading. When concrete is subjected to impact loading, the material strength will increase. The dynamic increase factor (*DIF*) is the proportional increase of the dynamic ultimate strength relative to the static ultimate strength. For dynamic loading, the ultimate compressive strength can be more than a doubling. Compilations by Bischoff and Perry (1991) show the relative change in the ultimate strength for concrete in uniaxial compression; see Figure 4.7.

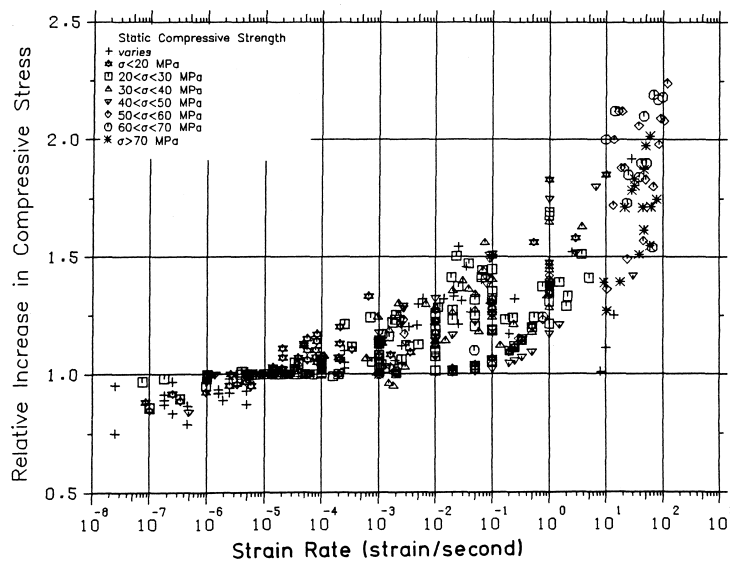


Figure 4.7 Relative increase in the ultimate uniaxial compressive strength as function of the strain rate; Bischoff and Perry (1991).

Additionally, according to Ross *et al.* (1996) the concrete ultimate uniaxial strength in tension increases by multiples of 5 to 7 at very high strain rates, as shown in Figure 4.8.

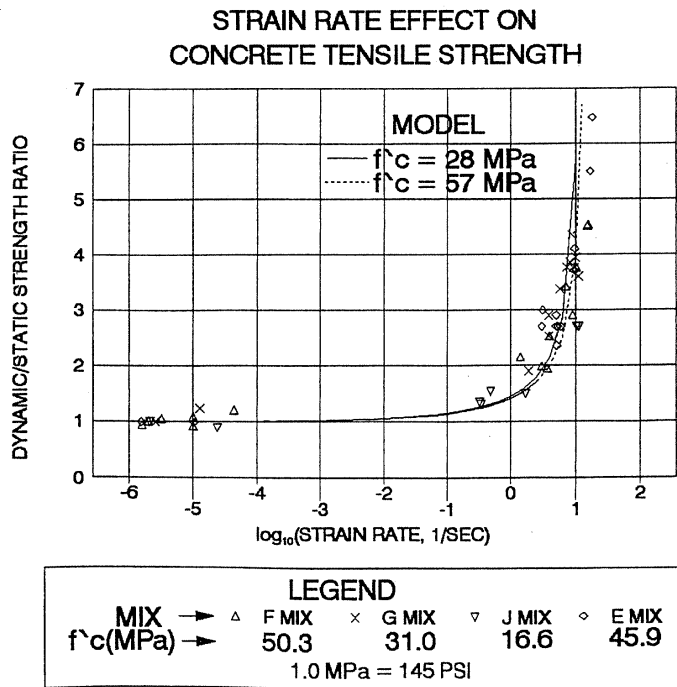


Figure 4.8 Strain rate dependency for concrete in tension; Ross *et al.* (1996).

Dispersions in the test results are explained by the difficulties of measurement in dynamic tests, and the method of testing is altered. Another explanation is that the amount of moisture in the concrete influences the viscous effects of concrete. Wet concrete is more sensitive to strain rate than dry concrete; see Ross *et al.* (1996).

The increased strength is explained by the change in the fracture plane. With increased loading rate, concrete will have multiple fractures and the amount of aggregate fracture increases; see Figure 4.1.

The viscous effects are explained by the following. When concrete is subjected to compressive loading, the pores tend to close. Because of the water, viscous effects develop an inner pressure in the pores that are filled with water, which gives an increasing strength of the material. When loading parallel to the pores, a resistance force is created; see Rossi and Toutlemonde (1996). For concrete in tension, the resistance force is created when the pores are opening. The *DIF* curve has a flat part and a steep part; see Figure 4.7 and Figure 4.8. For concrete in tension, when the strain rate is less than approximately 1 s^{-1} the viscous effects dominate, and when the strain rate exceeds approximately 10 s^{-1} the forces of inertia dominate. For concrete in compression, the forces of inertia dominate at strain rates of approximately $60\text{--}80 \text{ s}^{-1}$; see Ross *et al.* (1996).

4.4 Strain rate effects of confined concrete

The research in the area of strain rate effects has been focused mainly on uniaxial loading conditions. For multiaxial loading conditions, the relevant research has been done by Takeda *et al.* (1974), Zielinski (1982) and Weerheijm (1992). In real structures as blast shelters, the concrete members are in a multiaxial state of stresses; therefore, material behaviour in impact loading situations under multi-axial loading conditions at high rates must be known.

4.4.1 Strain rate effects of confined concrete in compression

Takeda (1974) demonstrated that the rate effects for confined concrete in compression are consistent at various compression levels, as shown in Figure 4.9. The static condition (S) has a strain rate of approximately 10^{-6} s^{-1} , the intermediate condition (III) has a strain rate of approximately 10^{-2} s^{-1} , and the impact condition (I) has a strain rate of approximately 1 s^{-1} . From the static tests, it can be seen that the ultimate strength is increased with increasing lateral pressure. For intermediate and impact conditions, the increase in ultimate strength is a combination of lateral pressure and strain rate effects; the increase is proportional to the static tests, according to Takeda.

However, in the case of impact condition (I) for increasing lateral pressure, it seems from Figure 4.9 that the increase in ultimate strength is no longer proportional.

No experiments have been done to the author's knowledge, on confined concrete behaviour at high strain rates, where the forces of inertia dominate. Similar tests with higher strain rates would therefore be very interesting.

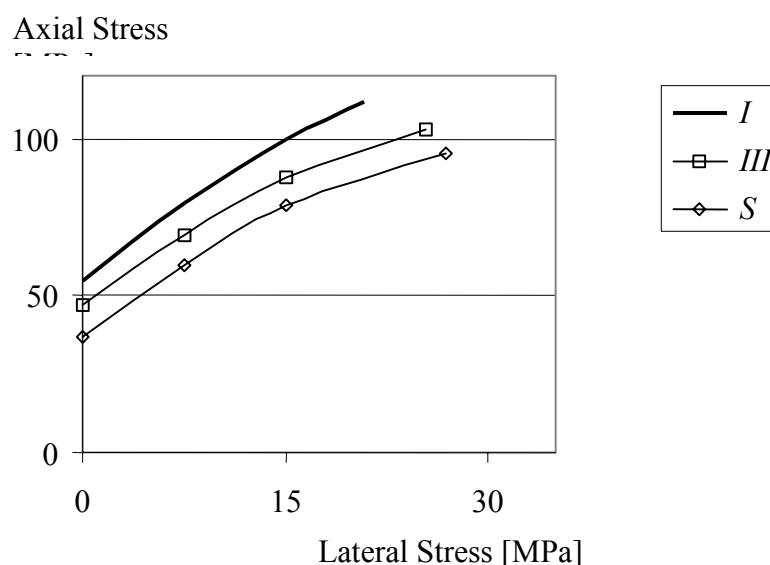


Figure 4.9 Confined concrete, strain rate dependency; based on Takeda *et al.* (1974). Curves: Impact (I), intermediate (III) and Static conditions (S).

4.4.2 Strain rate effects of confined concrete in tension

Zielinski (1985) performed a series of tests where the loading condition consisted of static lateral compression and axial static or impact tensile loading. In the static tests, the axial tensile force was gradually increased up to failure; the rate of loading was approximately 0.1 N/mm²/s. In the impact tests, a drop-weight was used and the rate of loading was about 10⁴ N/mm/s. In Figure 4.10 the ultimate tensile strength is shown for either static compression – static tension or static compression – impact tension. The results show that, at all levels of compressive stress tested, the impact tensile strength of concrete is higher than the strength with the static load. However, the ultimate tensile strength of concrete is hardly affected by lateral compressive stresses up to about 0.7 of the concrete cylinder strength. The lines that are plotted in Figure 4.10 correspond to the Mohr-Coulomb failure envelope.

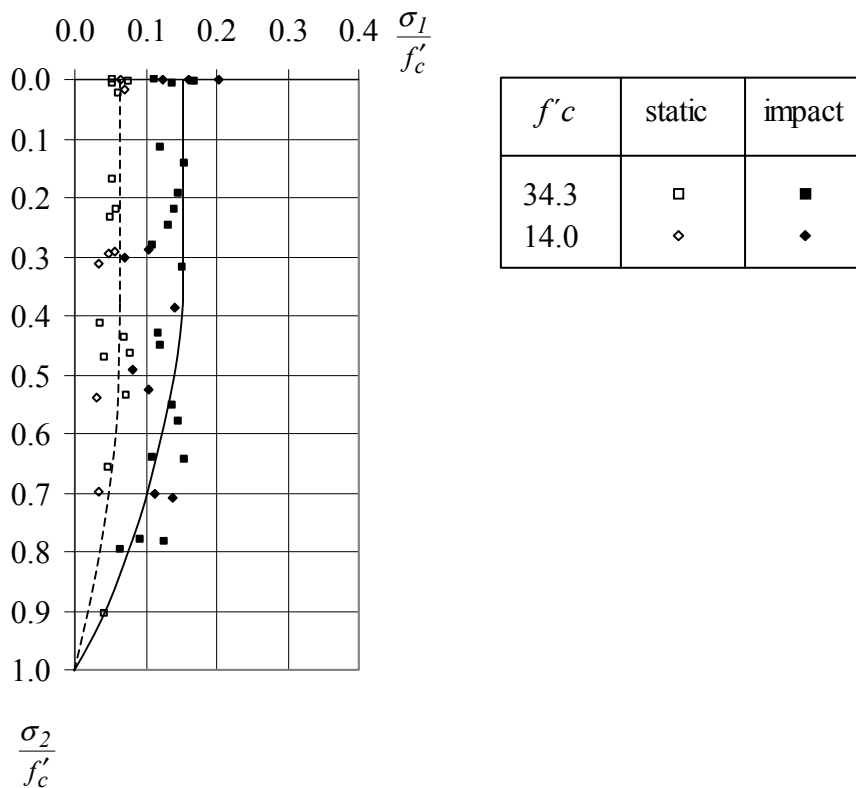


Figure 4.10 Strength of concrete under biaxial compression–tension. Test results; based on Zielinski (1985). Lines correspond to the Mohr-Coulomb failure envelope.

Furthermore, for high static lateral compression, the strains are extended for both static and impact tensile loading. And for low static lateral compression, the strains are barely affected; see further Zielinski (1985).

5 FE modelling of concrete under severe dynamic loading

5.1 Introduction

The development of computers during recent decades has created the possibility to use the finite element (FE) method for severe dynamic loading such as blast waves, or for penetration analyses of concrete. In this chapter it is described how to use the FE method for this type of loading situations.

In this thesis the non-linear FE analyses are limited to concrete penetration. The FE programs that have been used in the thesis are Abaqus/Explicit; see Abaqus/Explicit (2001) and AUTODYN; see AUTODYN (2001). These are discussed in greater detail in sections 5.3 and 5.4. Comparisons with experimental results and analyses of a projectile impacting a concrete target are discussed in Chapter 6.

5.2 Lagrangian, Eulerian and SPH techniques

In FE codes there are two main descriptions for the material movement, i.e. the Lagrangian and Eulerian descriptions as shown in Figure 5.1. In the Lagrangian description, the numerical mesh distorts with the material movement. In the Eulerian description, the numerical mesh is fixed in space, and the material moves in the elements. To allow the material movement, the fixed numerical mesh is larger than the original body.

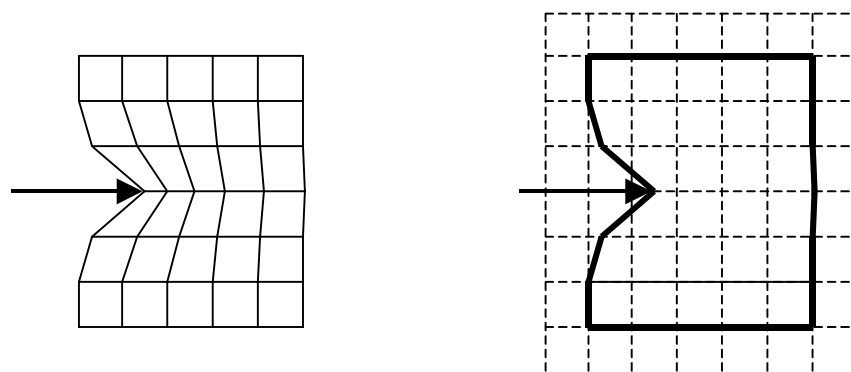


Figure 5.1 The Lagrangian description (left) and the Eulerian description (right).

With large displacements, by using the Lagrangian description of the material movement, numerical problems arise due to distortion and grid tangling of the mesh. This leads to loss of accuracy and can yield small time steps or even terminate the calculation. To overcome the numerical problems, a rezoning or erosion algorithm can be used. Rezoning transforms the current numerical mesh onto a new numerical mesh. With great distortion or grid tangling, an erosion algorithm must be used to continue the calculation. Erosion is defined as removal of elements in the analysis when a predefined criterion is reached; normally this criterion is taken to be the plastic

strains. With the erosion algorithm, a non-physical solution is obtained because of mass and thus internal strain energy is removed from the system.

Both the Lagrangian and Eulerian techniques are grid-based methods. The Smooth Particle Hydrodynamics (SPH) technique is a grid less technique, which is relatively new and has problems such as stability and consistency. Advances are that the numerical problems with grid tangling are overcome, since the technique is grid less, and modelling of fracture can be done in a more realistic way. Kernel approximation is used in the SPH technique; the body is created with interpolation points which are randomly distributed; see Figure 5.2. Each point will be influenced from points close to its neighbourhood, which are at some predefined distance. For example, to calculate the density of point I in Figure 5.2, the marked area will influence the density for that point with different weights, depending on the distance from that point – the weighting function. The SPH technique has not been used in this thesis, and thus is not discussed further.

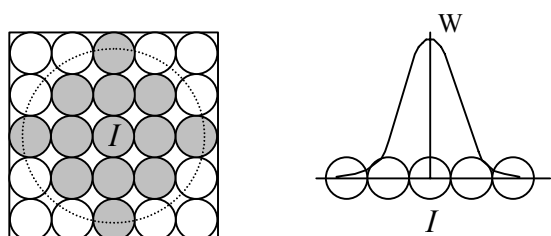


Figure 5.2 Principle of the Kernel approximation, based on Clegg et al. (1997). To the left: particle neighbourhood. To the right: weighting function.

5.3 Abaqus/Explicit

For non-linear analyses in Abaqus/Explicit there is no unique material models for both compression and tension. Which model is chosen depends on the type of analysis. For example if cracking is studied (where the compressive stresses is in the elastic zone) the *brittle cracking* model is used. In the case of compressive failure, the *elastic-plastic* model is used. The input in the *elastic-plastic* model is the uniaxial stress–strain relationship obtained from uniaxial tests as shown in Figure 5.3.

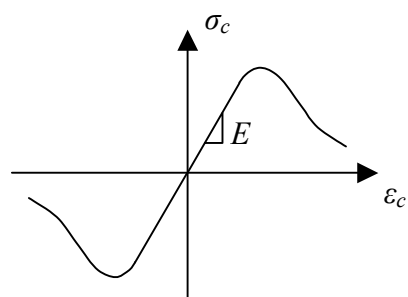


Figure 5.3 Elastic-plastic model for concrete in compression.

The *brittle cracking* model is used for concrete in tension, as shown in Figure 5.4. The model is linear–elastic in compression; for tension the softening is described as a bilinear stress–strain relationship. Here a model proposed by Gylltoft (1983) is used, which is based on the stress–crack opening relationship. To calculate the maximum crack width w_u , the fracture energy G_F and the tensile strength f_t of concrete are used. The crack width is smeared out to a distance, l , as shown in equation (5.1). In two-dimensional models for un-reinforced concrete, this distance is normally approximated by the square root of the area of the element, Johansson (2000).

$$\varepsilon_u = \frac{w_u}{l} = \frac{4G_F}{f_t l} \quad (5.1)$$

For crack initiation, Rankine’s criterion is used, i.e. the crack is initiated when the maximum principal stress reaches the concrete tensile strength.

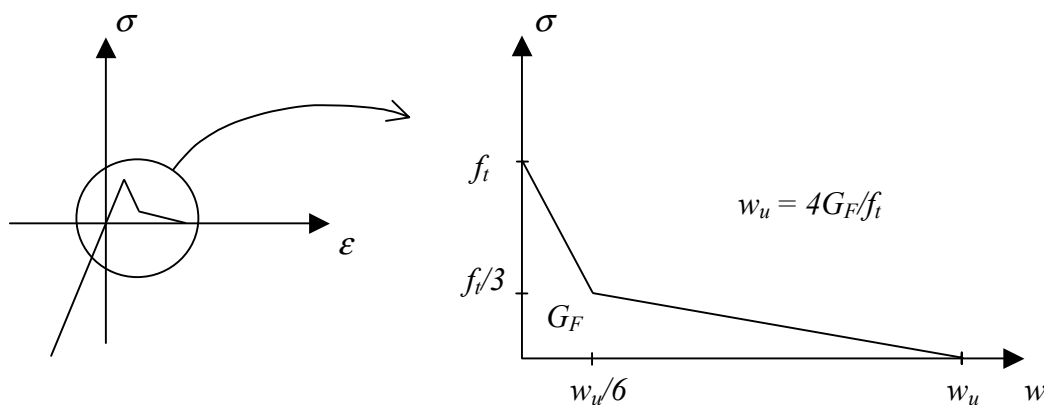


Figure 5.4 Bilinear uniaxial stress–strain relationship for concrete in tension, based on the stress–crack opening relationship; based on Gylltoft (1983).

The strain rate dependency with the elastic-plastic model can be entered directly as a tabular function of the equivalent plastic strain rate. The rate dependency is the dynamic increase factor (*DIF*), i.e. the relation of dynamic strength to static strength as a function of strain rate.

For the brittle *cracking model*, the rate dependency cannot be taken into account.

For the steel, a perfect elastic-plastic model with the von Mises yield criterion is used.

5.4 AUTODYN

In AUTODYN – AUTODYN (2001) – there are Lagrangian, Eulerian and SPH techniques for describing the material movement. In this thesis two types of techniques have been used, the Lagrangian and Euler techniques. As described in section 5.2, in Lagrangian mesh the material is remaining in the elements (cells), and in Eulerian mesh the material is transported between the elements. With ALE (Arbitrary Lagrange Euler), the Eulerian and Lagrangian techniques are combined.

The governing equations in AUTODYN are the Rankine-Hugoniot equations, conservation of mass, momentum and energy; see equations (2.15), (2.16) and (2.17) in Chapter 2. To complete the description of the continuum, two further relations describing the material behaviour are required (besides the load and boundary conditions): first the equation of state (EOS), and secondly a constitutive model.

5.4.1 Equation of state

The equation of state (EOS) relates the pressure to the local density (or specific volume) and the local specific internal energy in the material, with the general form of

$$p = p(\rho, e) \quad (5.2)$$

Where ρ is density and e is specific internal energy.

In FE programs used for static analysis, a constitutive model without any explicit description of the EOS normally describes the material behaviour. For these programs at high hydrostatic pressures (all principal stress components are equal), the material behaviour is linear (if the model has no cap combined with the original yield surface).

For severe loading, e.g. explosion or penetration into concrete, the hydrostatic pressures levels are so high that the non-linearity of the material behaviour must be taken into account.

5.4.1.1 Concrete

When concrete is applied to hydrostatic pressure, the relationship between hydrostatic pressure and density becomes non-linear at a certain pressure level as shown in Figure 5.5. Initially, for low-pressure levels the relationship for pressure and density is linear (elastic loading). With further loading, micro cracking occurs in concrete. Since concrete is porous, the pores collapse and the material will be compacted; this is termed as the plastic compaction phase.

At very high pressure levels, when the concrete is fully compacted (all pores are collapsed), the relationship between pressure and density becomes linear again. The EOS used in analyses in Chapter 6 is a combined P-Alpha and a polynomial EOS (implemented in the RHT model: see section 5.4.2.1). The P-Alpha EOS (in P-Alpha the plastic compaction phase is ten-point piecewise linear; P stands for pressure, and

Alpha is defined as the current porosity) defines the starting point for plastic compaction, and the polynomial EOS defines the compaction phase. In Figure 5.5 the initial density, ρ_0 , is the undisturbed concrete density, and the solid density, ρ_s , is defined as the density at zero pressure of the fully compacted solid. The material behaves elastically until the initial compaction pressure, p_{crush} , is reached; thereafter the plastic compaction phase takes place.

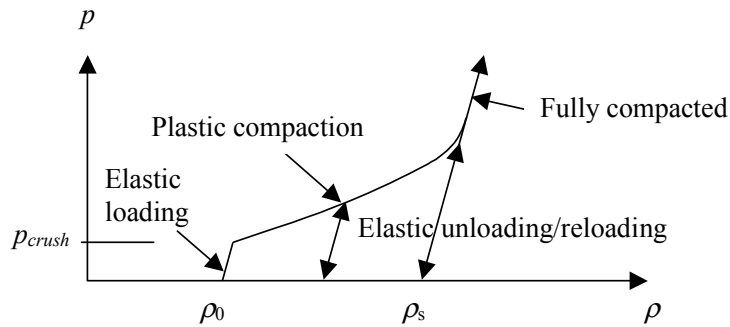


Figure 5.5 Equation of state (EOS), combined P-Alpha and polynomial.

5.4.1.2 Steel

For hydrostatic pressure, steel compression is approximately proportional to the pressure level. Thus, a linear EOS for steel is used. The pressure level is dependent on the bulk modulus, K , and the compression, μ ($\rho =$ density), as shown in Figure 5.6.

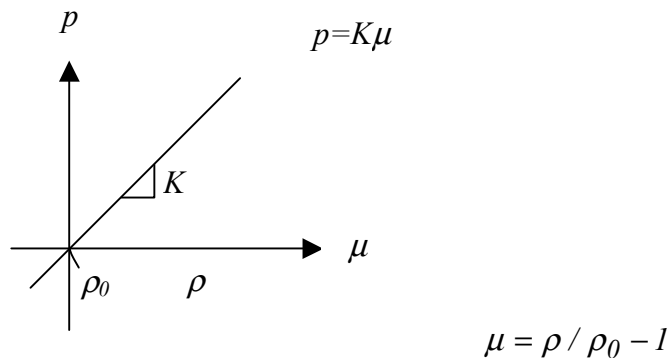


Figure 5.6 Equation of state for steel.

5.4.2 Constitutive models

The constitutive model relates the stress to the strains (ϵ), strain rates ($\dot{\epsilon}$), internal energy (e) and damage (D), with the general form.

$$\sigma_{ij} = f(\epsilon_{ij}, \dot{\epsilon}_{ij}, e, D) \quad (5.3)$$

5.4.2.1 Concrete

The constitutive model used in analyses in this thesis with AUTODYN is the RHT model, developed by Riedel (2000); see Figure 5.7. The model includes pressure hardening, strain hardening, strain rate hardening, third-invariant dependence for compressive and tensile meridians, and a damage model for model strain softening.

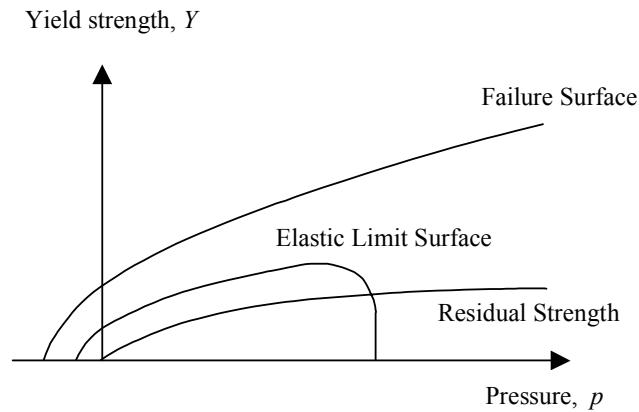


Figure 5.7 RHT-model.

The model consists of three pressure-dependent surfaces: a failure surface, an elastic limit surface, and a surface for residual strength.

The failure surface is a function of pressure and strain rate. The third-invariant dependence is included in the failure surface; see AUTODYN (2001), which defines the transfusion from the compressive meridian to tensile meridian and stress states between these. In equation (5.4) the normalized failure surface (the compressive meridian) is shown for static loading:

$$Y_{comp}^* = A(p^* - p_{spall}^*)^N \quad (5.4)$$

where A and N define the form of the compressive meridian that is a function of pressure, p^* is the normalized pressure by f_c and p_{spall}^* is defined as $p^*(f_t/f_c)$.

The residual strength is defined by the parameters B and M , and is a function of the pressure level as shown in equation (5.5).

$$Y_{res}^* = B \times p^{*M} \quad (5.5)$$

5.4.2.2 Steel

In this thesis, for steel a perfect (non-hardening) von Mises strength model is used as shown in Figure 5.8. The yield surface can be calculated from the second invariant of the stresses.

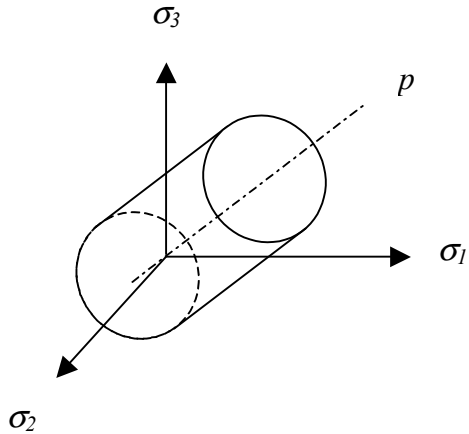


Figure 5.8 von Mises strength model.

5.5 Treatment of blast, shock and stress waves

Traditionally, for a concrete wall subjected to a blast wave, the load is applied to the surface as a time-dependent boundary load, where the pressure is often simplified with a triangular pressure-time curve according to equation (5.6); see also section 2.2.1.

$$p(t) = p_+ \left(1 - \frac{t}{t_+}\right) \quad (5.6)$$

With new advanced FE techniques, it is possible to follow the analysis from the explosion to creation of a blast wave and its propagation against the target, although, with a high computational time. In AUTODYN, time can be saved with a re-mapping technique, which allows the solution from an analysis to be taken to second analysis. By using a 1D model of the explosion and the blast wave propagation, it can be mapped to a 2D or 3D model as an initial load. This method gives more accurate prediction of the blast wave than using the traditional method with time-dependent boundary load as described in equation (5.6).

5.6 Erosion models

With non-linear FE programs it is possible to simulate penetration in concrete by fragments or projectiles. When a fragment or projectile penetrates concrete, the elements in the FE model will have large movements. With large displacement, in a Lagrangian description of the material, the numerical mesh may become highly distorted, leading to an inaccurate and inefficient solution. Further, this may ultimately lead to a termination of the calculation. To overcome the problem of distortion and grid tangling, an erosion algorithm can or must be used, implying an erosion model.

With an Eulerian description of the material movement, the problems of distortion and grid tangling are overcome, and hence no erosion algorithm is needed, implying a non-erosion model.

To get realistic solutions, the criterion for erosion (the plastic strain), is normally set above 150 % (natural strain). A parameter study by Johnson *et al.* (1998), where a concrete target was penetrated by a steel projectile, concludes that erosion criteria above 300 % will give realistic results. In the study, erosion criteria of 200, 300 and 400 % were used. The results for radial stresses and depth of penetration, as well as the mesh dependency, were compared. The study concluded that the higher the criterion for erosion is, the more accurate the results will be. However, the results regarding the general response were similar between the criteria of 300 and 400 %. The study also showed that with an erosion criterion of 200 %, the depth of penetration falls in the range of the test data, but the radial stresses become jumpy.

If the erosion criterion is set too low, the behaviour of the system will be inaccurate. For instance, the stress wave propagation and confined effects will be reduced since the strain energy cannot be transmitted.

Erosion criteria that are available in AUTODYN are the geometric strain, incremental geometric strain or effective plastic strain.

In Abaqus/Explicit the criteria for erosion is taken to be the plastic strains for the *elastic-plastic* model; see section 5.3.1.1. In the *brittle cracking* model – see section 5.3.1.1 – the erosion criterion is set to the direct cracking failure strain; the options are to have an erosion criterion for one, two or three cracks. One crack indicates that an element will be removed when any local direct cracking strain component reaches the failure value. Alternatively, two or three cracks indicate that the element will be removed when two or three cracking strains, respectively, reach the failure value.

5.7 Parameter study

Here a parameter study with AUTODYN is carried out for a steel projectile impacting a concrete target. In a study with Abaqus/Explicit; see Leppänen (2001), a parameter study was performed. The study concluded that the residual strength and the criteria for erosion influence the depth of penetration. By increasing the residual strength and the criteria for erosion, the depth of penetration is decreased. A trustworthy model must capture both the crater size and the depth of penetration, which are used for comparison in the present parameter study.

To sum up, the parameters of the target that influence the depth of penetration and the crater size are shown in Table 5.1, with values of large or small influence on the results. The parameters that will influence the response of the concrete are: the compressive strength, the tensile strength, the fracture energy, and the strain rate dependency for both compression and tension. The size of meshing, and with the Lagrangian method the criteria of erosion, will also influence the results.

Table 5.1 Parameters that influence the depth of penetration and crater size of the concrete target.

Parameter	Influence to the depth of penetration	Influence to crater size of the concrete target
Compressive strength	large	small
Tensile strength	small	large
Fracture energy	small	large
Strain rate dependency for compression	large	small
Strain rate dependency for tension	small	large
Residual strength	large	small
Erosion criteria	large	small
Mesh dependency	large	small

As listed in Table 5.1, the important parameters that influence the depth of penetration are the compressive strength, the strain rate dependency for compression, the level of the residual strength, the erosion criteria (with Lagrangian method) and the mesh dependency. The first three are well known from experimental results but, as far as the author is aware, the results in the literature are at low strain rates in the case of the strain rate dependency for compression, while the results on residual strength are for static and not dynamic loading. Furthermore, the depth of penetration is mesh-dependent.

The parameters that influence the crater size are the tensile strength, the fracture energy, and the strain rate dependency for tension. These are well known from literature, but in the last case only for uniaxial loading. For multiaxial loading at high strain rates, no experimental results have been reported to the author's knowledge.

Other factors that influence the depth of penetration and the crater size are the geometry of the target and the properties of the projectile. For example, the crater size will increase with increasing projectile diameter. In this comparison, a 6.28 kg projectile, with a diameter of 75 mm, impacted a concrete cylinder with diameter of 1.6 m and length of 2.0 m at striking velocity of 485 m/s.

A more detailed parameter study has been performed with the Lagrangian method, according to the parameters of mesh dependency, residual strength and the criteria for erosion. In addition, a phenomenological study of the strain rate dependency for tension has been carried out.

5.7.1 Mesh dependency

It is well known that the size of the numerical mesh affects the results and that with a refined mesh the computational time increases dramatically. For dynamic loading, the mesh dependency is even more important since more terms are added to the constitutive models (the strain rate effect). Johansson (2000) studied the mesh dependency by comparison of static and dynamic loading. He concluded that if the strain rate effect was included in the constitutive model, the general behaviour changed considerably. The strain rate was dependent on the numerical mesh, and therefore also the increase in dynamic strength is mesh-dependent. Solutions can be totally invalidated by poor choice of mesh. However, there is a risk of having too fine a mesh – see Wiberg (1974) – due to discretization and manipulation. Discretization error is dependent on the numerical modelling, and with an increasing number of elements the error is reduced. On the other hand, the manipulation error increases with the number of elements. Manipulation error is due to truncation, round-offs, and wrong input (too few numbers).

To treat the mesh dependency, the common method is to halve the mesh and compare the first coarse mesh with the halved finer mesh, and if the results differ negligibly the analyst is satisfied. In FE analyses with dynamic loading, it is important to use several meshes to ensure the accuracy of the results. Moreover, changing a mesh size in the structure must be done with great care.

In FE analyses in Abaqus/Explicit, the effects of meshing have been compared; see Figure 5.9. In these analyses the criterion for erosion is taken to be 200 % equivalent plastic strain. In Figure 5.9, the fifth mesh has converged according to the depth of penetration, by refining the mesh; the result as regard the depth of penetration will hardly be affected. This is, in principle, treatment of mesh dependency for impact loading.

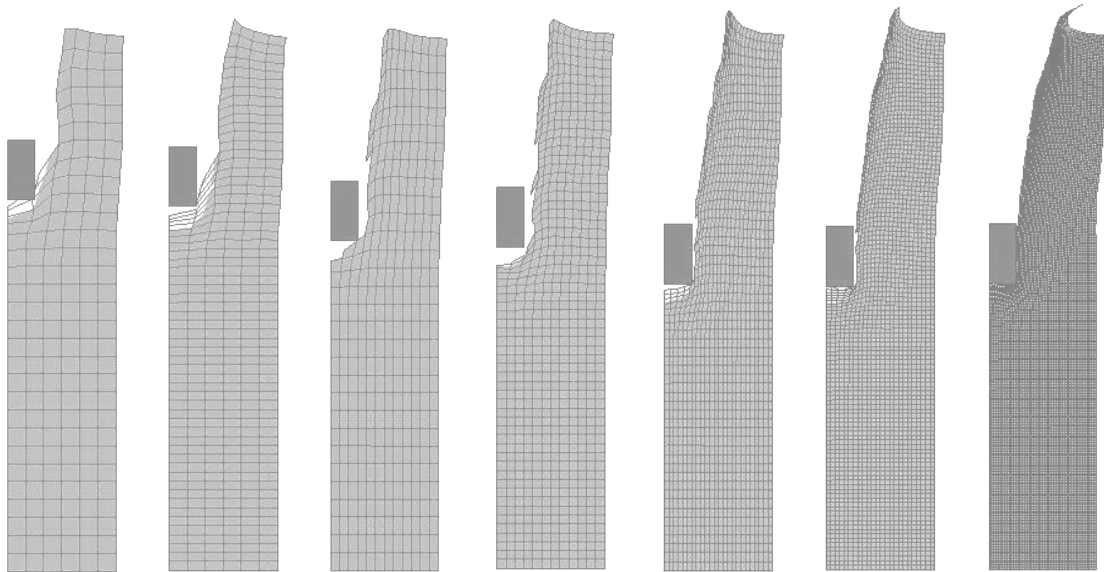


Figure 5.9 Effects of meshing in Abaqus/Explicit.

Zukas and Scheffler (2000) made a study on the effects of meshing. They concluded that, for accuracy, there should be at least three elements across the radius of the projectile. With AUTODYN, the mesh dependency was carried out with comparison of a projectile impacting a concrete target, as shown in Figure 5.10. By starting with the thumb rule having three elements across the radius of the projectile, the mesh has been further refined. The mesh sizes and number of elements are shown in Table 5.2.

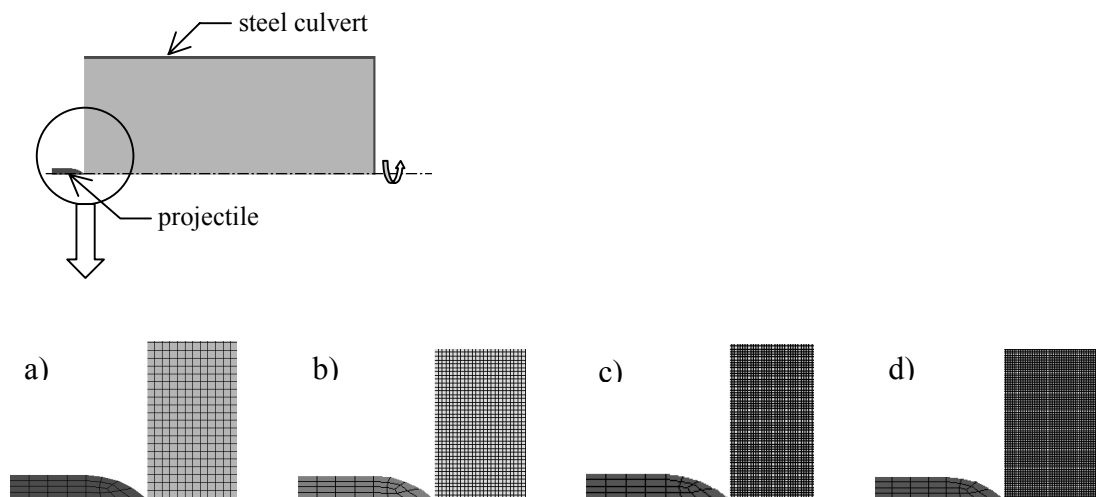


Figure 5.10 Mesh dependency in AUTODYN, four numerical meshes; the size and number of elements are shown in Table 5.1.

Table 5.2 Mesh dependency, size and number of elements for the target. Target radius is 800 mm and length is 2000 mm. Projectile radius is 37.5 mm.

Mesh	Size of element [mm]	Number of elements
a)	12.5	64 x 160
b)	6.25	128 x 320
c)	4.17	192 x 480
d)	3.13	256 x 640

In dynamic loading the strain rate is dependent on the numerical mesh. Here two comparisons have been performed.

First, the strain rate dependency for tensile strength is overestimated (with $\delta = 0.11$; see section 5.7.4), and the criterion for erosion (instantaneous geometric strain) is taken to be 70 %. Secondly, the parameters of strain rate dependency for both tension and compression are chosen with realistic values.

For the first comparison, as seen in Figure 5.11 the second mesh has converged according to the depth of penetration. The depth will hardly be affected by further refining of the mesh. The difference between the coarse mesh “a” and the fine mesh “c” is approximately 6 % according to the depth of penetration, and respectively less than 1 % between the medium mesh “b” and the fine mesh “c”.

By further refining of the numerical mesh “d”, the depth of penetration surprisingly decreases again.

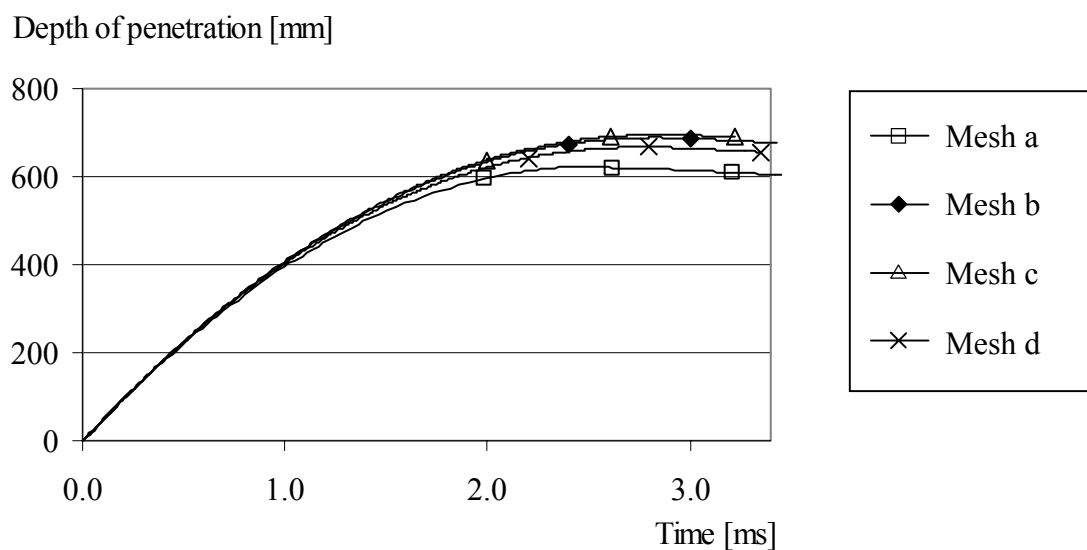


Figure 5.11 Effects of meshing on depth of penetration, AUTODYN.

A comparison of the crater size for the four meshes shows that they are approximately the same size, as shown in Figure 5.12.

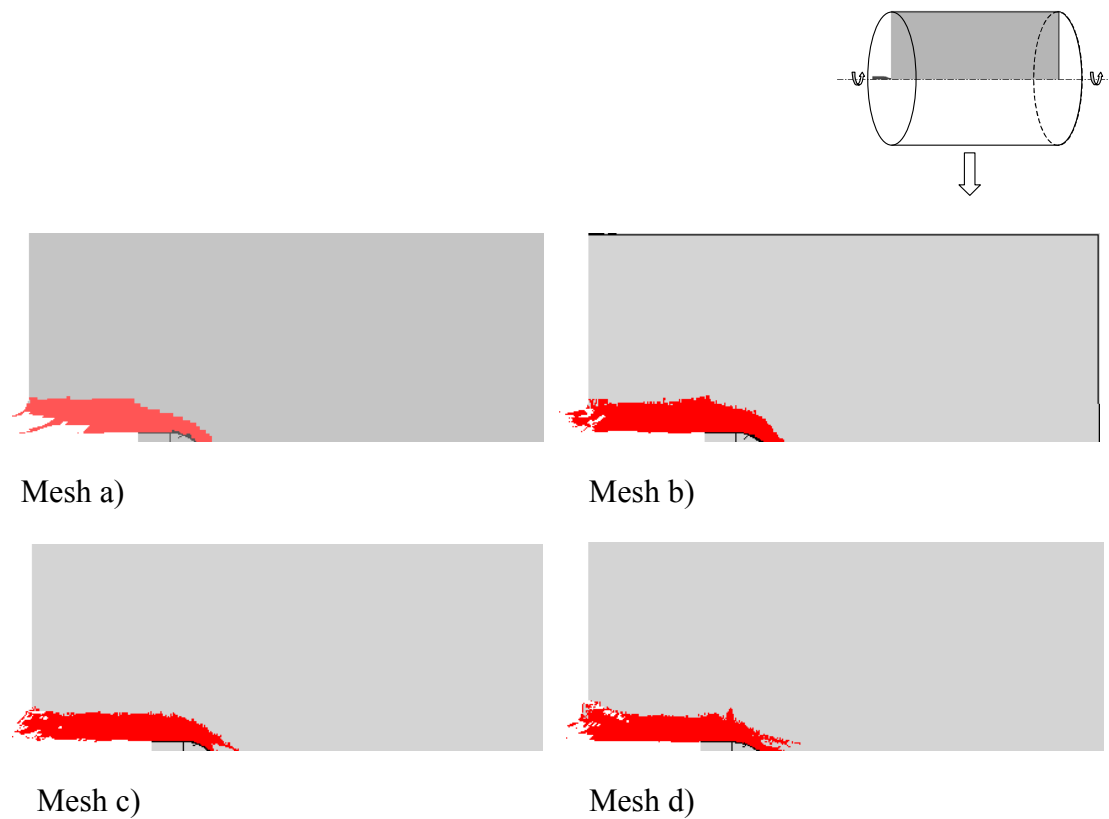


Figure 5.12 Effects of meshing on crater size, AUTODYN.

For the second comparison, with a realistic description of the material parameters, and with an erosion criterion of 125 % (instantaneous geometric strain), the depth of penetration will not converge as in the first comparison by refining the mesh; see Figure 5.13. The depths of penetration of the coarse mesh “a” and medium mesh “b” are approximately the same. The difference between the medium mesh and the fine mesh “c” is 6 %. By refining the mesh, the depth of penetration will increase.

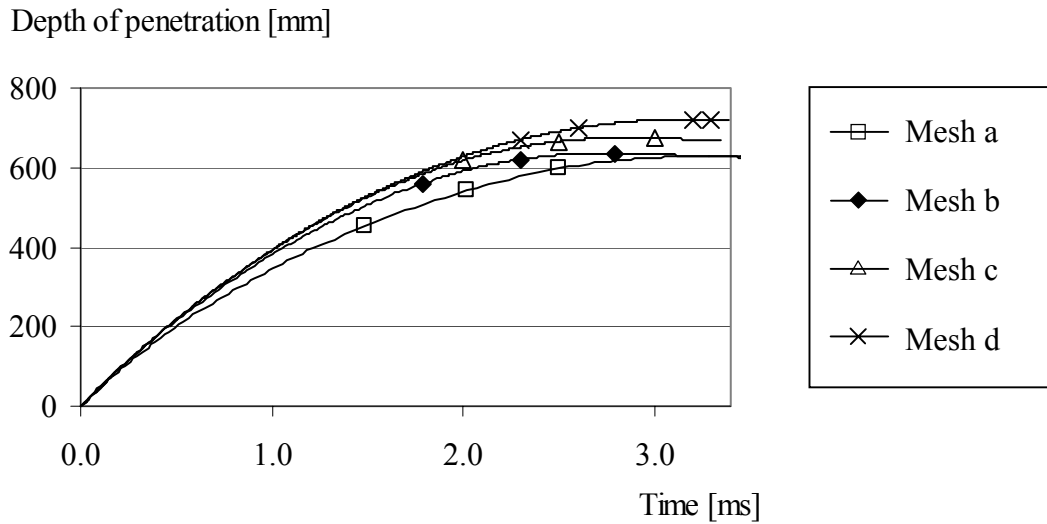


Figure 5.13 Parameter study, mesh dependency, depth of penetration.

It is therefore obvious that the results are mesh-dependent, and it is important to notice that the mesh affects the strain rate in the material, and, thus the strength and behaviour of the material. When comparing the crack propagation (the damage) by refining the mesh, the number of fine cracks will increase as shown in Figure 5.14.

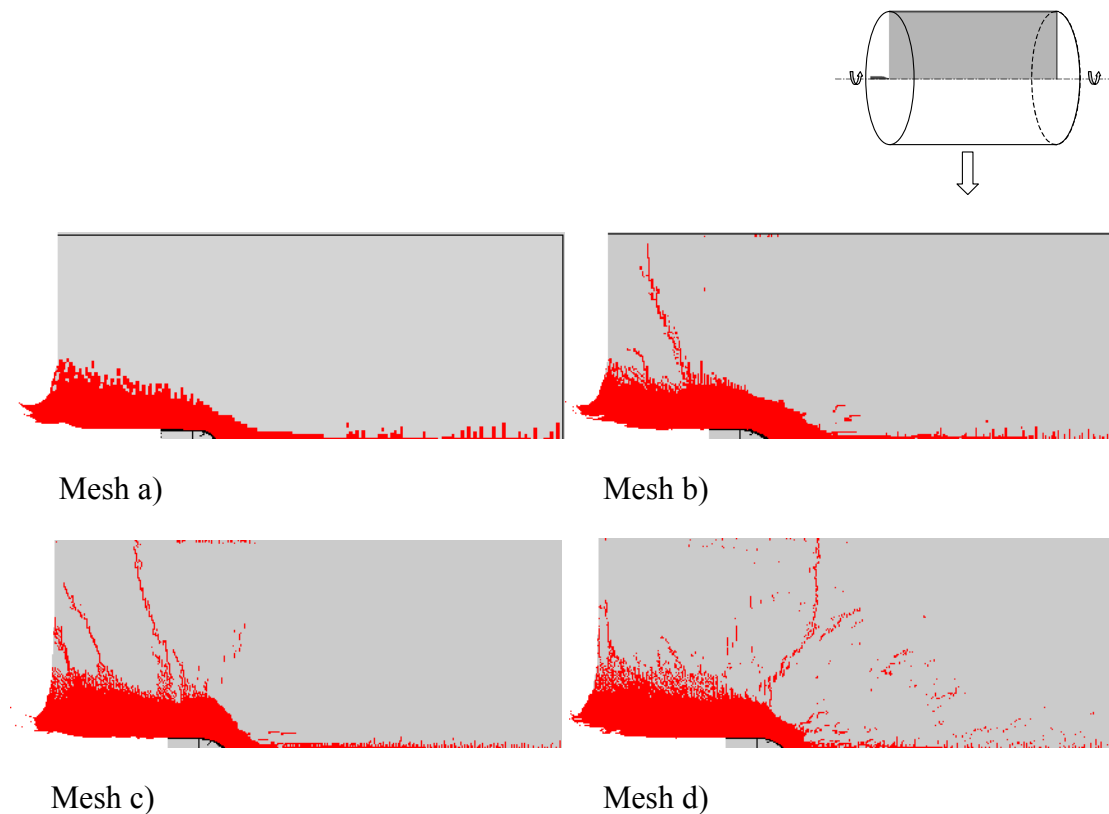


Figure 5.14 Parameter study, mesh dependency of crater size.

5.7.2 Residual strength

When a fragment or projectile impacts concrete, it will penetrate the concrete. The concrete will be crushed and the strength of the crushed concrete is the residual strength. In the uniaxial stress state, the residual strength is always zero. However, in multiaxial stress states as in real structures, the crushed concrete will contribute to the resistance. During the penetration, the crushed concrete will be pushed in both longitudinal and lateral directions, with confining effects.

In AUTODYN the level of the residual strength is estimated by parameters B and N ; see section 5.4.2.1. Here a comparison of residual strengths is made with the parameter B equal to 0.9, 1.1 and 1.5, and N equal to 0.7. The corresponding yield surface and the uniaxial stress–strain relationship for confined concrete are shown in Figure 5.15 and Figure 5.16 respectively (for B equal to 0.9 and 1.5).

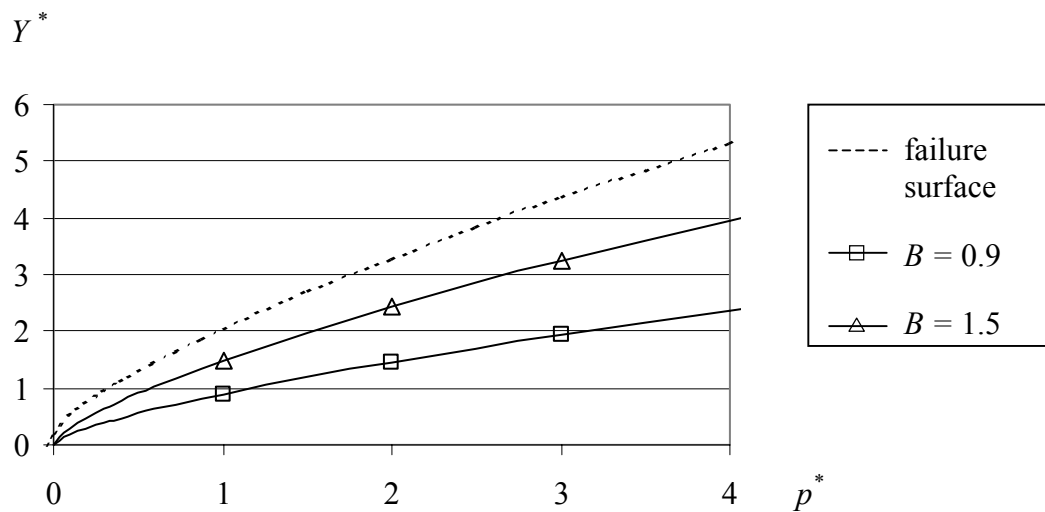


Figure 5.15 Residual yield surface.

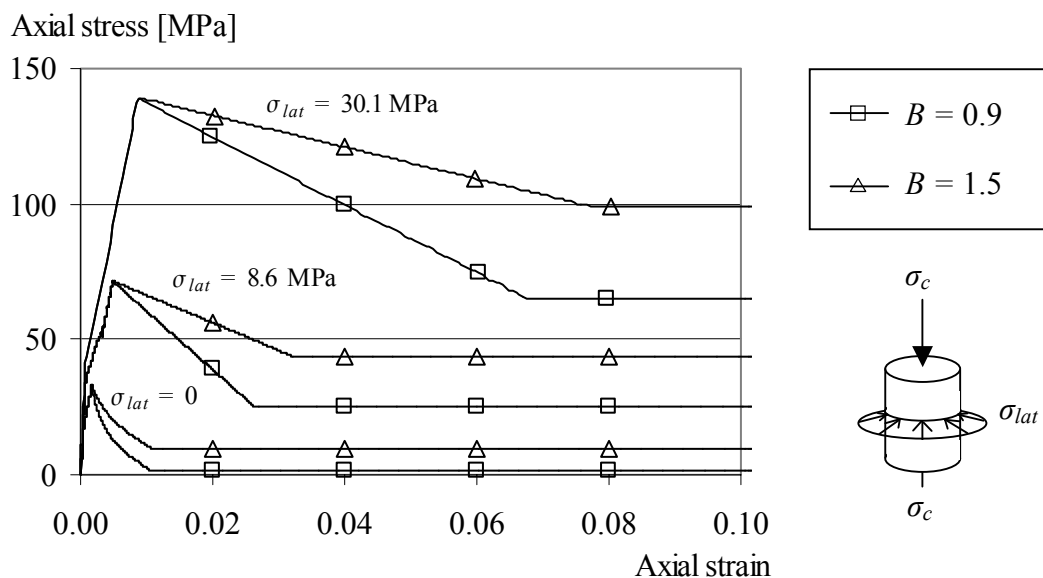


Figure 5.16 Stress–strain relationship for confined concrete.

The area under the stress–strain curve is a measurement of the energy absorption of the concrete. The combination of high residual strength and high erosion criterion, will lead to more energy absorption than a lower residual strength with lower erosion criteria. This is shown uni–axially schematic form by Figure 5.17. Here, for the comparison with varying residual strength, the criterion for erosion (the instantaneous geometric strain) is taken to be 125 %.

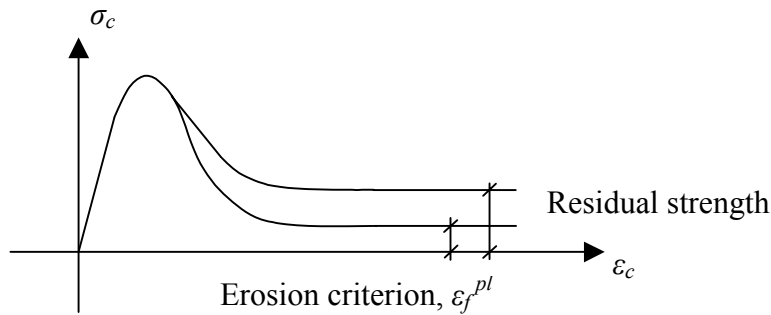


Figure 5.17 Energy absorption capacity according to residual strength and erosion criterion.

By increasing the level of the residual strength, the concrete energy absorption is increased, and the depth of penetration is influenced as shown in Figure 5.18. However, the crater size is hardly affected by the level of the residual strength, as shown in Figure 5.19.

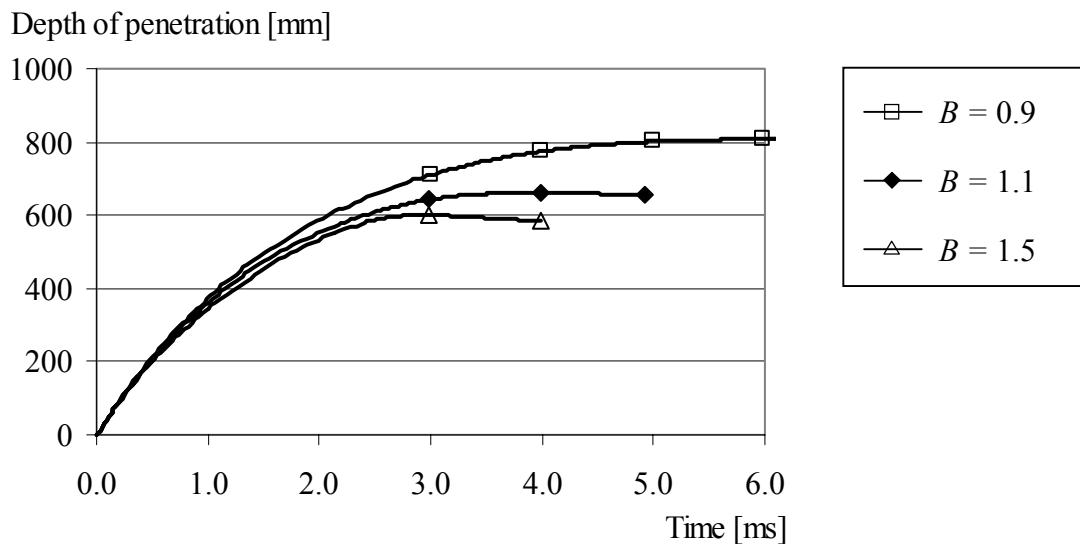


Figure 5.18 Parameter study, residual strength and depth of penetration.

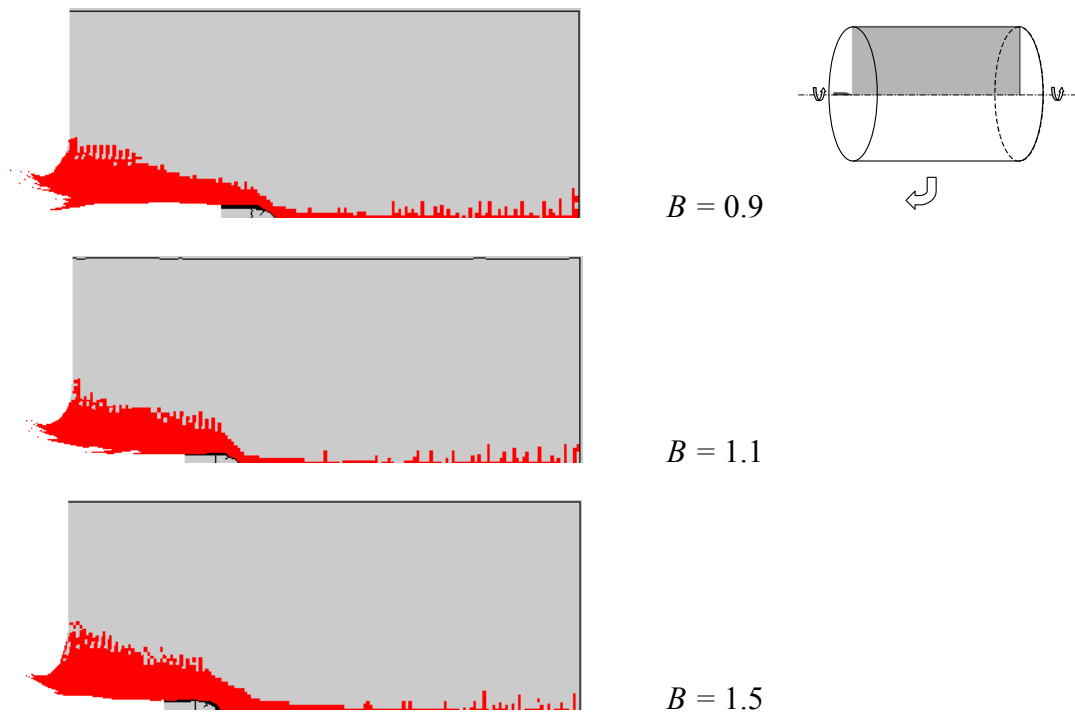


Figure 5.19 Parameter study, residual strength and crater size.

5.7.3 Erosion criteria

When studying fragment or projectile penetration into concrete, the Lagrangian method requires use of an erosion algorithm as described in section 5.6.1. The criteria for erosion will strongly influence the depth of penetration, as shown in Figure 5.20. The maximum crater diameter is barely affected by the level of the erosion criterion as shown in Figure 5.21.

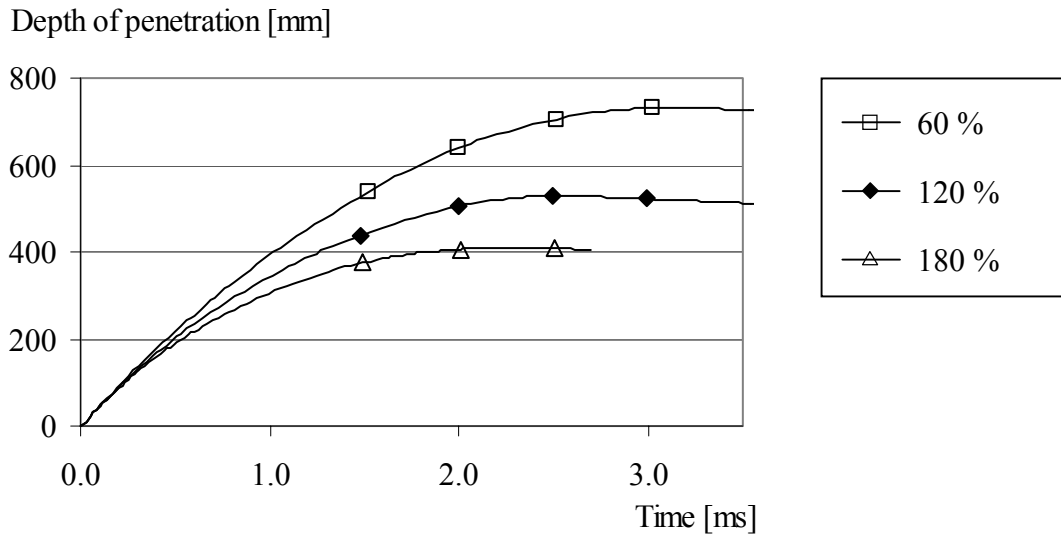


Figure 5.20 Parameter study, erosion criteria and depth of penetration.

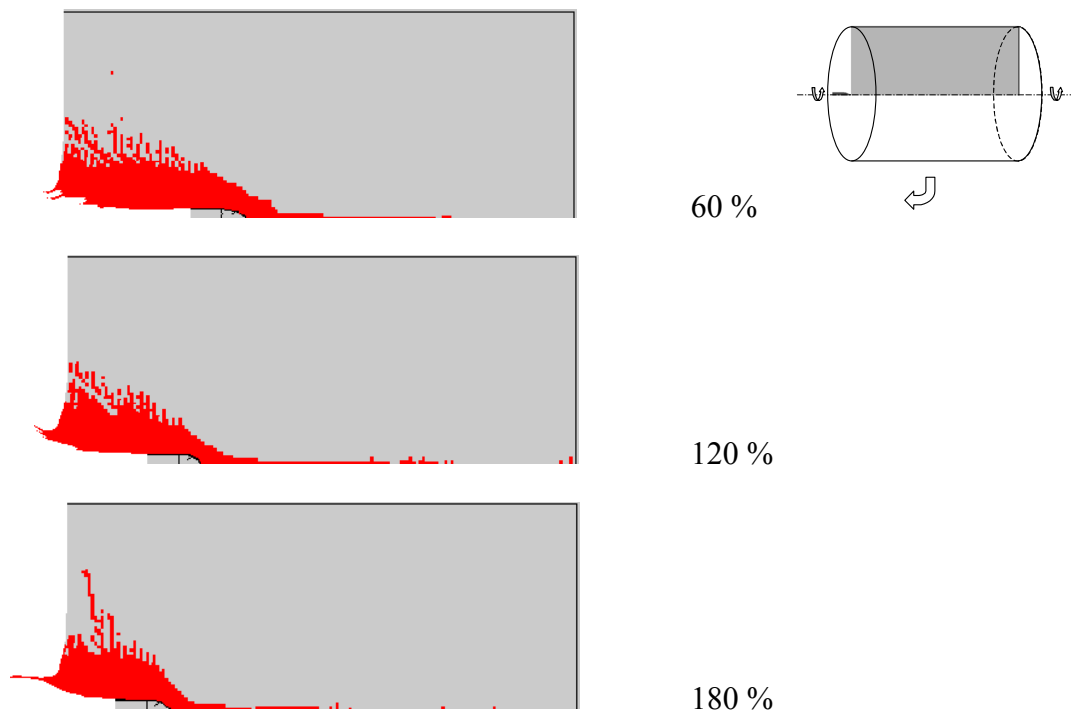


Figure 5.21 Parameter study, erosion criteria and crater size.

5.7.4 Strain rate effect of tensile strength

Concrete subjected to impact loading will have an increased strength, in both tension and compression – the strain rate effect. The increase in tension is as important as the increase in compression. During the penetration by the projectile, the concrete will be compressed in both the longitudinal and radial directions. Due to the compression in the radial direction, a tensile ring will be created around the projectile.

In the RHT model, the increase in tensile strength due to the strain rate effect is calculated as an increase in the yield surface by a factor F_{RATE} . The increase is dependent on the strain rate of the material and a factor δ ; see further AUTODYN (2001).

$$F_{RATE} = \left(\frac{\dot{\epsilon}}{\dot{\epsilon}_0} \right)^\delta$$

where $\dot{\epsilon}_0$ refers to static loading.

A phenomenological study of the influence of the tensile strain rate dependency shows that, with increasing strength, the crater size is reduced, as shown in Figure 5.22. In addition, the depth of penetration is influenced by the tensile strength as shown in Figure 5.23. Therefore, modelling the increase in tensile strength is as important as modelling the increase in compressive strength.

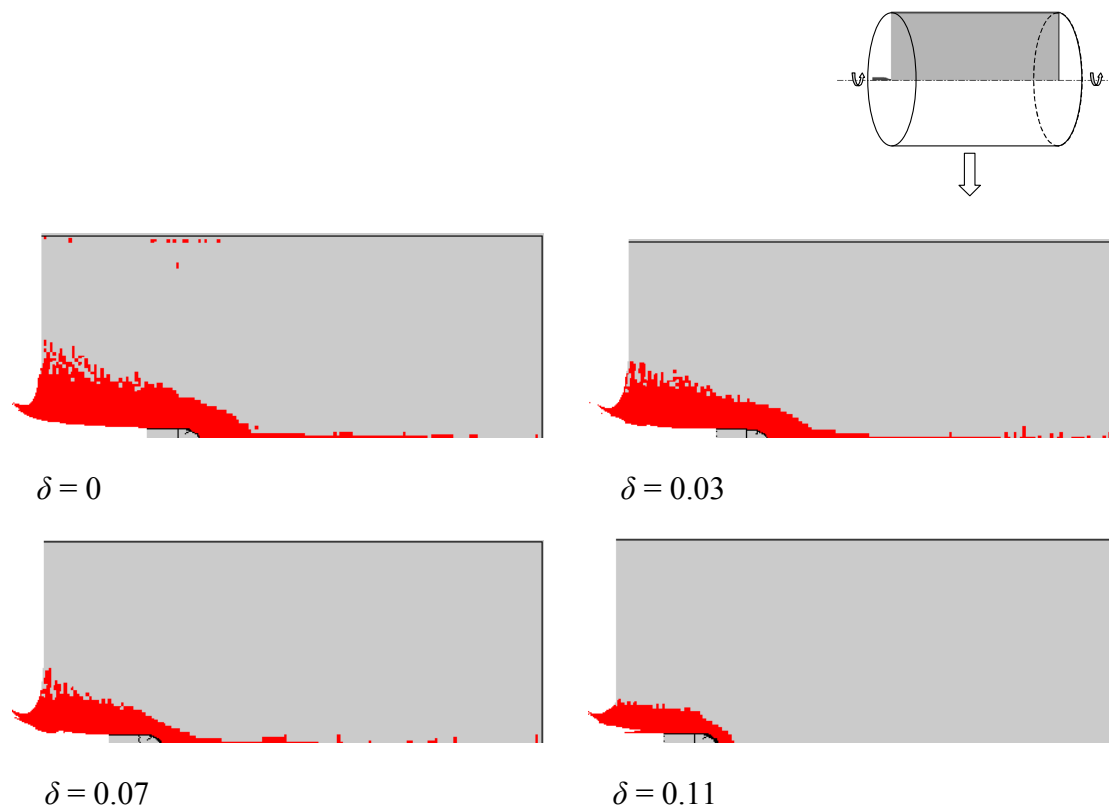


Figure 5.22 Phenomenological study of the effect of tensile strength on crater size.

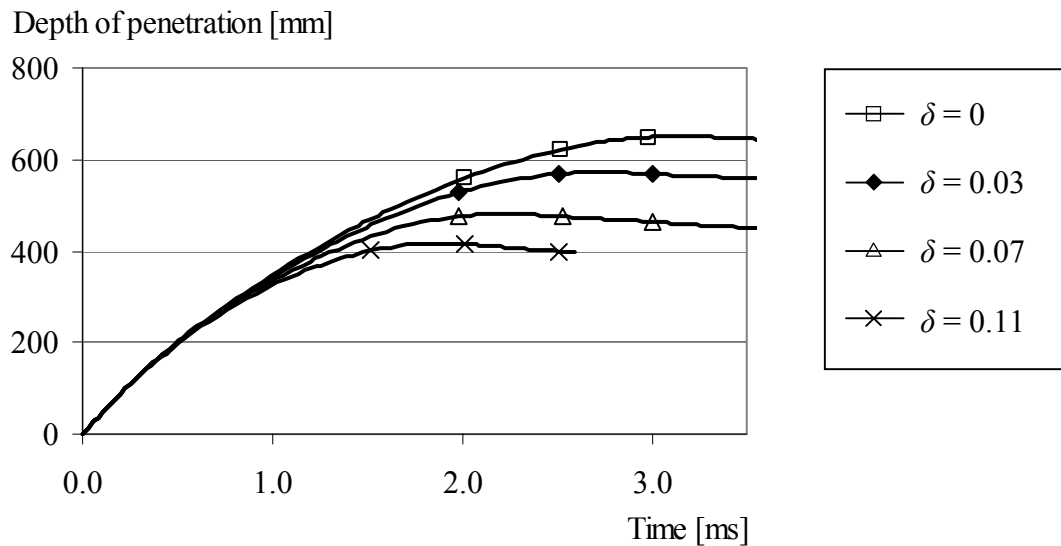


Figure 5.23 Phenomenological study of the effect of tensile strength on depth of penetration.

5.8 Discussion

The complexity of the mesh dependency can be solved by numerical methods, such as non-local models; see Needleman (1988). However, by using the traditional method of refining the mesh, reasonable results can still be obtained.

The residual strength has been studied by Attard and Setunge (1996). A model was developed for determining the full stress–strain curve from standard tri-axial tests, including the residual strength. The confining pressure varied between 1 and 20 MPa. In the severe loading case, as in concrete penetration, the confining pressure will exceed the range of that study. However, the model proposed by Attard and Setunge will indicate the level of the residual strength, and is used to calculate the residual strength in this thesis. Furthermore, the yield surface of the residual strength will approach the failure surface at high pressures; see Imran and Pantazopoulou (2001). This is captured with the model proposed by Attard and Setunge as well.

As noted above, with the Lagrangian method an erosion algorithm must be used to avoid numerical problems. By removing elements during the analyses, mass and strain energy are removed from the system, and non-physical results are obtained. The Eulerian method is preferable since no erosion algorithm is needed. However, it increases the computational time and for rapid initial estimation the Lagrangian method is preferable.

6 FE analyses of concrete penetration

A FE model with good material models should be able to predict the crater size and the depth of penetration of a steel projectile impacting a concrete target. In this chapter, FE analyses have been compared to experimental results. To ensure that the model can predict the depth of penetration and crater size, results from more than one experiment must be reproduced. In this thesis two experimental series with a total of 6 shots have been compared.

In a study by Leppänen (2001), FE program Abaqus/Explicit was evaluated, which is summarized in section 6.2. Furthermore, analyses with AUTODYN by using the RHT model for the concrete target have been carried out, as described in section 6.3. Two experimental series have been compared with FE analyses: first, with a 6.28 kg projectile impacting a concrete cylinder, by Hansson (1998), and secondly with a 0.906 kg projectile impacting a concrete cylinder, by Forrestal *et al.* (1994). The first series both the Lagrangian and Eulerian methods, and the second series the Lagrangian method have been used for the non-linear FE analyses.

6.1 Experimental series

In the first of these series, the 6.28 kg steel projectile impacted a concrete cylinder with a striking velocity of 485 m/s. Two shots are compared, one with support and the other without any support at the backside of the target. In the second series, with a projectile mass of 0.906 kg, the results of several striking velocities from 277 m/s to 800 m/s are compared with FE analyses.

6.1.1 Heavy steel projectile

In the experimental series reported by Hansson (1998), a 6.28 kg steel projectile was used with a length of 225 mm, diameter of 75 mm, density of 7830 kg/m³, bulk modulus of 159 GPa, shear modulus of 81.8 GPa, and yield stress of 792 MPa.

The target was a concrete cylinder cast in a steel culvert with a diameter of 1.6 m and a length of 2 m. The concrete cube strength was approximately 40 MPa (tested on a 150 mm cube). Two shots were made with the same impact velocity, first with support and secondly without support at the backside of the target; the results are shown in Table 6.1.

Table 6.1 Data summary for the experiments with 6.28 projectile impacting a concrete cylinder.

Striking velocity [m/s]	Projectile mass [kg]	$f_{c,cube}$ [MPa]	Depth of penetration [m]
485	6.28	40	0.655-0.660*

* Two shots were made, first with support and second without support at the backside of the target.

6.1.2 Light steel projectile

In the series reported by Forrestal *et al.* (1994), projectiles made from 4,340 steel rods and heat-treated to a hardness of R_c 43-45 were used. Moreover, filler material was used in the projectiles, with a density of 1580 kg/m^3 . The projectile length, l , was 242.4 mm; its diameter d was 26.9 mm, and the ogival radius s was 53.8 mm.

The concrete targets were cast in galvanized, corrugated steel culverts with diameter of 1.37 m and target length of 0.76 m. The shots had striking velocities of 277 m/s and 499 m/s. For two other experiments with impact velocities of 642 and 800 m/s, the target diameter was 1.22 m and the length 1.83 m. The concrete had a density of 2370 kg/m^3 and the unconfined uniaxial compressive cylinder strength varied between 32.4 and 35.2 MPa. Totally four experiments are compared in this thesis, and their results are summarized in Table 6.2.

Table 6.2 Data summary for the experiments with 0.906 kg steel projectile impacting a concrete cylinder.

Striking velocity [m/s]	Projectile mass [kg]	f_c [MPa]	Depth of penetration [m]
277	0.906	35.2	0.173
499	0.912	33.5	0.480
642	0.905	34.7	0.620
800	0.904	32.4	0.958

6.2 Analyses with Abaqus/Explicit

Analyses performed with Abaqus/Explicit are only compared to the experimental series by Hansson (1998). The FE model was 2-D axi-symmetric with quadratic elements; for the target of sizing 12.5 mm x 12.5 mm, see Leppänen (2001).

For analysis with large deformations in Abaqus/Explicit, an erosion algorithm must be used to avoid numerical problems. The erosion algorithm works by removing elements which have reached a user-specified criterion, in Abaqus/Explicit the plastic strain.

As previously described in section 5.4, Abaqus/Explicit has no material model that considers non-linearity for compression and tension at the same time for one element. With a combination of compression and tension models, it is possible to achieve results that agree with experiments regarding the depth of perforation and the crater size, see Figure 6.1 and, for further details, Leppänen (2001).

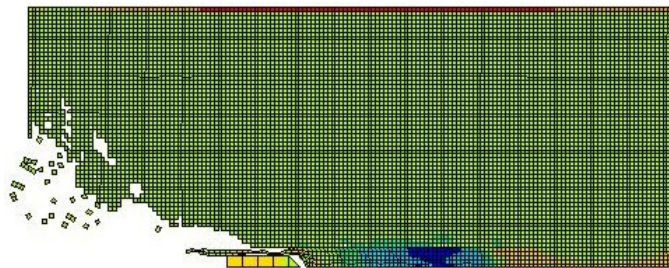


Figure 6.1 Analysis with Abaqus/Explicit. Projectile impact a concrete target.

6.3 Analyses with AUTODYN

The EOS used in the numerical model is a combined P-Alpha EOS and polynomial EOS; see Figure 5.5. The material parameters is shown in Appendix A. Detailing of the material parameters are described in AUTODYN (2001); here the compaction phase (polynomial EOS) is chosen to have the default values from the material library in AUTODYN. In the experimental series with 6.28 kg projectile, the density of the concrete is assumed to be 2400 kg/m³; see Betonghandboken (1994) (density of plain concrete).

The constitutive model used in the study is the RHT model shown in Figure 5.7, as described in section 5.4.3. Parameters A and N describe the failure surface (compressive meridian); see Appendix A for values. From the knowledge of the concrete behaviour in tri-axial stress states, the parameters can be decided. In this thesis, parameters used are calculated according to the model proposed by Attard and Setunge (1996), as shown in Figure 6.2 for low confining pressures. The proposed model by Attard and Setunge (1996) is limited to low confining pressures. However, the parameters A and N used in this thesis fit the experimental data presented by Bazant *et al.* (1996), with $f'_c = 46$ MPa; see Figure 4.5.

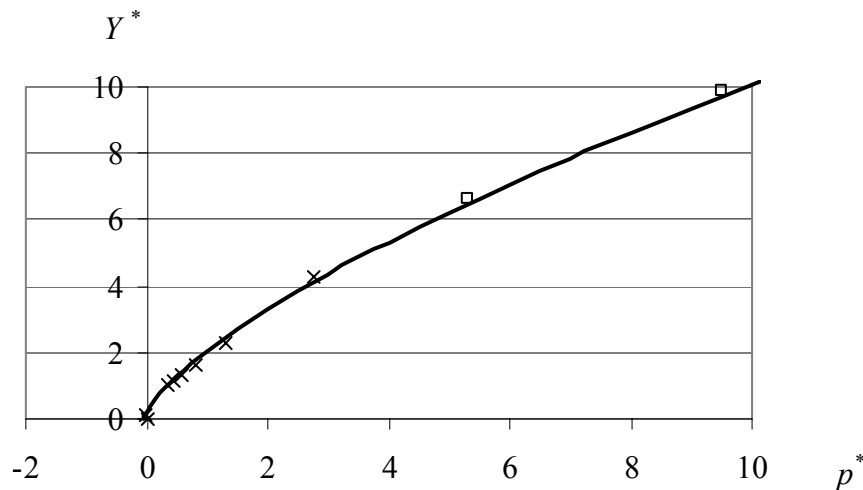


Figure 6.2 Failure surface (compressive meridian). $F_{RATE}(\dot{\epsilon}) = 1$, Y^* and p^* is normalized by f_c . Cross markers show input according to model by Attard and Setunge (1996), and rectangular markers show experimental data from Bazant *et al.* (1996).

The residual strength, as shown in Figure 6.3, is calculated on the basis of the model proposed by Attard and Setunge (1996), as previously discussed in section 5.6.

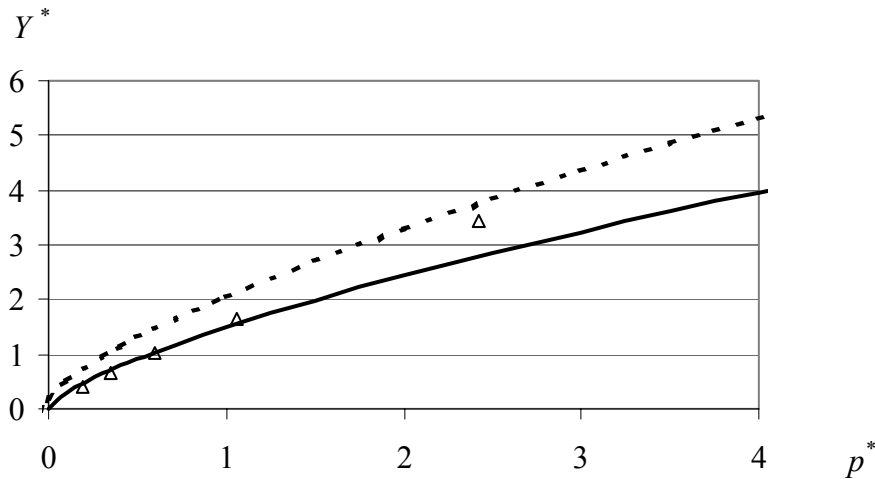


Figure 6.3 Residual strength. Triangular markers show input from model proposed by Attard and Setunge (1996). Dotted line is the failure Surface.

The material parameters for the constitutive model used in analyses are shown in Appendix A. In the experimental series by Hansson (1998), the tested concrete cube strength was 40 MPa. However, the cylinder strength is used as input in the material model, which is calculated from the cube strength according to the CEB-FIB Model Code 1990 (1993). In addition, the CEB Model Code 90 is used for calculating the material parameters, for instance the bulk modulus or tensile strength.

6.3.1 Mesh descriptions

6.3.1.1 Numerical mesh 1

The numerical mesh 1 is shown in Figure 6.4, where the results from analysis are compared to experiments from Hansson (1998). The target is of concrete cast in a steel culvert. The model is axisymmetric, created by quadratic elements with an element length of 6.25 mm, totaling 128 x 320 elements (for the target).

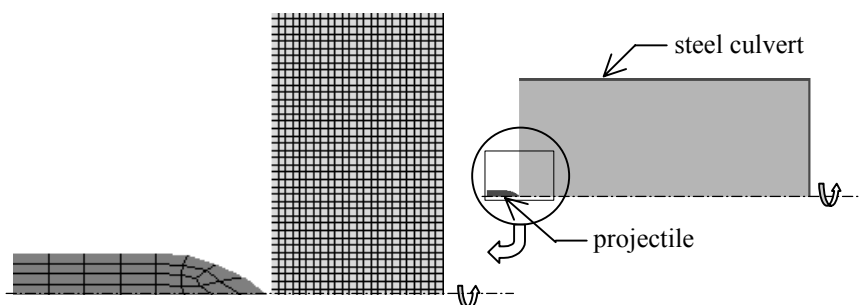


Figure 6.4 Numerical mesh 1.

6.3.1.2 Numerical mesh 2

The numerical mesh 2 is shown in Figure 6.5, where the results from analysis are compared to experiments from Forrestal *et al.* (1994). The target is of concrete cast in a galvanized steel culvert. The model is axisymmetric, created by rectangular elements with an element length of approximately 4 mm. For a target length of 0.76 m, the mesh size is 190 x 172 elements as seen in Figure 6.5, and for the target length of 1.83 m the mesh size is 153 x 458 elements.

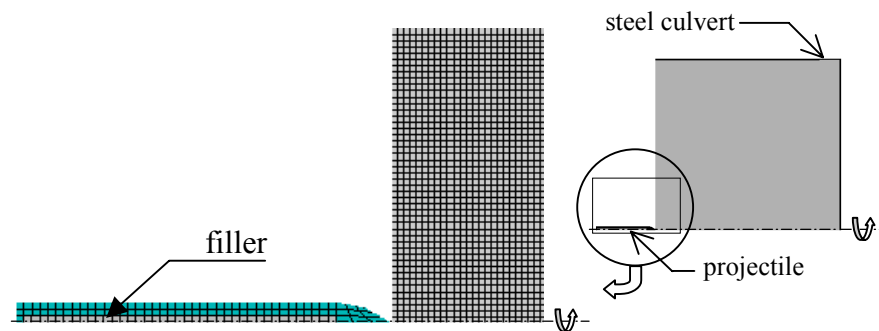


Figure 6.5 Numerical mesh 2.

6.3.2 Results

For the experimental results from Hansson (1998) the crater size and depth of penetration have been compared with both the Lagrangian and Eulerian method.

For the experimental results from Forrestal *et al.* (1994) the depth of penetration has been compared with the Lagrangian method, and, the crater sizes are shown for the numerical results.

6.3.2.1 Experiments with 6.28 kg projectile impacting a concrete cylinder

In the experiments two shots were made, first one with support and secondly one without any support at the backside. The depths of penetration were 655 mm and 660 mm respectively. The crater diameter was approximately 0.8 m for both shots.

For the numerical comparison without support at the backside, the depth of penetration by the was 636 mm with the Lagrangian technique (erosion criterion of 125 %), and 649 mm with the Eulerian technique, as shown in Figure 6.6.

With the Eulerian technique both the crater size and the depth of penetration agrees very well with the experimental results. Using the Lagrangian technique, the crater with erosion criterion of 125 % is too large. By increasing the criterion to 140 %, the crater size agrees with experiments, but the depth of penetration becomes 584 mm.

For numerical results with support at the backside, the depth of penetration was 627 mm with the Lagrangian technique and erosion criterion of 125 %. With erosion criteria of 140 % the depth of penetration was 575 mm.

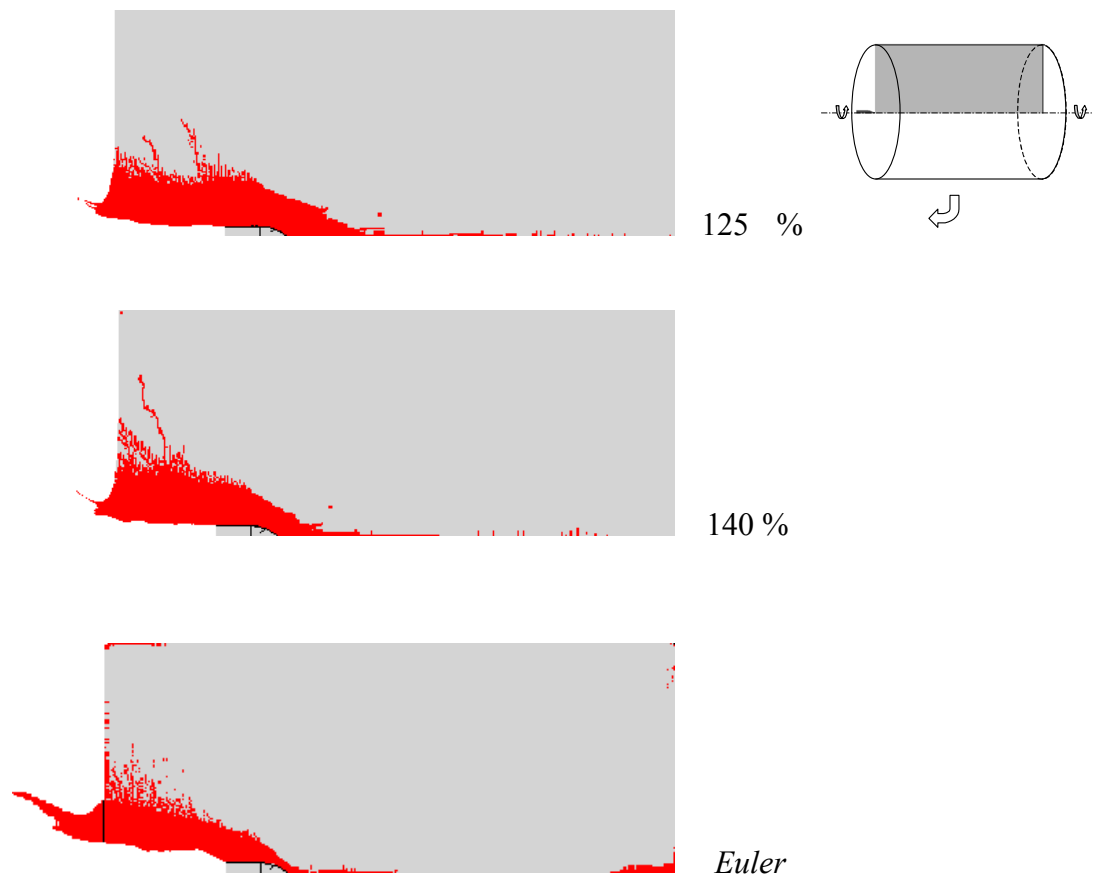
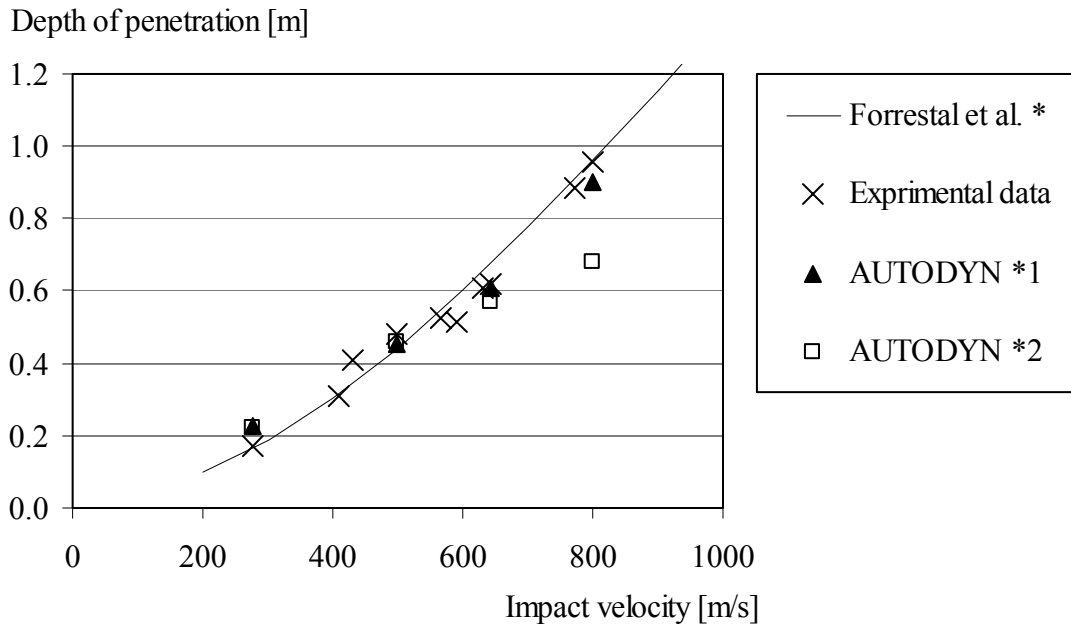


Figure 6.6 Cratering and the depth of penetration. Above: Lagrangian mesh; erosion criteria, $e = 125\%$ and $e = 140\%$. Below: Eulerian mesh. Comparison with experiments by Hansson (1998).

6.3.2.2 Experimental 0.906 kg projectile impacting a concrete cylinder

In the numerical model used for comparison with experimental results by Forrestal *et al.* (1994), the material parameters (strain rate dependency, residual strength, and criteria for erosion) for the concrete target are the same as in comparison with the experimental results with 6.28 kg projectile (except for the uniaxial compressive strength and density; see Appendix A). Totally four experimental results have been compared, all with a projectile diameter of 26.9 mm, and with varying impact velocities. The results from the analysis are shown in Figure 6.7, where the depth of penetration is analysed with the RHT model for different impact velocities.

The projectile was made of steel with hardness of R_c 43–45. The yield strength for this R_c 43–45 steel is 972 MPa and the ultimate strength is 1448 MPa. In the numerical model, a von Mises material model is used for the steel. Since the von Mises material model has no hardening in AUTODYN, the yield strengths of 972 MPa and 1448 MPa were used in the analyses; this gives a lower and an upper limit of the strength of steel.



* Empirical formula from Forrestal *et al.* (1994).

*1 Yield strength of steel is 1448 MPa.

*2 Yield strength of steel is 972 MPa.

Figure 6.7 Comparison of numerical results with experimental results from Forrestal *et al.* (1994).

The same model that was used previously for comparison with experimental results from the larger projectile having a mass of 6.28 kg – can predict the depth of penetration of the smaller projectile having a weight of approximately 0.906 kg. In Figure 6.8 the crater size and depth of penetration are shown from the analyses. The depth of penetration, maximum crater diameter and the lateral damage are increased for higher impact velocities. In these analyses the yield strength of the steel in the projectile was 1448 MPa. The crater size is smaller for the light projectile than in experiments with the heavier projectile (with mass of 6.28 kg and diameter of 75 mm).

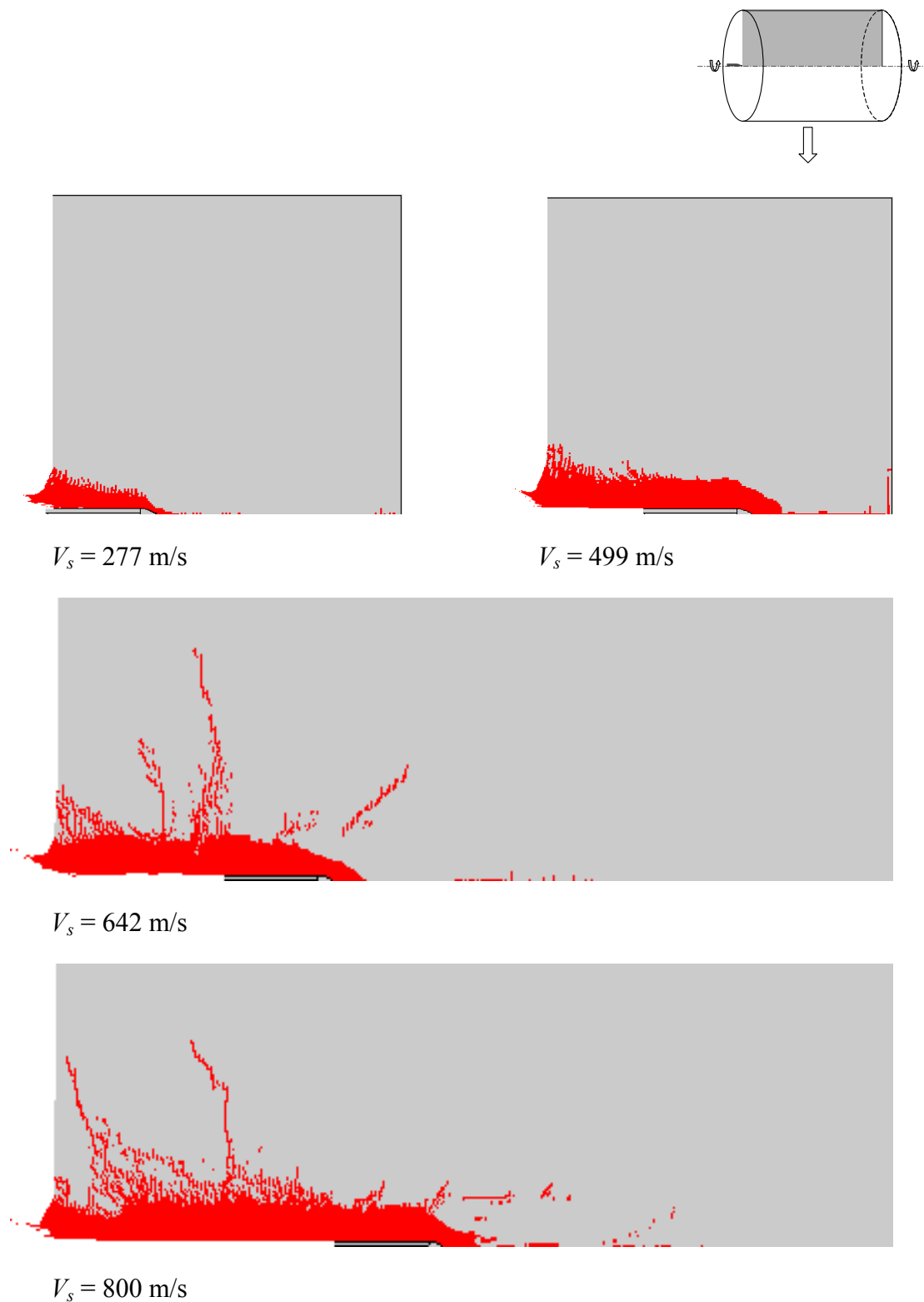


Figure 6.8 Cratering and the depth of penetration for varying impact velocities of the projectile. Lagrangian mesh; erosion criterion = 140 %. The yield strength for the steel of the projectile in the analyses was 1448 MPa. Comparison with experiments by Forrester et al. (1994).

In analyses where steel strength used for the projectile was 972 MPa, the results were very similar at low impact velocities, i.e. 277 m/s and 499 m/s. The crater size and depth of penetration were hardly affected by the lower steel strength. For the experiments with higher impact velocities, i.e. 642 m/s and 800 m/s the depth of penetration is less than when using the ultimate strength of steel in the analyses, see Figure 6.9.

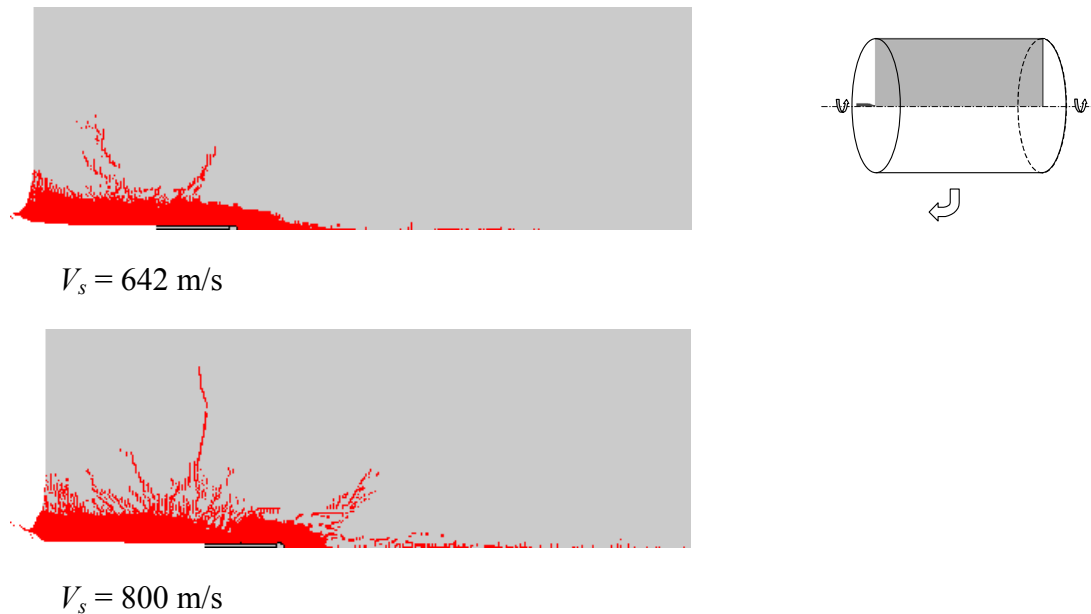


Figure 6.9 Cratering and the depth of penetration. Lagrangian mesh; erosion criterion = 140 %. The yield strength for the steel of the projectile in the analyses was 972 MPa. Comparison with experiments by Forrestal et al. (1994).

For the higher impact velocities, the steel strength of the projectile is important. The projectile deforms when using the true yield strength of the material in the material model (von Mises), as shown in Figure 6.10. However, when using the ultimate strength of the steel the projectile will not deform.

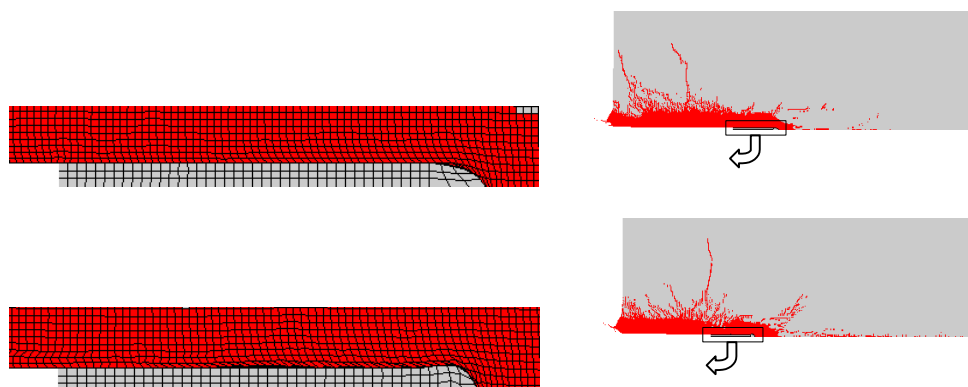


Figure 6.10 Projectile deformations for different yield strengths of steel. Impact velocity of 800 m/s. Above: The yield strength for steel of the projectile in the analysis was 1448 MPa. Below: The yield strength for steel in the projectile of the analysis was 972 MPa.

6.4 Discussion

Abaqus/Explicit has no material model that can combine non-linearity of compression and tension at the same time for one element. Normally, two different material models are combined: for areas where the compressive stresses are high, the compression model is used, and for areas where tensile stresses are high (where the compressive stresses are linear) the tension model is used. With a combination of a compression model and a tension model, it is possible to achieve results that agree with experiments regarding the depth of perforation and the crater size. However, Abaqus/Explicit cannot be used for general impact loading, since by using the method with combined models there can be errors in the analysis even if the end result seems to be correct. First of all, the stresses will vary from high compressive stresses to high tensile stresses; this leads to defaults in the analysis. Secondly, the distinction in where to use the compression and tension models is hard to draw, especially for analysis with multiple hits, such as fragments impacting a concrete wall.

AUTODYN, on the other hand, was created for analyses with large deformations. For reliable model, results from several experiments must be reproduced, regarding both the crater size and the depth of penetration. For example, correct results on depth of penetration can be obtained by changing, for instance, the residual strength or the erosion criterion (with the Lagrangian method).

In this thesis, numerical comparisons to experiments by Hansson (1998) were made with both Lagrangian and Eulerian methods. The erosion criterion, the instantaneous geometric strain for Lagrangian analyses, was calibrated to fit the experimental results. This erosion criterion was further used for comparison with another experimental series, in Forrestal *et al.* (1994), with varying impact velocities for the projectile.

For the experiments by Forrestal *et al.* (1994) the projectile was modelled with the von Mises material model. The model has no hardening, and the difference between the ultimate strength and the yield strength of the steel is so great that, by using the yield strength of the material, the depth of penetration will be underestimated. Therefore, analyses using the ultimate strength as the yield strength in the model were also carried out. This gives lower and upper limits according to the strength of the steel in the projectile. At low impact velocities the difference in depth of penetration is negligible, but for the higher impact velocities the increase of the steel strength is important as shown in Figure 6.7. In the experiments, non-deforming projectiles were used. As shown in Figure 6.10, in the analysis the projectile will deform when the increase in steel strength is not modelled. Hence, modelling the steel accurately, i.e. including hardening in the material model, is important at higher impact velocities.

6.5 Concluding remarks

Abaqus/Explicit is limited for impact analyses and is not suitable for general penetration analyses. With a knowledge of concrete under tri-axial stress states (failure surface, residual strength etc.), and with sophisticated material models such as the RHT model in AUTODYN, the depth of penetration and the crater size can be predicted.

In this thesis two experimental series has been compared, with varying projectile weights and impact velocities; in all cases the depth of penetration was predicted well. The Eulerian method is preferable. With the Lagrangian method, by using the erosion algorithm, elements are removed from the model and thus also mass and strain energy, and non-physical results are obtained. However, the Lagrangian method is time-saving.

For the concrete target, the material parameters that mostly influence the depth of penetration are the compressive strength, the strain rate dependency for compression, and the level of the residual strength. The fracture energy, tensile strength, and strain rate dependency for tension are the material parameters that mostly influence the crater size. The projectile impact velocity, mass, diameter and shape are of course also important factors for the depth of penetration and crater size.

7 Conclusions

7.1 General conclusions

The main aim of this thesis was to increase the knowledge of concrete structures subjected to explosive loading. A further intention has been to describe how to use the non-linear FE method for severe loading cases. FE analyses with a combination of blast and fragment impacts are very complex; in this thesis the analyses are limited to projectiles impacting a concrete target.

The theory of blast waves and their reflections describes the nature of the explosion. By using this, the load can be applied to a concrete structure in a realistic way. The classic stress wave theory describes the stress wave propagation in concrete at dynamic loading for elastic materials. Concrete under severe loading is far from elastic and the classic elastic assumptions are not valid; the shock wave theory is used to describe the material behaviour. The fundamental shock wave equations are based on the equations for conservation of mass, momentum and energy.

The concrete behaviour changes under dynamic loading. The initial stiffness, the ultimate strength, in both compression and tension will increase, and the concrete strain capacity is extended in dynamic loading. Furthermore, the fracture of a concrete member changes at dynamic loading and multiple fracture planes are obtained.

For design of protective structures, their penetration by fragments and projectiles is an important issue, and traditionally empirical equations are used to predict the depth of penetration. In the literature there are empirical equations to predict the depth of penetration for fragments and projectiles impacting a concrete target. The empirical equations give a good prediction of the depth of penetration, but will not describe the structural behaviour of the concrete structure. To increase the knowledge of concrete subjected to severe loading, a combination of experiments with the FE method is a powerful tool. It can be used for detailed analysis of the structural behaviour.

In this thesis, the FE programs Abaqus/Explicit and AUTODYN have been used for projectiles impacting a concrete target. Abaqus/Explicit has limitations; the program lacks material models that describe non-linearity for both compression and tension (for the same element). In Abaqus/Explicit, an erosion algorithm must be used to avoid numerical problems. By using the erosion algorithm, elements during the analyses are removed, thus mass and strain energy, and non-physical results are obtained.

AUTODYN was created originally for large deformation analyses. In AUTODYN there are several methods – Lagrangian, Eulerian and SPH – to describe the material movement. In this thesis the SPH technique has not been investigated. With the Lagrangian method, an erosion algorithm must be used to avoid numerical problems, and the level of erosion influences the depth of penetration. With the Eulerian method the numerical grid is fixed in space and the material moves in the grid, so that no erosion algorithm is needed. The Eulerian method is preferable since physical solutions are obtained, although, the computational time increases. For saving time, the Lagrangian method is preferable, and it is recommended for first estimations in new problems.

A reliable model must be able to describe experimental results. The RHT model in AUTODYN seems to be able to predict both the depth of penetration and the crater size for projectile impact analyses in concrete.

The material parameters that mostly influence the depth of penetration are the concrete compressive strength, the strain rate dependency for compression, and the level of the residual strength. Furthermore, the numerical mesh influences the depth of penetration. The mesh dependency is commonly treated by refining the mesh until the differences are negligible. However, the results obtained in this thesis are reasonable. The material parameters that mostly influence the size of the crater are the tensile strength, the fracture energy and the strain rate dependency for tension.

7.2 Future research

The work presented in this thesis is a part of a research project whose long-term aim is to increase the knowledge of reinforced concrete structures subjected to loading with a combination of blast and fragments from an explosion. To reach the aim, combining experiments with non-linear FE analyses is a powerful tool, and is a natural continuation of this thesis.

From the explosion, besides the blast wave and fragmentation, much energy is released in the form of increasing temperature in the materials. In this thesis the temperature effects are neglected, and further study is needed where they are taken into account.

A large research area has been the behaviour of concrete under dynamic loading. The experiments carried out so far in the literature are mainly for uniaxial loading. Experiments on dynamic loading for confined concrete are limited to low strain rates. There is need of experimental results on confined concrete under loading at high strain rates, for both compression and tension, to increase the knowledge of concrete behaviour and the input for material models.

From standard tri-axial static tests, the residual strength can be estimated, and has been used for non-linear FE analyses in this thesis. However, it is not obvious that the residual strength is equal for dynamic loading compared to static loading. Experimental results under dynamic loading would thus be very interesting.

For FE analyses the strain rate in the material is mesh-dependent. The traditional way to treat the mesh dependency is to refine the mesh. There are various methods of overcoming the mesh dependency, such as using non-local material models, and these should also be developed further.

8 References

- Abaqus/Explicit Manuals (1998). *Abaqus/Explicit Manuals, Version 5.8*, Hibbitt, Karlsson & Sorensen, Inc. 1998, USA.
- Attard M. M. and Setunge S. (1996): Stress-strain relationship of confined and unconfined concrete. *Aci Materials Journal*, Vol. 93, No. 5, Sep-Oct 1996, pp. 432-442.
- AUTODYN Manuals (2001): *AUTODYN Manuals, Version 4.2*, Century Dynamics, Inc. 2001, Sam Ramon, USA.
- Baker W. E. (1973): *Explosions in air*, Univ. of Texas Press, Austin, 268 pp.
- Bazant Z. P., Bishop F. C. and Chang T. P. (1986): Confined Compression Tests of Cement Paste and Concrete up to 300-ksi. *Journal of the American Concrete Institute*, Vol. 83, No. 4, Jul-Aug 1986, pp. 553-560.
- Bazant Z. P., Xiang Y. Y., Adley M. D., Prat P. C. and Akers S. A. (1996): Microplane model for concrete .2. Data delocalization and verification. *Journal of Engineering Mechanics-Asce*, Vol. 122, No. 3, Mar 1996, pp. 255-262.
- Bergman S. G. A. (1950): Inträngning av pansarbrytande projektiler och bomber i armerad betong (in Swedish). *FortF/F TM B 2*, 1950, pp. 179-217.
- Betonghandbok (1994): *Betonghandbok, Material, utgåva 2* (Handbook for Concrete Material, second edition, in Swedish), AB Svensk Byggtjänst och Cements AB, Solna, 1127 pp.
- Bischoff P. H. and Perry S. H. (1991): Compressive behaviour of concrete at high strain rates. *Materials and Structures*, Vol. 24, 1991, pp. 425-450.
- Bulson P. S. (1997): *Explosive loading of engineering structures*, E & FN Spon, London, 233 pp.
- CEB-FIB Model Code 1990 (1993): *CEB-FIB Model Code 1990, Design Code*, Thomas Telford, Lausanne, Switzerland, 437 pp.
- Clegg R. A., Sheridan J., Hayhurst C. J. and Francis N. J. (1997): The application of SPH techniques in AUTODYN-2D to kinetic energy penetrator impacts on multi-layered soil and concrete targets. *8th International Symposium on Interaction of the Effects of Munitions with Structures*, Virginia, USA, pp. 9.
- ConWep (1992): *Collection of conventional weapons effects calculations based on TM 5-855-1, Fundamentals of Protective Design for Conventional Weapons*, U. S. Army Engineer Waterways Experiment Station, Vicksburg, USA.
- Forrestal M. J., Altman B. S., Cargile J. D. and Hanchak S. J. (1994): An Empirical Equation for Penetration Depth of Ogive-Nose Projectiles into Concrete Targets. *International Journal of Impact Engineering*, Vol. 15, No. 4, Aug 1994, pp. 395-405.
- Forsén R. (1989): *Initialverkan, verkan på byggnader av inneslutna explosioner (in Swedish)*. C 20747-2.6, FOA Rapport, Stockholm, 37 pp.
- Forsén R. and Edin K. (1991): *Vapenverkan mot flervånings betongbyggnad III. Bestämning av skador från splitterladdningar mot husfasad i skala 1:4 (in Swedish)*. C 20860-2.3, FOA report, Sundbyberg, 40 pp.

- Forsén R. and Nordström M. (1992): *Damage to Reinforced Concrete Slabs Due to the Combination of Blast and Fragment Loading (In Swedish)*. B 20101-2.6, National Defence Research Establishment (FOA), Tumba, 12 pp.
- FortH1 (1987): *Fortifikationshandbok del 1, Kapitel 1-3 (In Swedish)*, Stockholm, 50 pp.
- Geradin M. and Rixen D. (1994): *Mechanical Vibrations, Theory and Application to Structural Dynamics*, Wiley, Paris, 411 pp.
- Gylltoft K. (1983): *Fracture mechanics models for fatigue in concrete structures*. Doctoral Thesis, Division of Structural Engineering, Luleå University of Technology, Luleå, Sweden, 210 pp.
- Hansson H. (1998): *Numerical simulation of concrete penetration*. 98-00816-311--SE, FOA-R, Defence Research Establishment, Tumba, 17 pp.
- Hughes G. (1984): Hard missile impact on reinforced concrete. *Nuclear Engineering and Design*, Vol. 77, 1984, pp. 23-35.
- Imran I. and Pantazopoulou S. J. (2001): Plasticity model for concrete under triaxial compression. *Journal of Engineering Mechanics-ASCE*, Vol. 127, No. 3, March 2001, pp. 281-290.
- Janzon B. (1978): *Grundläggande Stridsdelfysik (in Swedish)*. C 20261-D4, FOA Rapport, Stockholm, 164 pp.
- Johansson J. P. M. and Karlsson S. (1997): *Nytt armeringsutförande i betongramhörn utsatta för positivt moment (in Swedish)*. Master Thesis 97:5, Division of Concrete Structures, Chalmers University of Technology, Göteborg, Sweden, 145 pp.
- Johansson M. (1996): *New Reinforcement Detailing in Concrete Frame Corners of Civil Defence Shelters*. Licentiate Thesis, Publication 96:1, Department of Structural Engineering, Division of Concrete Structures, Chalmers University of Technology, Göteborg, 78 pp.
- Johansson M. (1999): *Non-linear Finite Element Analyses of Civil Defence Shelter Subjected to Explosion Load or Collapse Load*. Report 99:8, Department of Structural Engineering, Division of Concrete Structures, Chalmers University of Technology, Göteborg, 85 pp.
- Johansson M. (2000): *Structural Behaviour in Concrete Frame Corners of Civil Defence Shelters, Non-linear Finite Element Analyses and Experiments*. Doctoral Thesis, Department of Structural Engineering, Chalmers University of Technology, Göteborg, Sweden, 204 pp.
- Johansson M. (2002): *Stötvågsutbredning i luft (in Swedish)*. Publication B54-223/02, Swedish Rescue Service Agency, Karlstad, Sweden.
- Johnson G. R., Beissel S. R., Holmquist T. J. and Frew D. J. (1998): Computed radial stresses in a concrete target penetrated by a steel projectile. *Fifth International Conference on Structures Under Shock and Impact V*, pp. 793-806.
- Jonasson T. (1990): *Kontaktverkan I, Sprängladdningars kontaktverkan på armerade betongplattor*. C 20809-2.6, FOA rapport, Sundbyberg, 58 pp.
- Krauthammer T. (2000): *Modern Protective Structures, Design, Analysis and Evaluation*. Course notes, The Pennsylvania State University, 358 pp.

- Leppänen J. (2001): *Finita Elementanalyser av splitterbelastade betongkonstruktioner, Inledande studie med ABAQUS/Explicit (in Swedish)*. Rapport 01:1, Institutionen för konstruktionsteknik, Betongbyggnad. Chalmers Tekniska Högskola, Göteborg, 72 pp.
- Needleman A. (1988): Material Rate Dependence and Mesh Sensitivity in Localization Problems. *Computer Methods in Applied Mechanics and Engineering*, Vol. 67, No. 1, Mar 1988, pp. 69-85.
- Nordström M. (1992): *Splitterbelastning av betongplattor I, Metodik för bestämning av energiupptagande förmåga hos armerade betongplattor belastade med olika splitertätheter (in Swedish)*. D 20209-2.3, FOA rapport, Sundbyberg, 54 pp.
- Nordström M. (1993): *Splitterbelastning av betongplattor II, Energiupptagande förmåga hos armerade betongplattor belastade med olika splitertätheter. (in Swedish)*. D 20226-2.3, FOA rapport, Sundbyberg, 30 pp.
- Nordström M. (1995): *Splitterbelastning av betongplattor III, Energiupptagande förmåga hos armerade betongplattor belastade med olika kombinationer av splitthastigheter, splitertätheter och splitstorlekar. (in Swedish)*. 95-00094-7(6,2.6)--SE, FOA-R, Stockholm, 101 pp.
- Plos M. (1994): *Ny armeringsskarv för ramhörn i skyddsrum (in Swedish)*. Report 94:2, Division of Concrete Structures, Chalmers University of Technology, Göteborg, Sweden, 27 pp.
- Riedel W. (2000): *Beton unter dynamischen Lasten Meso- und makromechanische Modelle und ihre Parameter (in German)*. Doctoral Thesis, Institut Kurzzeitdynamik, Ernst-Mach-Institut, der Bundeswehr Munchen, Freiburg, 210 pp.
- Ross C. A., Jerome D. M., Tedesco J. W. and Hughes M. L. (1996): Moisture and strain rate effects on concrete strength. *Aci Materials Journal*, Vol. 93, No. 3, May-Jun 1996, pp. 293-300.
- Rossi P. and Toutlemonde F. (1996): Effect of loading rate on the tensile behaviour of concrete: Description of the physical mechanisms. *Materials and Structures/Materiaux et Constructions*, Vol. 29, No. 186, Mars 1996, pp. 116-118.
- Swedish Rescue Services Agency (1994): *Shelter Regulations, SR - English edition*, Publication B54-168/94, Karlstad, Sweden, 94 pp.
- Swedish Rescue Services Agency (1998): *Skyddsrumregler SR - Produktion och vidmakthållande*, (Shelter Regulations - Production and Maintenance. in Swedish), Publication B54-141/98, Karlstad, Sweden.
- Takeda J., Tachikawa H. and Fujimoto K. (1974): Mechanical behavior of concrete under higher rate loading than in static test. *Proc. Mechanical Behaviour of Materials*, pp. 479-486.
- US Army Fundamentals of Protective Design (Non-nuclear) (1965): *US Army Fundamentals of Protective Design (Non-nuclear)*, Department of Army Technical Manual TM5-855-1, Washington.
- Weerheijm J. (1992): *Concrete under impact tensile loading and lateral compression*. Doctoral Thesis, Delft University of Technology, The Netherlands, 157 pp.

- Wiberg N. E. (1974): *Finita Elementmetoden, en datoranpassad beräkningsmetod för ingenjörproblem (in Swedish)*, LiberTryck, Göteborg, Sweden, 1974, 427 pp.
- Zielinski A. J. (1982): *Fracture of concrete and mortar under uniaxial impact tensile loading*. Doctoral Thesis, Delft University of Technology.
- Zielinski A. J. (1985): *Concrete under biaxial loading: Static compression-impact tension*. Stevin Report 5-85-1, Delft University of Technology.
- Zukas J. A. and Scheffler D. R. (2000): Practical aspects of numerical simulations of dynamic events: effects of meshing. *International Journal of Impact Engineering*, Vol. 24, No. 9, Oct 2000, pp. 925-945.

Appendix A: Input data to RHT model in AUTODYN

Input data for concrete: RHT model, equation of state (EOS).

Parameter	Experiments with 6.28 kg projectile	Experiments with 0.906 kg projectile
Porous density (g/cm ³)	2400	2370
Porous soundspeed (m/s)	2920	2920
Initial compaction pressure	2.33e4	2.33e4
Solid compaction pressure	6e6	6e6
Compaction exponent n	3	3
Solid EOS:	Polynomial	Polynomial
Compaction curve:	Standard	Standard
<i>A1</i> (kPa)	3.527e7	3.527e7
<i>A2</i> (kPa)	3.958e7	3.958e7
<i>A3</i> (kPa)	9.04e6	9.04e6
<i>B0</i>	1.22	1.22
<i>B1</i>	1.22	1.22
<i>T1</i> (kPa)	3.527e7	3.527e7
<i>T2</i> (kPa)	0	0

Input data for concrete: RHT model, constitutive model.

Parameter	Experiments with 6.28 kg projectile	Experiments with 0.906 kg projectile
Shear Modulus (kPa)	1.433e7	1.433e7
Compressive Strength f'_c (kPa)	3.38e4	f'_c
Tensile Strength f_t/f'_c	0.078	0.078
Shear Strength f_s/f'_c	0.18	0.18
Failure Surface Parameter A	2	2
Failure Surface Parameter N	0.7	0.7
Tens./Compr. Meridian Ration	0.6805	0.6805
Brittle to Ductile Transit.	1.05e-2	1.05e-2
G(elas.)/G(elas-plas.)	2	2
Elastic Strength/ f_t	0.7	0.7
Elastic Strength/ f'_c	0.53	0.53
Use Cap on Elastic Surface	Yes	Yes
Residual Strength Const. B	1.5	1.5
Residual Strength Exp. M	0.7	0.7
Comp. Strain Rate Exp. a	0.032	0.032
Tens. Strain Rate Exp. D	0.025	0.025
Max. Fracture Strength Ratio	1e20	1e20
Damage constant D1	0.04	0.04
Min. Strain to Failure	0.01	0.01
Residual Shear Modulus Frac.	0.13	0.13
Tensile Failure model	Hydro Tens.	Hydro Tens.
Erosion Strain/instantaneous geometric strain (Lagrange)	1.25 and 1.4	1.4

Appendix B: Parameter study

The parameter study has been carried out with experiments using a 6.28 kg projectile, where the material parameters are shown in Appendix A.

Influence of	Residual Strength	Erosion criteria	Mesh	Strain rate factor δ	Depth of penetration [mm]	Maximum crater size [mm]
Residual Strength, B	0.9	1.25	mesh a	0.025	811	600
	1.1	1.25	mesh a	0.025	662	640
	1.5	1.25	mesh a	0.025	601	665
Erosion criteria	1.5	0.6	mesh a	0.025	732	755
	1.5	1.2	mesh a	0.025	529	780
	1.5	1.8	mesh a	0.025	411	575
Mesh dependency	1.5	1.25	mesh a	0.025	629	615
	1.5	1.25	mesh b	0.025	636	605
	1.5	1.25	mesh c	0.025	675	610
	1.5	1.25	mesh d	0.025	721	635
Strain rate factor δ	1.5	1.25	mesh a	0	651	760
	1.5	1.25	mesh a	0.03	572	615
	1.5	1.25	mesh a	0.07	481	585
	1.5	1.25	mesh a	0.11	417	340

Appendix C: Empirical formulas for penetration with projectiles

Bergman (1950)

$$\frac{x}{d} = 4.86 * \chi * V_s \left(1.44 + \frac{0.18}{\chi * V_s^{1.73}} + 0.005 * \chi * V_s^{1.73} \right) \quad \text{for } \geq 3.5 \quad (\text{C.1})$$

If $\frac{x}{d} < 3.5$ then

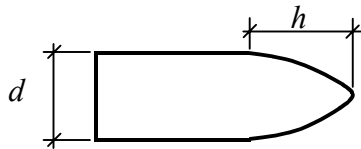
$$\frac{x}{d} = \frac{V_s}{V_{3.5}} * 3.5 \quad (\text{C.2})$$

where $V_{3.5}$ is the velocity that corresponds to $\frac{x}{d} = 3.5$.

In these formulas,

$$\chi = \frac{N * m_p}{\sqrt{\sigma_c} * d^{2.8}} * 7.57 * 10^{-8} \quad (\text{C.3})$$

and x = depth of penetration [m], m_p = projectile mass [kg], σ_c = concrete compressive cube strength [MPa], V_s = impact velocity [m/s], d = projectile diameter, and N is given from Figure C.1.



$$N = 0.70 + 0.27 \frac{h}{d}$$

Figure C.1 Nose shape factors.

The experimental ranges in which the equation is valid for ogival projectiles with nose shapes between calibre diameters of d : 0.1 to 0.4 [m], N : 0.8 to 1.2, m_p : 0.02 to 1,000 [kg], σ_c : 30 to 50 [MPa], D : 0.1 to 0.4 [m] and $V_s < 1,200$ [m/s].

Whiffen (1983)

British Road Research Laboratory produced an empirical formula, Whiffen (1983), according to Bulson (1997):

$$x = \left(\frac{870}{\sigma_c^{0.5}} \right) \left(\frac{m_p}{d^2} \right) \left(\frac{d}{c} \right)^{0.1} \left(\frac{V_s}{1750} \right)^n \quad (\text{C.4})$$

where x = depth of penetration [in], m_p = projectile mass [lb],
 d = projectile diameter [in], σ_c = crushing strength of concrete [lb/in²],
 V_s = striking velocity [ft/sec], c = maximum aggregate size [in],

and

$$n = \frac{10.7}{\sigma_c^{0.25}} \quad (\text{C.5})$$

The experimental ranges on which the equation was based were for ogival projectiles with nose shapes between 0.8 and 3.5 calibre radius and σ_c : 800 to 10,000 (lb/in²), m_p : 0.3 to 22,000 (lb), d : 0.5 to 38 (in), d/c : 0.5 to 50, V_s : 0 to 3700 (ft/sec). (The formula fitted experimental data within a scatter, slightly less than $\pm 15\%$ wide.)

US Army Technical Manual on the Fundamentals of Protective Design (1965), based on the work by Beth (1943)

The units are the same as those in the British formula, see equation (C.4), and the accuracy was said to be within $\pm 15\%$.

$$x = \frac{222}{\sigma_c^{0.5}} \left(\frac{4m_p}{\pi d^2} \right) d^{0.215} \left(\frac{V_s}{1000} \right)^{1.5}, [\text{in}] \quad (\text{C.6})$$

Hughes (1983)

$$\frac{x}{d} = 0.19 * \kappa * \frac{I}{S} \quad (\text{C.7})$$

Where

κ = nose shape coefficient (= 1, 1.12, 1.26 and 1.39 for flat, blunt, spherical and very sharp noses respectively), I = impact parameter (= $m_p V_s^2 / (\sigma_t d^3)$), S = strain rate factor (= $1 + 12.3 \ln(1 + 0.03xI)$), m_p = missile mass [kg], V_s = impact velocity [m/s],
 σ_t = concrete tensile strength (modulus of rupture test) [Pa], d = missile diameter [m],

$$\sigma_t = 0.63(\sigma_c)^{1/2}. \quad (\text{C.8})$$

Forrestal et al. (1994)

$$x = \frac{m_p}{2\pi a^2 \rho N} \ln\left(1 + \frac{N\rho V_1^2}{S\sigma_c}\right) + 4a \quad \text{for } x > 4a \quad (\text{C.9})$$

$$S = \frac{N\rho V_s^2}{\sigma_c} * \frac{l}{\left(1 + \frac{4\pi a^3 N\rho}{m_p}\right) \exp\left(\frac{2\pi a^2 (x-4a)N\rho}{m_p}\right) - 1} \quad (\text{C.10})$$

$$N = \frac{8\psi - 1}{24\psi^2} \quad (\text{C.11})$$

$$V_1^2 = \frac{m_p V_s^2 - 4\pi a^3 S\sigma_c}{m_p + 4\pi a^3 N\rho} \quad (\text{C.12})$$

where

m_p = projectile mass [kg], a = shank radius [m], s = ogive radius [m], $\psi = s/2a$, σ_c = concrete compressive strength, ρ = target density [kg/m³], V_s = striking velocity [m/s], and the proportionality S is estimated as

$$S = 82.6(f'_c)^{-0.544} \quad (\text{C.13})$$

Limitations

The empirical formulas are validated for a diverse range of experimental data. The limitations of the formulas are shown in Table C.1.

Table C.1. Limitations of the empirical formulas.

Formula by	Impact velocity [m/s]	Projectile weight [kg]	Projectile diameter [m]	Concrete strength, f'_c [MPa]	I^*
Bergman	<1200	0.02-1000	0.1-0.4	25.5-42.5	-
Beth	-	-	-	-	-
Forrestal	<1200	0.064-5.9	<0.0762	13.5-96.7	-
Hughes	-	-	-	-	40-3500
Whiffen	<1128	0.1368-10000	0.0127-0.9652	5-58.6	-

* $I = m_p v^2 / (\sigma_c d^3)$, $I < 40$ corresponds to $h/d < 3.5$ and $x/d < 0.7$, and $I < 3500$ corresponds to the range of test data.

Appendix D: Empirical formulas for penetration with fragments

The depth of penetration

The depth of penetration is estimated by equations (D.1) and (D.2), according to Krauthammer (2000).

$$x = \frac{0.95m_f^{0.37}V_s^{0.9}}{f_c^{0.25}} \quad \text{for } x \leq 1.4m_f^{1/3} \quad (\text{D.1})$$

or

$$x = \frac{0.32m_f^{0.4}V_s^{1.8}}{f_c^{0.25}} + 0.4m_f^{1/3} \quad \text{for } x > 1.4m_f^{1/3} \quad (\text{D.2})$$

where m_f = fragment weight [oz], V_s = the fragment striking velocity [kfps] and f_c = the concrete compressive strength [psi].

The thickness of concrete wall that just prevent perforation

For steel fragments, the thickness of concrete wall that just prevents perforation is calculated as in Krauthammer (2000):

$$t_{pf} = 1.09xm_f^{0.033} + 0.91m_f^{0.33} \quad \text{inches} \quad (\text{D.3})$$

where x is the penetration depth from equations (D.1) and (D.2), and m_f is the fragment weight.

Licentiate Theses and Doctoral Theses, Department of Structural Engineering – Concrete Structures, Chalmers University of Technology, 1990-

- 90:1 Stig Öberg: Post Tensioned Shear Reinforcement in Rectangular RC Beams. Publication 90:1. Göteborg, April 1990. 603 pp. (No. 1021). Doctoral Thesis.
- 90:2 Johan Hedin: *Långtidsegenskaper hos samverkanskonstruktioner av stål och betong (Long Time Behaviour of Composite Steel Concrete Structures)*. Publication 90:2. Göteborg, August 1990. 53 pp. (No. 1079). Licentiate Thesis.
- 92:1 Björn Engström: *Ductility of Tie Connections in Precast Structures*. Publication 92:1. Göteborg, October 1992. 368 pp. (Nos. 936, 999, 1023, 1052). Doctoral Thesis.
- 93:1 Mario Plos: *Shear Behaviour in Concrete Bridges - Full Scale Shear Test. Fracture Mechanics Analyses and Evaluation of Code Model*. Publication 93:1. Göteborg, April 1993. 70 pp. (Nos. 1088, 1084). Licentiate Thesis.
- 93:2 Marianne Grauers: *Composite Columns of Hollow Steel Sections Filled with High Strength Concrete*. Publication 93:2. Göteborg, June 1993. 140 pp. (No. 1077). Doctoral Thesis.
- 93:4 Li An: *Load Bearing Capacity and Behaviour of Composite Slabs with Profiled Steel Sheet*. Publication 93:4. Göteborg, September 1993. 134 pp. (No. 1075). Doctoral Thesis.
- 93:5 Magnus Åkesson: *Fracture Mechanics Analysis of the Transmission in Zone in Prestressed Hollow Core Slabs*. Publication 93:5. Göteborg, November, 1993. 64 pp. (No 1112). Licentiate Thesis.
- 95:1 Christina Claeson: *Behavior of Reinforced High Strength Concrete Columns*. Publication 95:1. Göteborg, June 1995. 54 pp. (No. 1105). Licentiate Thesis.
- 95:2 Karin Lundgren: *Slender Precast Systems with Load-Bearing Facades*. Publication 95:2. Göteborg, November 1995. 60 pp. (No. 1098). Licentiate Thesis.
- 95:3 Mario Plos: *Application of Fracture Mechanics to Concrete Bridges. Finite Element Analysis and Experiments*. Publication 95:3. Göteborg, November 1995. 127 pp. (Nos. 1067, 1084, 1088, 1106). Doctoral Thesis.
- 96:1 Morgan Johansson: *New Reinforcement Detailing in Concrete Frame Corners of Civil Shelters. Non-linear Finite Element Analyses and Experiments*. Publication 96:1. Göteborg, November 1996. 77 pp. (No. 1106). Licentiate Thesis.
- 96:2 Magnus Åkesson: *Implementation and Application of Fracture Mechanics Models for Concrete Structures*. Publication 96:2. Göteborg, November 1996. 159 pp. (No. 1112). Doctoral Thesis.

- 97:1 Jonas Magnusson: *Bond and Anchorage of Deformed Bars in High-Strength Concrete*. Publication 97:1. Göteborg, November 1997. 234 pp. (No. 1113). Licentiate Thesis.
- 98:1 Christina Claeson: *Structural Behavior of Reinforced High-Strength Concrete Columns*. Publication 98:1. Göteborg 1998. 92 pp + I-IV, 75 pp. (No. 1105). Doctoral Thesis.
- 99:1 Karin Lundgren: *Three-Dimensional Modelling of Bond in Reinforced Concrete. Theoretical Model, Experiments and Applications*. Publication 99:1. Göteborg, November 1999. 129 pp. (No. 37). Doctoral Thesis.
- 00:1 Jonas Magnusson: *Bond and Anchorage of Ribbed Bars in High-Strength Concrete*. Publication 00:1. Göteborg, February 2000. 300 pp. (No. 1113). Doctoral Thesis.
- 00:2 Morgan Johansson: *Structural Behaviour in Concrete Frame Corners of Civil Defence Shelters*. Publication 00:2. Göteborg, March 2000. 220 pp. (No. 1106). Doctoral Thesis.
- 00:3 Rikard Gustavsson: *Static and Dynamic Finite Element Analyses of Concrete Sleepers*. Publication 00:3. Göteborg, March 2000. 58 pp. (No. 41). Licentiate Thesis.
- 00:4 Mathias Johansson: *Structural Behaviour of Circular Steel-Concrete Columns. Non-linear Finite Element Analyses and Experiments*. Publication 00:4. Göteborg, March 2000. 64 pp. (No. 48). Licentiate Thesis.
- 01:3 Gunnar Holmberg: *Fatigue of Concrete Piles of High Strength Concrete Exposed to Impact Load*. Publication 01:3. Göteborg, August 2001. 69 pp. (No. 55). Licentiate Thesis.
- 02:1 Peter Harryson: *Industrial Bridge Construction – merging developments of process, productivity and products with technical solutions*. Publication 02:1. Göteborg, January 2002. 90 pp. (No. 34). Licentiate Thesis.
- 02:2 Ingemar Löfgren: *In-situ concrete building systems – developments for industrial constructions*. Publication 02:2. Göteborg, March 2002. 125 pp. (No. 35). Licentiate Thesis.